Effect of In Phase and Out of Phase Forcing on Circular Cylinder Wake

by

Michael H. Moore Jr.

A thesis submitted to the Graduate Faculty of
Auburn University
in partial fulfillment of the
requirements for the Degree of
Master of Science

Auburn, Alabama
May 4, 2013

Keywords: Circular cylinder, Flow control, Periodic forcing

Approved by

Anwar Ahmed, Chair, Professor of Aerospace Engineering
Roy Hartfield, Walt and Virginia Woltosz Professor of Aerospace Engineering
Jay Khodadadi, Alumni Professor of Mechanical Engineering

Abstract

Using periodic forcing, the control of instabilities in the wake of a circular cylinder was investigated. The cylinder model had two straight slits, one on each side, that were connected to separate low frequency and high frequency acoustic drivers. In order to provide equal periodic forcing, the top and bottom slits were separated by a partition located in the middle of the cylinder. This feature also allowed the implementation of in-phase (IP) and out-of-phase (OP) forcing. The experiments were conducted at six different forcing frequencies and Reynolds numbers of 12,000 and 24,000. Excitation frequencies (f_e) ranging from $\frac{1}{2}f_{s_0}$ to $4f_{s_0}$ were utilized in an attempt to decrease and eliminate the amplitude of von Kármán vortex shedding. A unique random noise frequency excitation was also investigated and was found to similarly suppress the oscillatory wake. Forcing from the two dimensional slit was able to disrupt the formation of the von Kármán instability, therefore reducing the oscillatory wake and the pressure drag. A maximum reduction of 28% was observed for the in-phase driver mode and 26% for out-of-phase. At the lower Reynolds number the wake was more responsive to the periodic forcing and required a lower blowing coefficient. It was found that the out-of-phase excitation caused the shedding frequency to lock on to the corresponding excitation frequency until approximately $4f_{s_0}$. In-phase forcing was more efficient at suppressing the cylinder wake, while the out-of-phase driver mode had more control authority.

Acknowledgments

The author would like to thank Dr. Anwar Ahmed for his guidance, patience, and expertise in the development of this thesis. You have taught me many valuable lessons, and for that I am forever thankful. Thanks are also due to Mr. Andy Weldon for his advice and expertise in machining each part of the experimental apparatus. I would also like to thank Mr. AJ Weiner and Brian Davis for their support and encouragement while working in the wind tunnel. Last, but not least I would like to acknowledge my family and loving wife for their patience, encouragement, and emotional support through this long and challenging process.

Table of Contents

List of Figures

List of Tables

List of Abbreviations

ω	Vorticity, $\zeta = \frac{\omega d}{U_\infty}$
b	Wake half-width
C_d	Drag coefficient
C_μ	Blowing coefficient $\frac{u_j}{U_\infty}$
f_e	Excitation or forcing frequency
f_{s_0}	Natural shedding frequency
IP	In-phase forcing
k	Turbulent kinetic energy, $\frac{u'^2+v'^2+w'^2}{U_\infty^2}$
L	Formation length
OP	Out-of-phase forcing
P_s	static pressure
P_t	Total pressure
q	Dynamic pressure
R_{ij}	Reynolds shear stress, $\frac{\overline{u'v'}}{U_\infty^2}$
u_i'	Fluctuation component of velocity in the streamwise direction
u_j'	Fluctuation component of velocity in the normal direction
U_∞	Free stream velocity

v_s periodic excitation velocity

D Cylinder diameter

St Strouhal Number $\frac{fD}{U_\infty}$

Chapter 1

Introduction

Circular cylinders are classified as canonical bluff bodies due to the substantial amount of separation that occurs over the surface and are seen today in many practical applications. These geometric shapes are used readily due to their simple structural characteristics and ease of manufacturing. However, very unique and complex flow characteristics are produced in the wake of the body, that can cause premature fatigue or even structural failure due to vortex induced vibrations. Research on this topic has been conducted for many years to gain a better understanding of the flow instabilities associated with the bluff body and to improve or control their detrimental effects. A number of review articles on the subject of bluff body flow characteristics have been written, notably those of Berger and Wille (1972) [3], Bearman (1984) [4], Oertel (1990) [5], Williamson (1996) [6], Rockwell (1998) [7], Roshko (1955) [8] and Williamson and Govardhan (2004)[9].

1.1 Bluff body flow characteristics

A very comprehensive description of the behaviour of cylinder wake is described by Zdravkovich in his book on circular cylinder flow [1]. At extremely low Reynolds numbers ($\mathrm{Re} < 1$), called a creeping flow, the inertial forces are very small compared to the viscous forces as a fluid encounters a body allowing separation to occur at the rear stagnation point creating a symmetric flow with no vortex shedding. At a Reynolds number of approximately 4 to 5 a closed, symmetric near wake is formed with the free shear layers meeting at the end of the near wake called the confluence point. Figure 1.1a shows a steady separation regime that occurs at Reynolds numbers from 4 to 48 and is characterized by the closed near wake becoming elongated and unstable near $\mathrm{Re} = 30$ due to the Helmholtz instability. The onset of

sinusoidal oscillations of the shear layer begins at the confluence point causing the shear layer to roll up into Helmholtz vortices at crests and troughs, shown in Figure 1.1b. These vortices are then shed periodically from either side of the body, creating what is famously known as the von Kármán vortex formation [4] [10]. Gerrard studied the effects of vortex induced vibrations and described the process of fluid entrainment in the near wake of a bluff body. It was postulated that the circulation from the connected shear layer increased the strength of the growing vortex until it was strong enough to attract the opposing shear layer across the near wake. The vortex was then separated from the shear layer due to the approach of oppositely signed vorticity and shed downstream as Helmholtz vortices [2]. An illustration of the shear layer entrainment can be seen in Figure 1.2. The entrained shear layer may separate in three directions: (a) the largest part is engulfed into the growing vortex, (b) while another portion gets pushed into the developing shear layer, and (c) the final portion is temporarily entrained into the body causing a low pressure region of circulation. Flow over a bluff body is known to be predominantly two-dimensional until three-dimensional effects are introduced with Reynolds numbers greater than 180 [10]. At increasing Reynolds numbers up to 200 a fully periodic wake is formed with staggered laminar eddies shown in Figure 1.1c.

As Reynolds number increases above 200 a transition in the wake begins. Farther downstream, the laminar periodic wake becomes unstable and the transition gradually moves upstream until the eddy becomes turbulent during its formation. Typically the shedding frequency of the Helmholtz vortices can be quantified using the Strouhal number, which relates the shedding frequency (f_{s_0}), body diameter (D), and free stream velocity (U_∞) and is defined in equation 1.1. For cylinders at sub-critical Reynolds numbers, the average value of $St \approx 0.21$.

$$St = \frac{fD}{U_\infty} \tag{1.1}$$

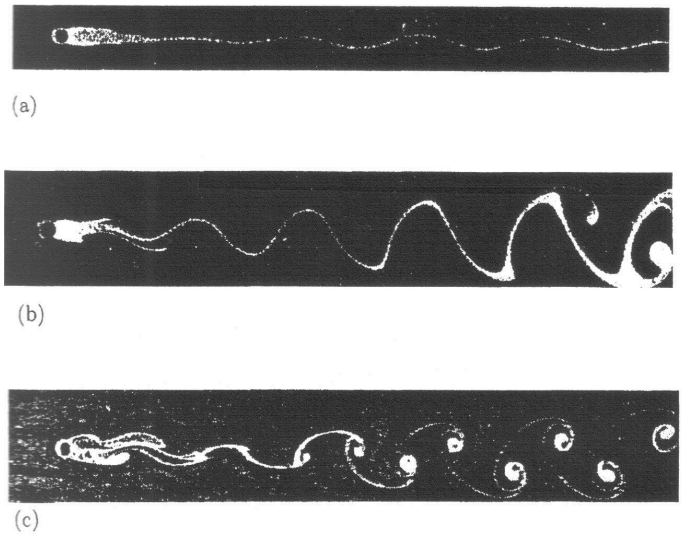

Figure 1.1: Periodic laminar wake: (a) Re = 54, (b) Re = 65, (c) Re = 102 [1]

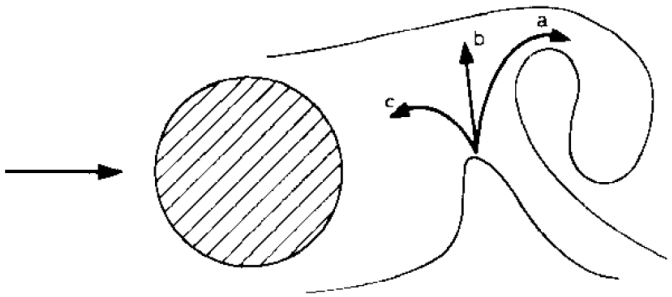

Figure 1.2: Vortex-formation showing entrainment flows [2]

Reynolds numbers ranging from 400 to approximately 20,000 are classified as a sub-critical state and experience a transition in the shear layers themselves. In this state the instability of the separating shear layer develops, decreasing the formation length and moving the transition point forward. Increasing the Reynolds number further causes the shear layers to become stronger and the instabilities farther downstream to increase in strength, pushing the transition to turbulence gradually upstream until the eddy becomes turbulent during its formation [1]. Above this range is a regime known as the critical state characterized by a transition in the boundary layers.[1]

The present research focuses on the sub-critical or shear layer transition regime with the Reynolds numbers used ranging from 12,000 to 24,000. The basic structure of the flow develops as the boundary layer encounters an adverse pressure gradient due to the divergent geometry of the cylinder and separates from the surface, forming a free shear layer. The boundary layer feeds vorticity into the free shear layer downstream of the cylinder causing it to roll up into Helmholtz vortices on the top and bottom of the cylinder which grow larger resulting in the formation of the von Kármán vortex formation. A region of slowly recirculating flow is formed directly behind the body called the near wake separation bubble. The separation bubble is bounded by the interacting shear layers from the top and bottom of the cylinder and is at a significantly lower pressure compared to the free stream pressure. This region is responsible for a large portion of the pressure drag associated with bluff bodies. The separation bubble ends at a downstream closure point that may be identified as a point where the shear layers cross the center line in the wake and begin to interact, or more accurately, at a point where the mean velocity is zero along the wake center line. [11]

1.2 Flow control

A large part of fluid mechanics research consists of attempts to control a fluid as it moves passed a body. Viscous effects dominate most practical applications and give rise to many complicated flow regimes. At lower Reynolds numbers the dominant force on a body is mainly attributed to skin friction, but as the Reynolds number exceeds a critical value, vortex shedding occurs generating a significant amount of pressure drag. Vortex shedding gives rise to a plethora of challenging flow characteristics to combat. A few of the major issues include structural vibrations, acoustic noise, and large increases in the mean drag and lift fluctuations. Many areas that could benefit from effective flow control include offshore platforms, bridge pylons, cables and ropes used for mooring, heat exchanger tubes, cooling towers, smoke stacks, tall buildings, and aircraft control surfaces and antennae to name a few. In an attempt to improve the flow characteristics over bluff bodies, a variety of flow

control techniques have been developed and are reviewed by Choi et al [12]. The two main categories of flow control are:

(1) Passive flow control

(2) Active flow control

1.3 Passive flow control

Passive flow control techniques are classified by a modification of the body or surface geometry to alter the flow characteristics.

1.3.1 Body geometry and surface alterations

Research conducted by Owen and Bearman [13] showed a significant reduction in drag of up to 47% for a cylinder with a sinuous axis and about 25% for a cylinder with hemispherical bumps along the span. It was shown that if the separation line of a bluff body is forced to be sinuous , then there is a suppression of the vortex shedding and consequently a reduction in drag. Nakamura and Igarashi [14] achieved a reduction in drag and fluctuating forces for a cylinder in a cross-flow by attaching cylindrical rings along its span. Separation bubbles on both sides of the ring allowed the recovery of the low pressure region behind the cylinder. A wake comparison between a smooth cylinder and grooved cylinder was conducted by Liu, Shi, and Yu [15]. The length of the recirculation zone in the near wake was shown to be extended by 18.2% for the grooved cylinder due to the small-scale recirculating zones produced by the cavities, decreasing drag. Shoa, Wang, and Wei [16] added a narrow strip parallel to the cylinder surface at varying angles from the trailing stagnation point. It was found that at a range from 30 to 50 degrees the obstructive strip successfully suppressed the periodic wake. Ahmed et al [17] investigated the flow characteristics over a wavy cylinder. The wake behind the nodal points of attachment was found to be more narrow and have a faster rate of velocity recovery compared to the saddle points of attachment. A splitter plate was investigated by a number of researchers, Anderson and Szewczyk [18], Bearman [19], Hwang

et al. [20], Kwon and Choi [21], Ozono [22], and Roshko [8]. The interaction between the top and bottom shear layers was delayed in the wake, suppressing vortex shedding. As a result, the base pressure behind the bluff body increased, resulting in a drag reduction.

1.3.2 Surface alterations

Helical strakes have been implemented by Scruton and Walshe [23], Woodgate and Mabey [24], Hirsch, Ruscheweyh, and Zutt [25], Wong and Kokkalis [26], and Every, King, and Weaver [27]. This method of passive flow control is able to reduce the force fluctuations, which decreases the vibration induced by Kármán vortex shedding. Eckmekci and Rockwell [28] placed a single span wise wire in the upper shear layer on a circular cylinder and observed the effects on the near wake. The wire was able to decrease the impact of the Kármán instability when it was placed at certain critical angles, which led to a contraction of the time-averaged flow characteristics of the wake. Kareem and Cheng[29] investigated the pressure and force fluctuations on roughened cylinders by placing a trip wires at ± 65 degrees and separation wires at ± 115 degrees. With the wires positioned at the optimal locations, the surface pressure measured was characteristic of higher Reynolds number flows with three dimensional features. By placing rectangular tabs spanwise at optimal locations along the separation point of a circular cylinder, Yoon [30] achieved a drag reduction. The tabs caused a phase mismatch in the vortex shedding process, which broke up the naturally two dimensional vortices creating high levels of mixing in the wake.

1.4 Active flow control

Active flow control methods are characterized by introducing additional energy to the flow. Generally, when time-periodic forcing is applied, the vortex shedding in the wake becomes locked in-phase with the forcing that is applied [31]. A few techniques, however, have been successful in reducing drag and attenuating the von Kármán vortex shedding.

Tokumaru and Dimotakis [32] experimented with the effects of a circular cylinder at an oscillatory high-frequency of rotation to control the wake. The sinusoidal rotation was performed at specific frequencies, f and a normalized peak rotational rate of Ω. The peak rotation rate was chosen so that the circumferential velocity of the cylinder would be comparable to the velocity just outside the boundary layer. The Strouhal number was varied between 0.17 and 3.3. The greatest control authority was observed when the forcing frequency was in sync with the shedding structures. They concluded that the mechanism by which the wake can be controlled have more to do with the ejection of circulation into the flow instead of the behavior of the flow in the absence of forcing. A base bleed technique was implemented by Bearman [33] and Wood [34]. It was found that the bleed decreased the strength of the vortex formation which decreased the profile drag. As the strength of the base bleed increased, the formation of the vortices formed farther downstream. An examination of the wake of a transverse vibrating cylinder was performed by Koopman [35], showing that the coherence of separation points along the span is induced when the vibration is driven at the vortex natural shedding frequency. As a certain amplitude of vibration was reached, the vortex formation experienced a dramatic change. Originally, the vortex filaments of the non-vibrating cylinder shed in a slanted direction and when the cylinder was vibrated, the vortex filaments jumped to align themselves parallel with the cylinder, reducing the lateral spacing between the wake vortices. This phenomenon required a displacement of about 10% of the cylinder diameter for each tested Reynolds number. A similar study was conducted by Ongoren and Rockwell [36] using cylinders of various cross-sectional geometries. The excitation frequency, f_e, was at a frequency relative to the formation frequency, f_o. At a critical amplitude, both the subharmonic frequency ratio of 0.5 as well as 1, the near wake structures became phase-locked to the cylinder motion, but in two different synchronization mechanisms. Oscillations at a frequency close the that of the shedding frequency resulted in a phase shift of approximately π. The formation length was significantly reduced and an increase in the angle of inclination of shedding was seen in the base region. Just above this

frequency ratio the shedding switches phases to the opposite side of the cylinder including a decrease in inclination of the base region to about zero. Over a wide range of forcing frequencies, the near wake rapidly recovered to a large scale antisymmetric mode similar to the Kármán vortex formation through the interaction of the cylinder's own vortices of alternate signs. A study was done by Fransson, Konieczny, and Alfredsson [37] on the flow around a circular cylinder subjected to continuous suction or blowing. The blowing and suction rate was varied compared to the free stream velocity and given as Γ. The maximum suction was 40% of the free stream and the maximum blowing was 60% of the free stream velocity. It was shown that relatively low levels of suction or blowing had a large effect on the flow around the cylinder. Suction strengths above $\Gamma \approx$ -2.5 moved the separation line farther aft resulting in a smaller wake and a drag reduction of up to 70%. When blowing was applied through the porous cylinder, the opposite effect was observed and an increase in drag occurred.

A different method of active flow control that has been used in the past involves applying sound waves to the flow. Blevins [38] and Detemple-Laake and Eckelmann [39] are a few of the researchers that have conducted this type of research. Blevins' research was conducted in the Reynolds number range of 20,000 to 40,000. The results showed a correlation between sound and span-wise vortex shedding detected by four flush film sensors placed on the cylinder at different span-wise locations. Irregular signals were obtained when the excitation was absent, but when a 143.5 dB sound wave was applied to the flow at the shedding frequency, the four signals were approximately in-phase with less irregularity. This showed that the application of the periodic excitation was able to synchronize the shedding frequency and increase its strength. Detemple-Laake and Eckelmann superimposed sound waves on the flow over a cylinder in the mean flow direction to investigate the coupling mechanism. The Reynolds number range was selected to be between 53 and 250 with the ratio of sound frequency to natural shedding frequency ranging from 0.5 to 4. Twelve different wake

structures were found depending on the sound frequency and amplitude that were categorized into three groups: structures independent of the ratio of sound frequency and natural shedding frequency, synchronization, and the natural shedding frequency locking onto the sound frequency.

1.5 Present research

Past research on internal periodic forcing has been reported by Huang [40] and Fujisawa and Takeda [41]. Huang's work mainly focused on Reynolds numbers in the range from 4,000 to 8,000. It was found that only weak excitation was needed to suppress the formation of periodic vortex shedding. It was also found that vortex shedding on both sides of the cylinder may be suppressed even when only one shear layer was affected. This observation showed that the vortex shedding instabilities were a result of the interaction between parallel shear layers. Fujisawa and Takeda [41] focused on periodic forcing through a slit at Reynolds number of 9,000. They altered the location of the slit relative to the attachment point and forcing amplitude to obtain a drag reduction of up to 30%. The optimum placement of the slit was found to be just behind the separation point and an excitation frequency near the unstable frequency of the separating shear layer. Bhattacharya [42] conducted research on the effect of three dimensional forcing on the wake of a circular cylinder at higher Reynolds numbers of 24,000 and 45,000, which introduces global modes with larger amplitudes. A hollow circular cylinder with diametrically opposite sinusoidal slits were used to introduce three dimensional forcing to effect the shear layers and a drag reduction of almost 50% was obtained for a Reynolds number of 24,000.

The objective of the present work was to explore the effects of in-phase and out-of-phase forcing on the turbulent wake behind a circular cylinder using two-dimensional forcing. The forcing provided by the acoustic driver diaphragms acted as a synthetic jet that added momentum to the shear layer at the onset of separation through the slits and modified the flow in the wake.

Chapter 2

Experimental Set-up

The cylinder model used in this study had two straight slits on opposite sides. Each end of the cylinder was connected, via copper tubing, to a sub-woofer to apply the periodic forcing at the desired frequencies and blowing coefficients. Tests were performed at Reynolds numbers of 12,000 and 24,000. A constant temperature anemometer (CTA) was used to measure the air speed of the flow through the slits ensuring the proper blowing coefficient, and measure the wake power spectra by computing PSD. This illustrated the affect of the periodic forcing on the natural shedding frequency of turbulence statistics, vorticity, and energy distributions in the wake. Particle image velocimetry (PIV) was also performed to document the formation of complex wake structures. Post processing of PIV data consisted of proper orthogonal decomposition (POD) to quantify the dominant modes in the wake. The drag coefficient for each case was calculated from pitot surveys of the wake using the momentum deficit method.

All experiments were conducted in the Auburn University 3 ft x 4 ft, closed circuit, low speed wind tunnel. The tunnel speed was monitored electronically and also with a manometer. The free stream turbulence level was found to be approximately 0.5% and the non-uniformity was less than 1%.

2.1 Details of cylinder and test set-up

The model used was a hollow resin cylinder made on a three-dimensional printer in the Air Force Research Lab at Wright Patterson Air Force Base. A partition in the middle of the cylinder allowed the periodic forcing from each driver to individually exit the slits on either side. Figure 2.1 shows the cylinder model which had an effective aspect ratio of 23 and

slit lengths of 6.5 inches. Figure 2.2 show a cross section view of the cylinder and Figures 2.3 and 2.4 illustrate the in-phase and out-of-phase forcing, respectively. The model was installed between two walls mounted in the test section shown in Figures 2.5 and Figure 2.6.

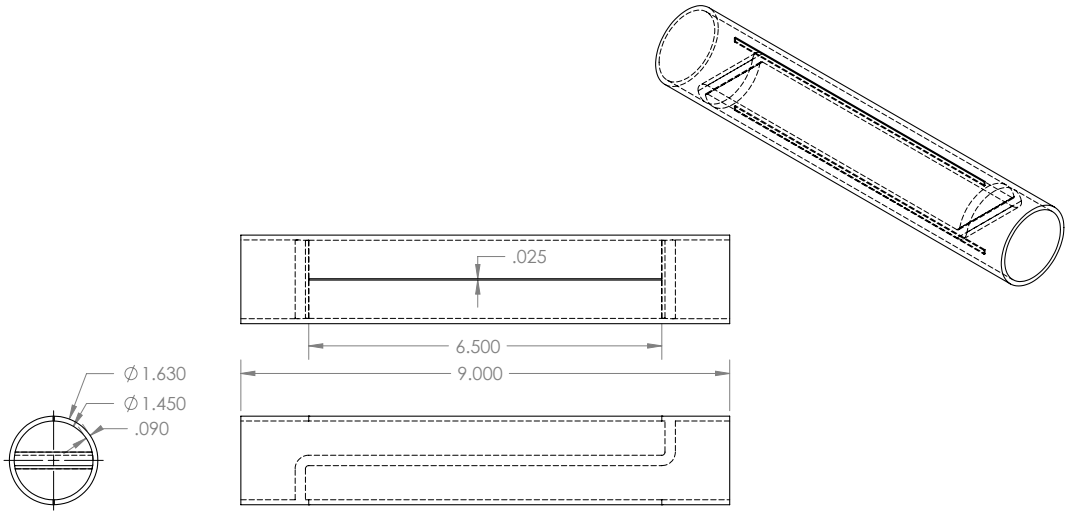

Figure 2.1: Cylinder model

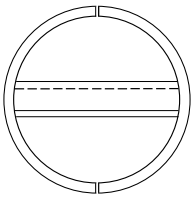

Figure 2.2: Cross section of hollow partitioned cylinder

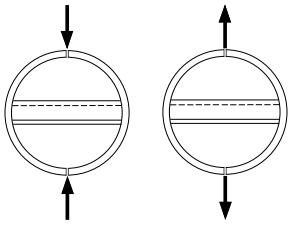

Figure 2.3: Periodic forcing (IP)

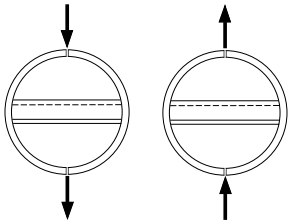

Figure 2.4: Periodic forcing (OP)

The wall inserts were made out of 1 inch thick particle board with large acrylic windows for PIV measurements. The walls were held in place with the help of aluminum L-brackets bolted to the test section floor. The periodic forcing supplied by the drivers traveled through copper piping that was attached to each end of the cylinder, through a round opening in the front end of the acrylic wall, and up through the ceiling of the test section to the drivers.

2.1.1 Drivers

The periodic forcing applied to the flow was supplied by two sets of drivers. The low frequency forcing (11.5 Hz – 46 Hz) was generated from two Infinity Reference 12 inch sub woofers and the high frequency forcing was generated from two Infinity Reference 8 inch (1000 watt max). drivers. The drivers were connected to wave form generators (Wavetek model 182A and 132) to provide a sinusoidal wave signal and desired frequencies. The signal was monitored on an oscilloscope and passed through separate external power amplifiers (MB Dynamics SS250VCF for the 12 inch drivers and an MBIS Model SS500 for the 8 inch drivers) requiring a range of nine to sixteen volts. A polarity reversing box was constructed from two switches in order to change the phase of the drivers. It was found that at the higher frequencies, a larger voltage was required to generate the desired periodic forcing. Special care was taken to prevent any damage to the driver voice coils.

2.1.2 Data acquisition system

A National Instruments data acquisition board (NI USB-6210) was used to acquire all of the data generated by the constant temperature anemometers. The raw data was then

processed in LabVIEW 10.0.1 using a continuous voltage acquisition program and recorded to a text file for spectrum analysis using MATLAB.

2.1.3 Constant temperature anemometers

Constant temperature anemometry was used to the determine the Strouhal number of the wake. A single bridge miniCTA system from DANTEC Dynamics was used to acquire wake spectra. The frequency response of the system was approximately 6 kHz at 30 m/s. The wire was made of platinum plated tungsten with a diameter of 5 microns and a length of 1.25 millimeters. A maximum operating temperature recommended by the manufacturer was 300°C, but a temperature of only 200°C was selected to ensure the longevity of the wire.

A two degrees of freedom Velmax traverse was placed above the test section to provide axial and transverse probe movement along the test section. Probe access to the test section was available through a slot cut in the acrylic ceiling. The traverse was manually controlled, via Velmex VP9000 controller, to specific locations measured in the test section. The CTA probe holder was attached to a streamlined support to reduce the vibration, which was securely fastened to the traverse controller.

2.1.4 Wake pressure survey

A pitot probe was secured to the traverse system and connected to a Validyne DP45-16 pressure transducer to obtain the dynamic pressure required to calculate the drag coefficient (Appendix B.1). The transducer was read by a volt meter which sent the pressure data to a National Instruments USB-6008 data acquisition board. A LabVIEW program was developed to record the pressure measurements as the traverse moved in increments of one-tenth of an inch in the transverse direction throughout the wake of the cylinder from two to ten diameters downstream.

2.1.5 Particle image velocimetry (PIV)

Particle image velocimetry is a well known flow diagnostic technique. The system uses a high energy light source, in this case, a YAG laser, to form a thin light sheet in the desired plane of interest to illuminate the particulates in the flow shown in Figure 2.7. A high speed camera is integrated into the laser timing system to capture successive images to be analyzed.

A New Wave Research Solo III dual pulse laser was used for PIV measurements. The light beam was passed through three lenses consisting of a diverging lens, a converging lens to focus the beam, and finally a cylindrical lens to generate the light sheet.

The images were captured using a Cooke Corporation Sensicam high speed camera of 1376 x 1040 pixel resolution with a Tamron 75mm lens. The interrogation window was 32 x 32 pixels.

The camera timing was synced with the laser pulses using two quantum composer pulse generators (Model 9514). One generator was used to control the laser pulses and the other was used to control the camera shutter. The timing between images was set to 50 μs. 1155 image pairs were taken for each case.

An Antari Z-800II smoke generator was used to seed the flow with smoke particles and was placed in the diffuser section of the closed circuit wind tunnel. A remote control was used to trigger the production of smoke. The fog liquid mixture (glycol and water) was heated and vaporized by passing through a heat exchanger and then dispersed into the flow. By placing the smoke generator in the diffuser, the particles had time to disperse throughout the flow before they reached the test section.

CamWare 2.19 software was used to record the captured image pairs on a computer system and Fluere version 0.9 was used to process the image data using cross correlation.

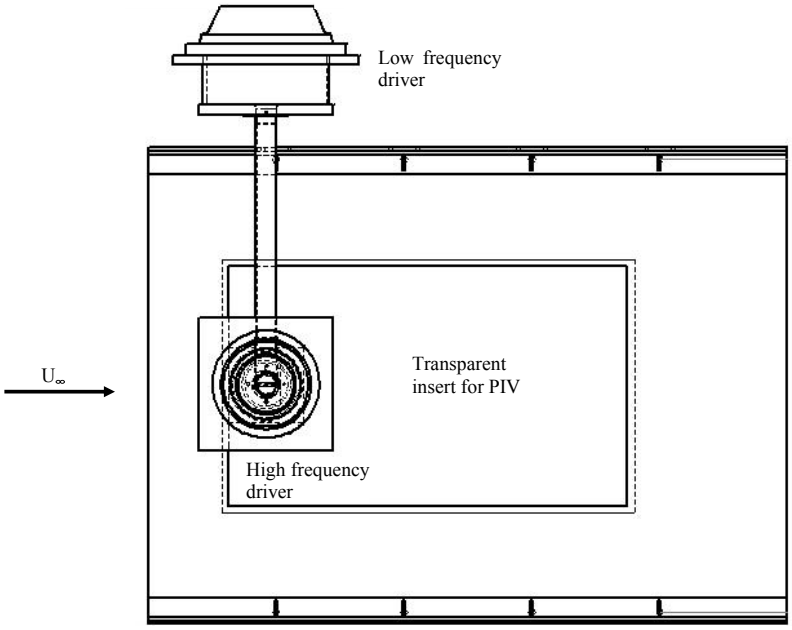

Figure 2.5: Side view of PIV wall set-up

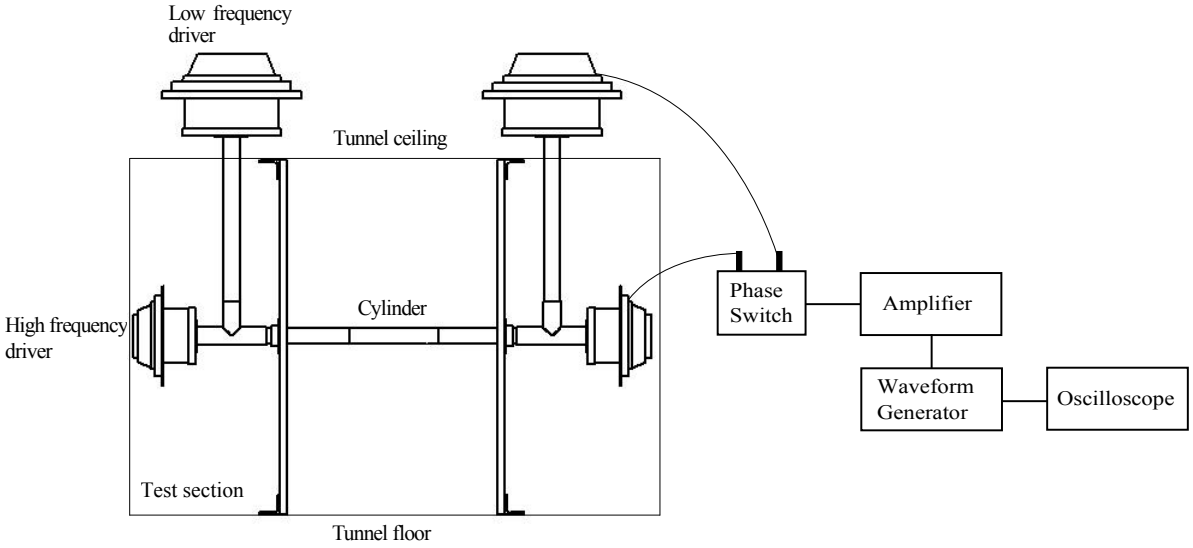

Figure 2.6: periodic forcing set up

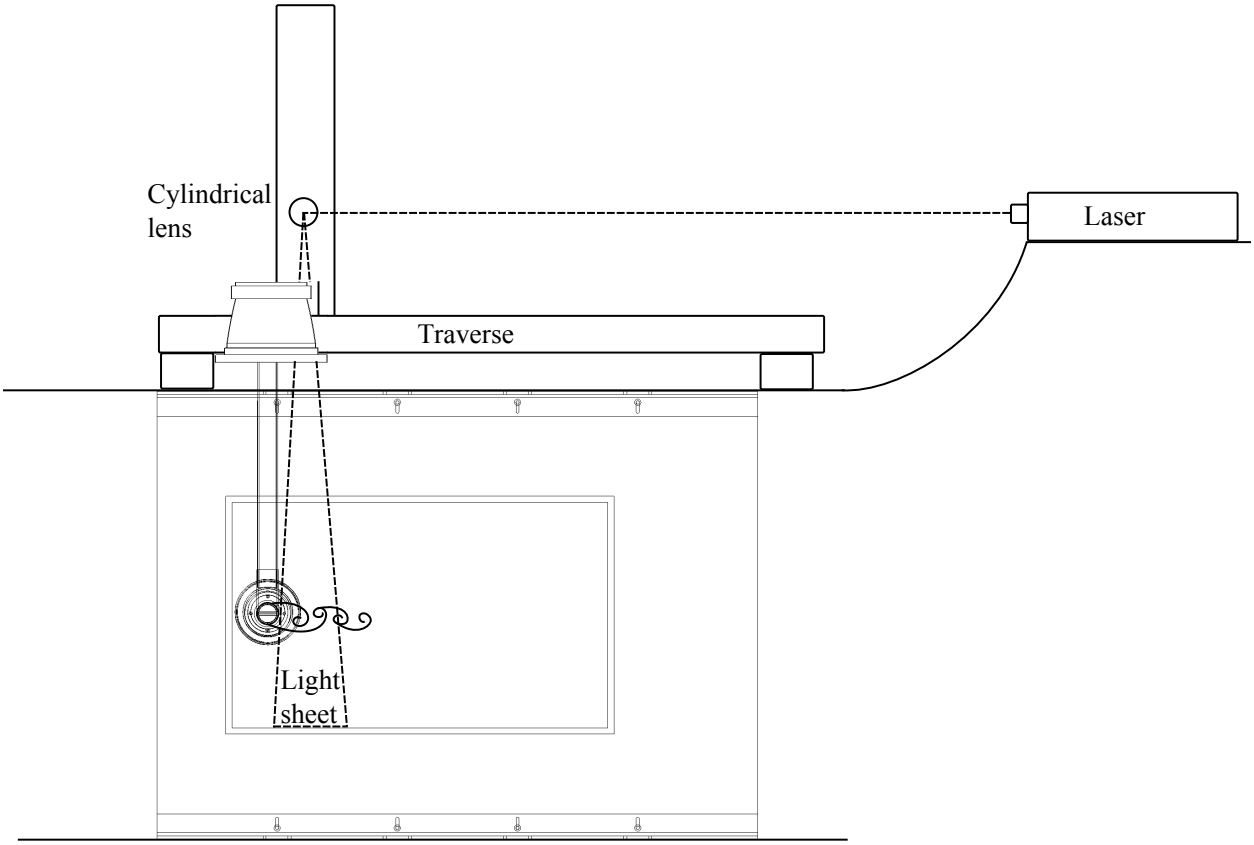

Figure 2.7: Particle image velocimetry test set-up

Chapter 3

Results and Discussion

The tests were conducted at free stream velocities of 15 ft/sec and 30 ft/sec resulting in Reynolds numbers of approximately 12,000 and 24,000, based on the cylinder diameter. The cylinder was positioned between the two support walls with the straight slit 90 degrees from the forward attachment line, which was discovered to be the optimal angle by Fujisawa and Takeda [41]. The single wire constant temperature anemometer was placed directly above the slit to measure the slit jet velocity. At each forcing frequency the blowing coefficient was calculated and the required voltage was recorded to ensure repeatability. The C_μ values and corresponding voltages were listed in Tables A.2 and A.3.

3.1 Wake power spectra

The DANTEC single hot wire was placed at a position of $\frac{y}{D} = 0.5$ and $\frac{x}{D} = 4$, which was verified to be the optimal position for the upper shear layer using a Hewlett-Packard spectrum analyzer. The natural shedding frequency was found to be 23 Hz for a Reynolds number of 12,000 and 46 Hz for a Reynolds number of 24,000. The forcing frequencies were chosen based on multiples of the natural shedding frequency. The maximum frequency tested was 184 Hz, which was $4f_{s_0}$, due to driver effectiveness and power limits. The calculated power spectra for each Reynolds number is based on a DC signal level.

Figure 3.3 compares the effect of the different forcing frequencies while operating in the in-phase forcing mode. For the no forcing case the slits were sealed to ensure there was no momentum loss due to the openings. A sharp peak can be seen at the top of the figure at 23 Hz indicating the natural shedding frequency of the cylinder. A sub-harmonic driver frequency of 11.5 Hz, or $\frac{1}{2}f_{s_0}$, produced a decrease in the magnitude of the natural shedding

frequency, but also introduced a small harmonic peak at the excitation frequency. As the forcing frequency was increased to a value equal to the natural shedding frequency of 23 Hz, an increase in the magnitude of the spectral peak was observed. At 46 Hz the magnitude of the shedding frequency began to decrease indicating an attenuation of the natural shedding frequency. This was also observed in the frequencies greater than $2f_{s_0}$, where the shedding frequency was damped out almost entirely. A special case using a random noise input was also tested with surprising results. The broadband wavelength of the signal was able to completely eliminate the shedding peak as can be seen in each case. A plot of the random noise time history and power spectrum can be seen in Figures 3.1 and 3.2.

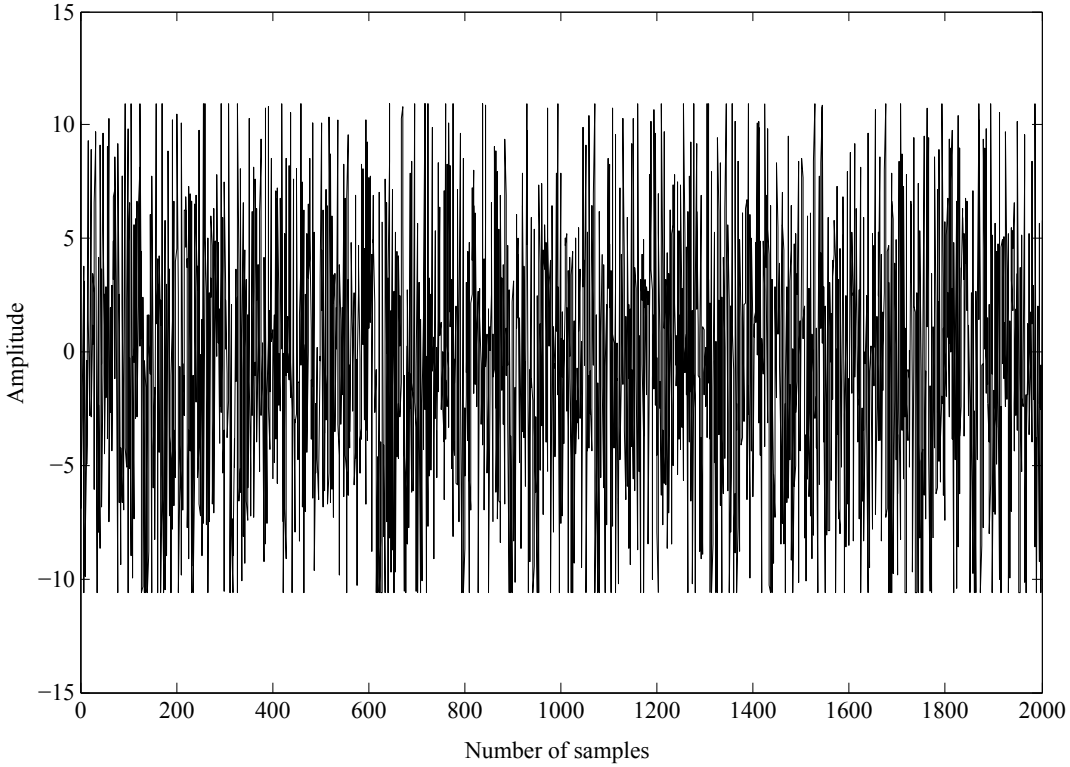

Figure 3.1: Time history of random noise signal

The results of the forcing cases with the drivers in the out-of-phase mode can be seen in Figure 3.4. In this configuration, a spectral phase shift occurred indicated by the peaks in the spectral plot matching or locking on to the excitation frequency. At $f_e = 92Hz$,

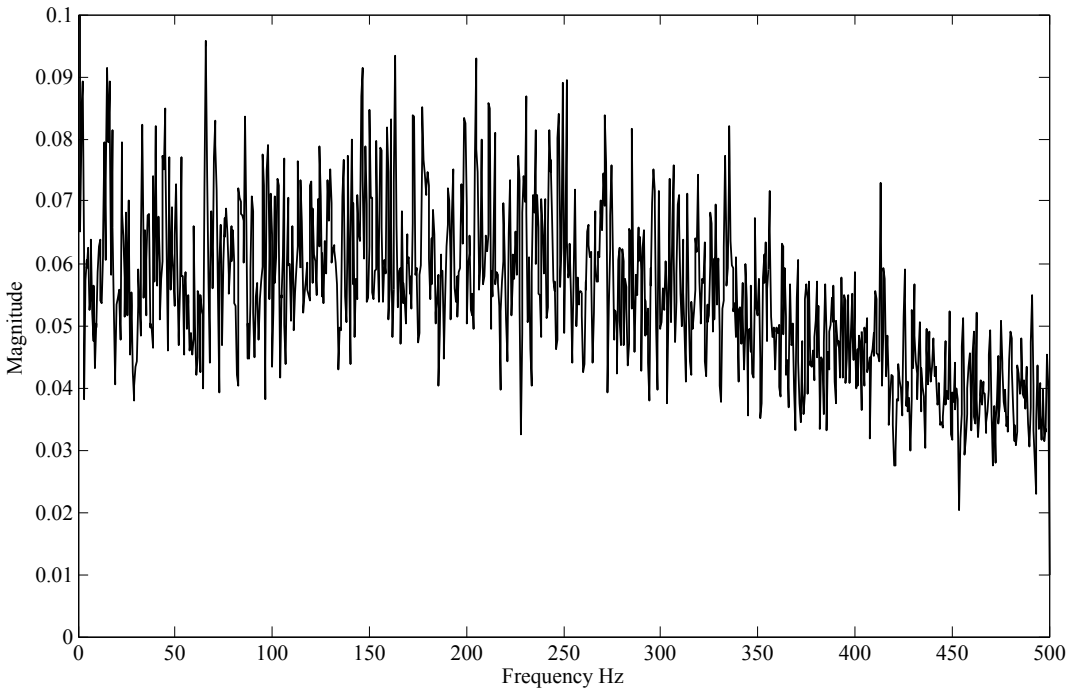

Figure 3.2: Power spectra of random noise signal

the spectral peak was eliminated all together, signifying a successful suppression of the von Kármán vortex formation. Similar results were seen in the random noise forcing as well.

The spectral plots for the in-phase and out-of-phase driver modes for a Reynolds number of 24,000 are shown in Figures 3.5 and 3.6. Similar trends were observed at this Reynolds number with larger peak magnitudes. However, higher amplifier voltages were required to supply enough power to generate the correct blowing coefficient.

From the data analyzed, it is clear that with in-phase forcing at frequencies greater than $2f_{s_0}$ at a Reynolds number of 12,000 and $4f_{s_0}$ at a Reynolds number of 24,000, the excitation frequency was able to successfully suppress the natural shedding frequency. Detemple-Laake and Eckelmann's work [43] investigated the coupling mechanisms of the generation of circular cylinder wake as sound was superimposed in the mean direction of the flow. It was observed that the natural shedding frequency would actually lock on to the sound frequency, which was supported by the out-of-phase forcing cases in the present research. The flow visualization study by Hsiao [44] supports this observation as well by showing that the basic

mechanism for the elimination of von Kármán vortices in the shear layer was by disrupting their formation. The periodic forcing technique was able to accomplish this task by breaking up the strengthening vortices into smaller eddies near the cylinder. Also, depending on the phase the forcing was applied, the vortex formation occurred at the same frequency as the excitation frequency, as seen in the out-of-phase periodic forcing. Bhattacharya's [42] results showed that using three dimensional forcing with a sinusoidal slit the natural shedding peak of a circular cylinder can be eliminated with forcing frequencies greater than or equal to $2f_{s_0}$ at Reynolds numbers of 24,000 and 45,000. His research concluded that the main factor for the cancellation of shedding vortices was the three dimensionality introduced through the sinusoidal slit which depends on the slit geometry, bowing coefficient, and the excitation frequency. The present case used a straight slit geometry, which introduced only two dimensional disturbances to the growing shear layers.

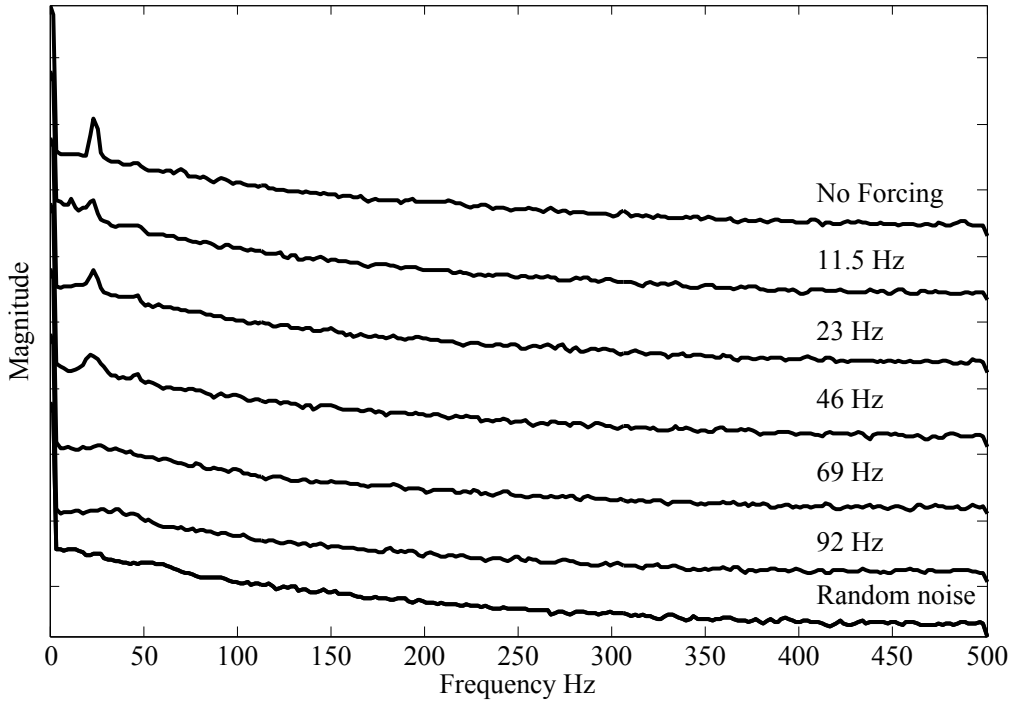

Figure 3.3: Power spectra for Re = 12,000, IP

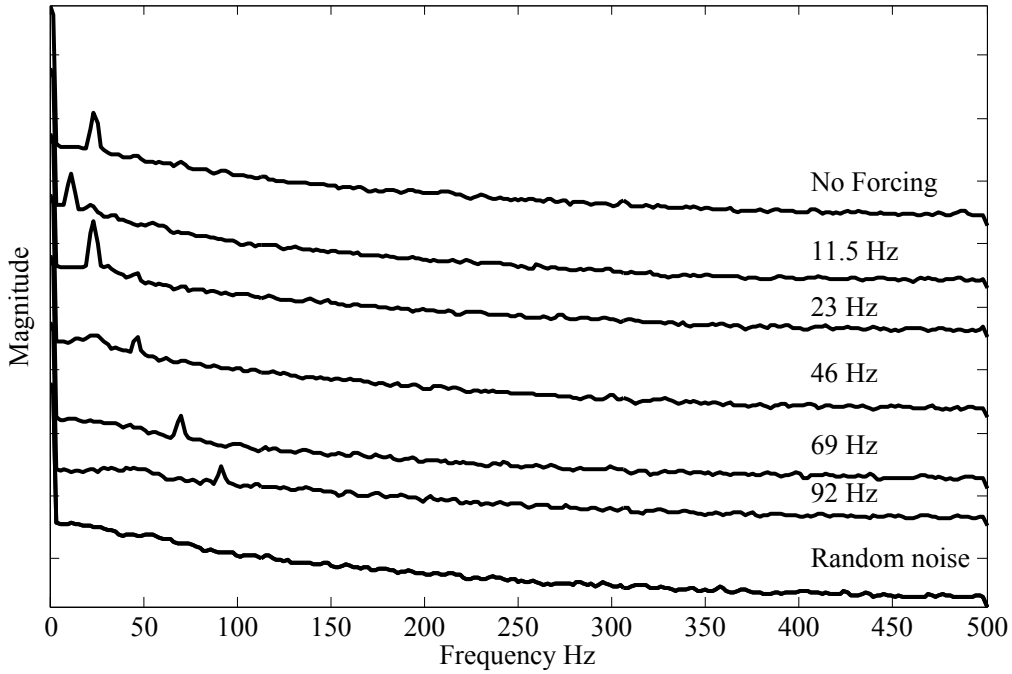

Figure 3.4: Power spectra for Re = 12,000, OP

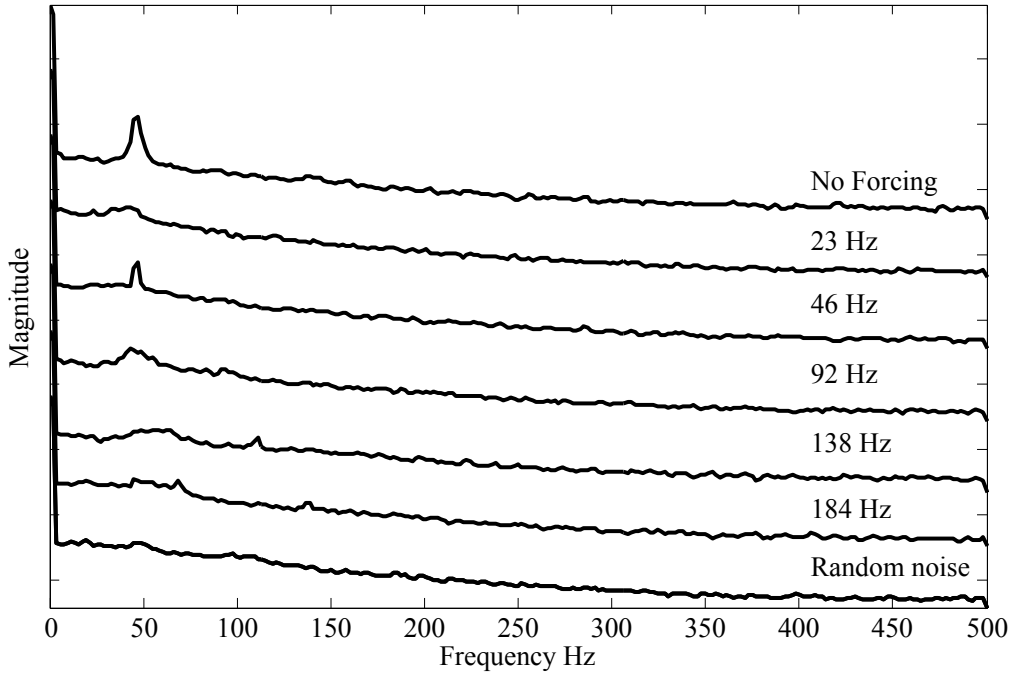

Figure 3.5: Power spectra for Re = 24,000, IP

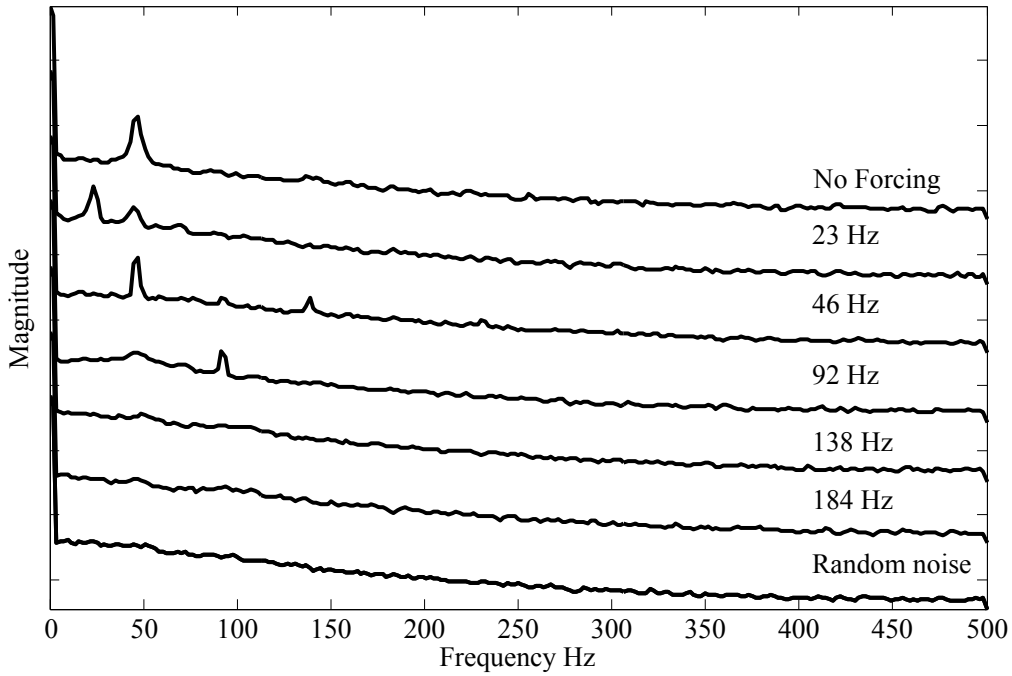

Figure 3.6: Power spectra for Re = 24,000, OP

3.2 Mean wake quantities

Pressure surveys were taken using a pitot probe connected to a pressure transducer and traversed vertically ±5 diameters at each downstream location, up to 10 diameters. Mean velocity profiles of the wake were formed at each excitation frequency, and wake half-width and drag coefficient values were calculated to describe the excitation effects.

Mean velocity profiles at x/D = 4 can be seen in Figures 3.8 and 3.9. The drag coefficients were calculated using the wake momentum deficit method, described in Appendix B.1, and are presented for Reynolds numbers of 12,000 and 24,000 in Tables 3.1 and 3.2 respectively. One would deduce that the in-phase driver mode would be more effective at reducing the cylinder drag due to the superior results illustrated in the power spectrum density plots discussed earlier. This was also supproted by the wake velocity profiles. The drag data shows a larger reduction using the in-phase forcing technique as opposed to the out-of-phase mode due to a more successful suppression of the von Kármán vortex formation. In the near wake of the cylinder at Re = 12,000, and at 2 diameters downstream a drag reduction of 5.5% was observed for the in-phase case and 4% in the out-of-phase mode. At a location of 4 diameters downstream a more significant drag reduction was observed with 28% for in-phase and 26% for out-of-phase. The sub-harmonic excitation frequency amplified the instabilities present in the flow, resulting in a 1% increase in drag with the in-phase excitation and a 1.2% increase for the out-of-phase mode. As the excitation frequency was increased the drag continued to decrease until it reached a minimum at $f_e = 92$ or $4f_{s_0}$. 6 cylinder diameters downstream a decrease in drag of 20% and 18% was seen for the in-phase and out-of-phase modes respectively. The in-phase mode had less of an effect farther downstream at 8 diameters with a drag reduction of 16%. The out-of-phase case produced a 10% reduction. At 10 diameters downstream the in-phase mode improved the drag characteristics by 27% and 25% for the out-of-phase mode.

The tests performed at a Reynolds number of 24,000 showed an interesting trend. In analyzing the drag coefficients at each location and comparing them to the lower Reynolds

number case (in-phase: 5.5%, out-of-phase: 4%) it was found that at downstream locations closer to the cylinder, for example 2 diameters downstream, the periodic forcing had a greater effect in the reduction of drag with a 9% reduction using in-phase forcing and 6% reduction using the out-of-phase forcing. However, at downstream locations greater than 8 diameters the drag reduction decreased. This was in part due to the increased amount of kinetic energy in the higher speed flow causing the positive effects of the periodic forcing to be less at greater downstream locations.

The wake half-width was calculated from the wake deficit data. The wake half-width, illustrated in Figure 3.7, is defined as the distance from the center of the wake to a location where the velocity defect is half of the maximum. Figures 3.10 and 3.11 show the variation of the wake half-width at each Reynolds number and excitation frequency. It is known that as the wake progresses downstream, the wake width increases. This was evident by the positive slope of the no forcing case seen at each Reynolds number. In Figure 3.8a the 11.5 Hz excitation frequency was shown to increase the half-width at each downstream location, which occurred with $f_e \leq 2f_{s_0}$. When an excitation frequency of $f_e > 2f_{s_0}$ was applied, seen in Figure 3.8d, the half-width was smaller when compared to the no forcing case, which indicated a narrowing of the wake.

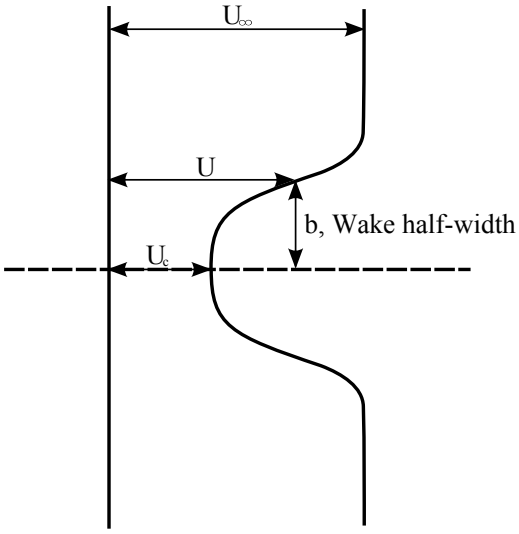

Figure 3.7: Description of the wake half-width

Figures 3.12 and 3.13 illustrate the possible effects of the periodic forcing for each forcing mode. When utilizing the in-phase driver mode, the periodic forcing effects both shear layers at the same time either by sucking air in through the slits or blowing it out. This could either shrink or expand the wake by subtracting or adding momentum to the forming eddies in the shear layers. The natural tendency for vortex shedding is to shed alternately. If the side of the shear layer that is about to shed an eddy is submitted to suction, energy is taken from the shear layer and the forming eddy will be weaker. If the side of the shear layer that is not shedding an eddy is subjected to blowing, momentum is added to this side and may compete and disrupt the opposite shear layer, reducing the wake periodicity. Figure 3.13 shows the possible effect of out-of-phase forcing. An amplification of the natural instability may occur depending on the side the vortex sheds and the natural shedding frequency may also coincide or lock-on to the excitation frequency. If the excitation occurs in the opposite phase of the natural vortex shedding, the shear layer experiences a reduction in energy due to suction while the opposite shear layer experiences an increase in fluid momentum. In a case where the excitation frequency is equal to the natural shedding frequency, the periodicity is disrupted with the opposite phase of the natural shedding frequency, dampening out the vortex formation.

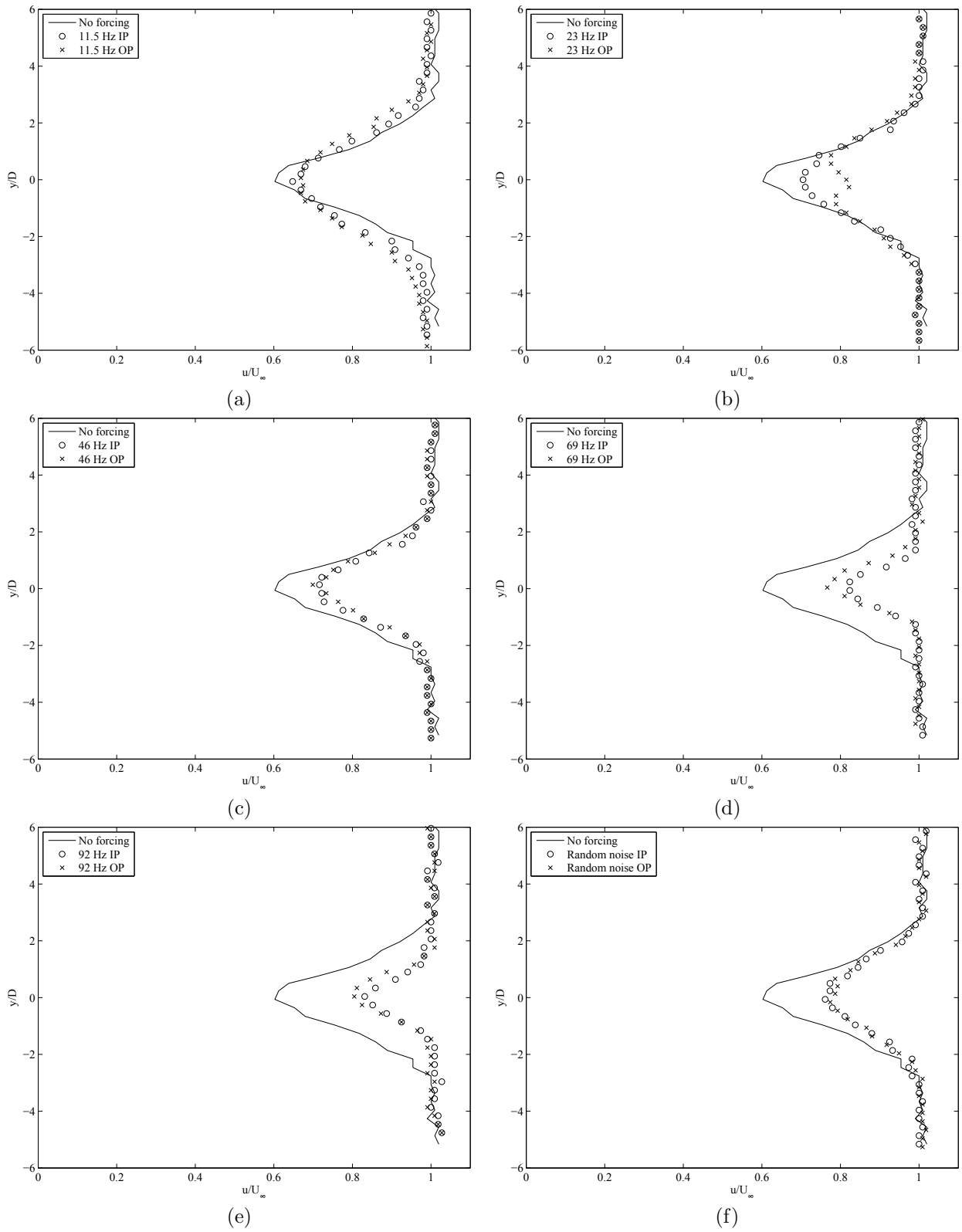

Figure 3.8: Mean velocity profile (x/D = 4, Re = 12,000)

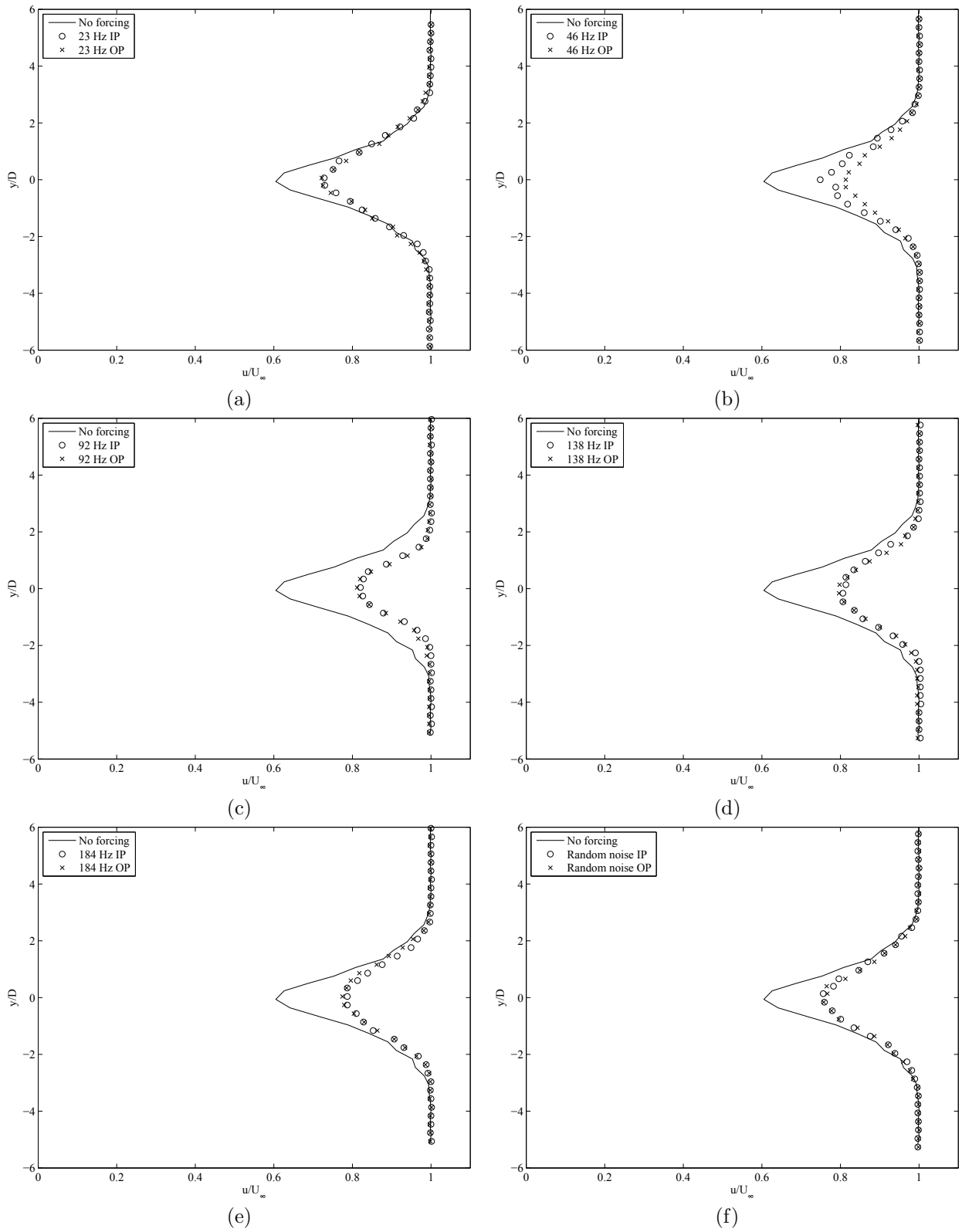

Figure 3.9: Mean velocity profile (x/D = 4, Re = 24,000)

Table 3.1: Coefficients of drag at different downstream locations

Re = 12,000	Location downstream									
Frequency	2D		4D		6D		8D		10D	
(Hz)	In	Out	In	Out	In	Out	In	Out	In	Out
NoForcing	1.837		1.812		1.8123		1.7923		1.7784	
11.5	1.93	1.9846	1.829	1.834	1.7599	1.8315	1.8381	1.8914	1.827	1.9033
23	1.9023	1.9452	1.4185	1.4003	1.7298	1.7353	1.7845	1.8595	1.7854	1.8105
46	1.8364	1.8682	1.3845	1.3848	1.6945	1.7157	1.7324	1.7221	1.762	1.7617
69	1.7377	1.7857	1.3092	1.3273	1.4632	1.4808	1.5903	1.6066	1.7184	1.7428
92	1.7501	1.76	1.3048	1.3266	1.4577	1.4791	1.5964	1.6171	1.2929	1.3223
Noise	1.7967	1.8218	1.4601	1.4769	1.4468	1.4806	1.4922	1.6547	1.6280	1.6490

Table 3.2: Coefficients of drag at different downstream locations

Re = 24,000	Location downstream									
Frequency	2D		4D		6D		8D		10D	
(Hz)	In	Out	In	Out	In	Out	In	Out	In	Out
NoForcing	1.9621		1.7614		1.6984		1.6349		1.6464	
23	1.8964	1.8909	1.2589	1.2485	1.7215	1.7026	1.7396	1.7225	1.7587	1.7346
46	1.8369	1.8427	1.3154	1.4030	1.8031	1.8514	1.8044	1.8341	1.8180	1.8319
92	1.8618	1.8581	1.2448	1.2525	1.5553	1.4546	1.9036	1.9158	1.8905	1.9055
138	1.8397	1.875	1.1721	1.189	1.334	1.391	1.397	1.4224	1.8122	1.858
184	1.7868	1.8863	1.1332	1.1748	1.3494	1.3698	1.7328	1.4486	1.7174	1.5552
Noise	1.8559	1.8421	1.1463	1.1457	1.3334	1.3346	1.517	1.5081	1.5175	1.5126

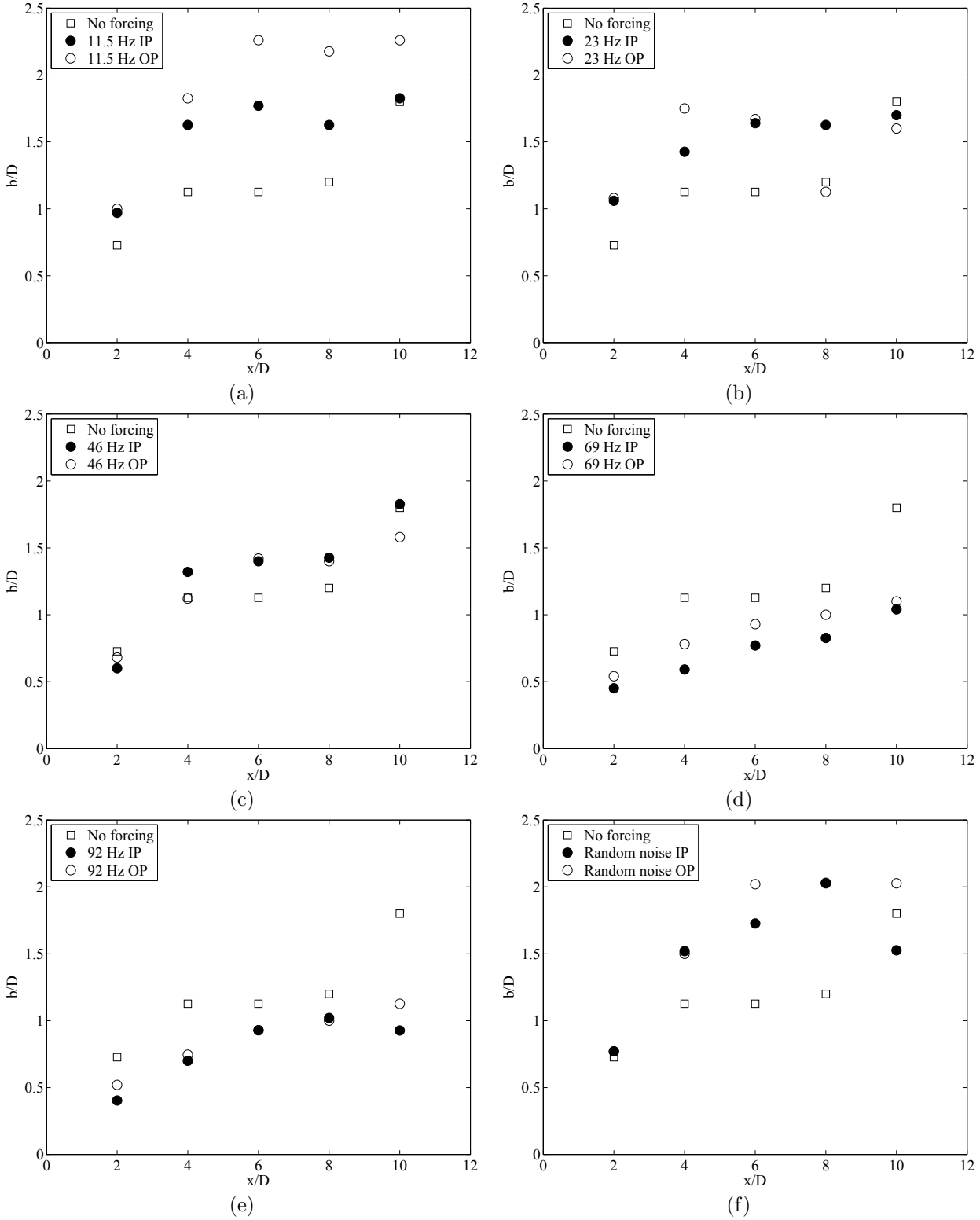

Figure 3.10: Variation of wake half-width (Re = 12,000)

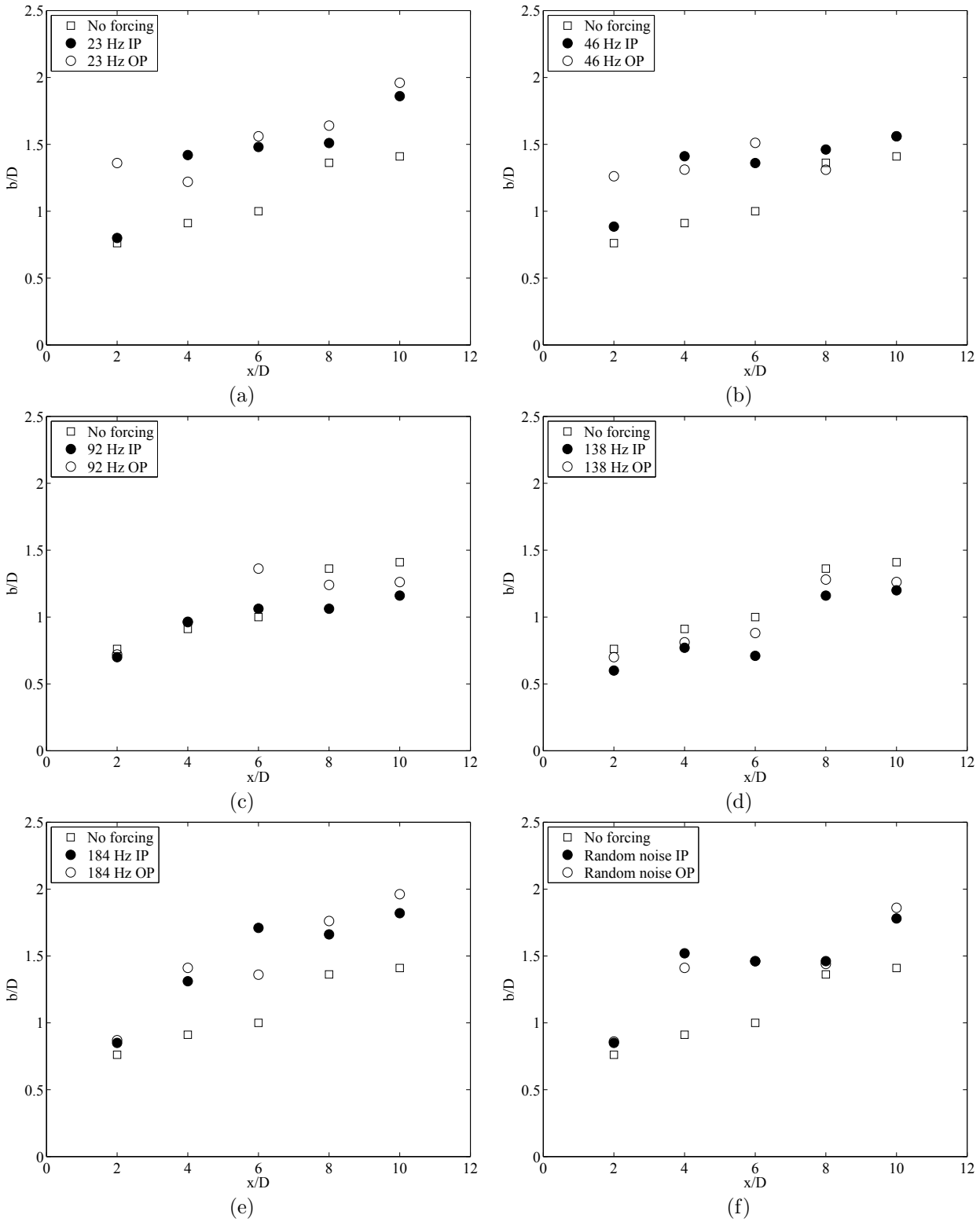

Figure 3.11: Variation of wake half-width (Re = 24,000)

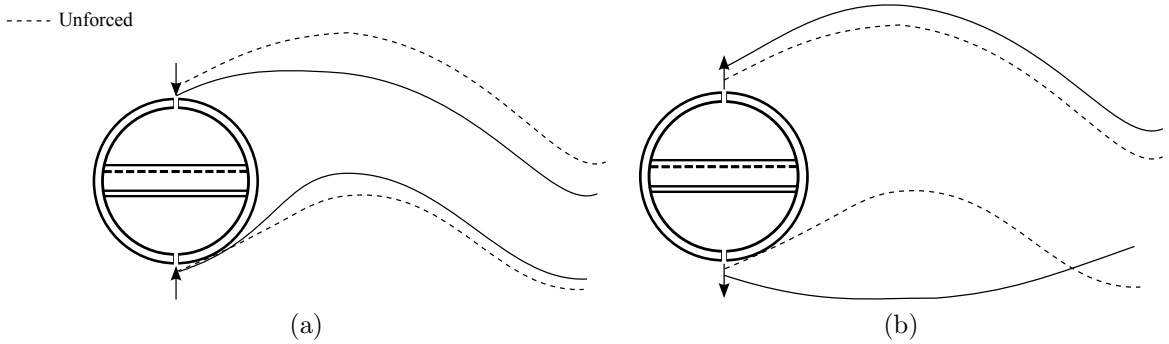

Figure 3.12: Cartoon of in-phase forcing effect

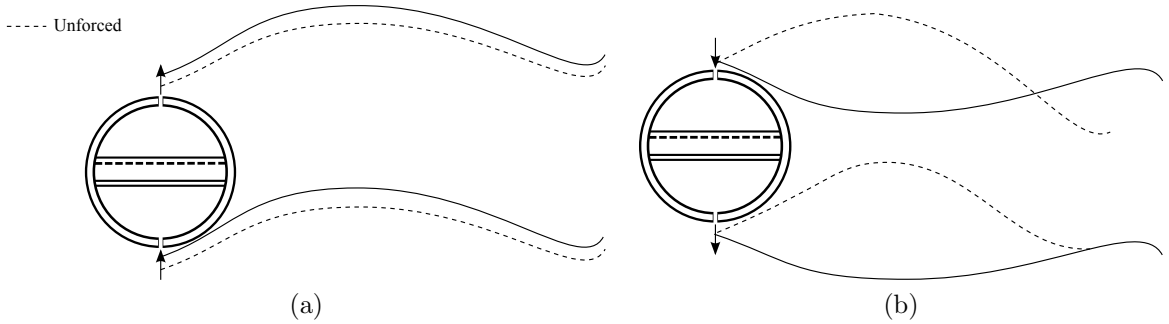

Figure 3.13: Cartoon of out-of-phase forcing effect

3.3 Time-averaged turbulent quantities

Particle image velocimetry (PIV), data was collected for each excitation frequency and driver mode from the near wake up to 10 diameters downstream. Through post processing, instantaneous velocity vector field data was produced for each of the 1155 image pairs recorded and later averaged. Additionally, snapshot proper orthogonal decomposition (POD) was implemented to extract the modal energy distributions of the flow. The velocity vector field at each location was combined and stitched together using a MATLAB program to form a continuous data range up to 10 diameters downstream in order to view the effects of forcing as the flow established over several diameters.

Flow statistics such as the turbulence intensity, Reynolds shear stress, turbulent kinetic energy, and vorticity were calculated for each case. The Reynolds shear stress is defined as $R_{ij} = \frac{\rho \overline{u_i' u_j'}}{U_\infty^2}$. Turbulent kinetic energy was calculated, using the mean of the turbulence

normal stress, $k = \frac{1}{2}\frac{(\overline{(u_1')^2}+\overline{(u_2')^2}+\overline{(u_3')^2})}{U_\infty^2}$. The TKE quantifies the mean kinetic energy associated with the eddies in the turbulent flow, making it easy to recognize the effectiveness of flow control. Large eddies carry large amounts of energy downstream, therefore a wake with a lower distribution of kinetic energy signifies an absence of large turbulent structures. Vorticity is defined as the curl of velocity and was an essential part in describing the effects of the applied forcing, $\zeta = \frac{\omega d}{U_\infty}$. By illustrating the vorticity of the flow, the vortices in the wake can be revealed on an average basis to aide in assessing the effectiveness of wake suppression.

PIV results are presented in Figures 3.14 through 3.83.

3.3.1 Time-averaged mean flow

The streamlines are presented in Figures 3.14 through 3.27. These figures represent the time-averaged trajectories of the seeded flow as it passed over the cylinder and provide a good indication of the effect of forcing. Figure 3.14 and 3.21 show the baseline, no forcing cases for Re = 12,000 and Re = 24,000 respectively. In each figure, two well defined foci can be seen in the center of the large, symmetric regions of circulation located in the near wake. A saddle point can also be seen where the streamlines intersect and mark the end of the near wake. The distance between the cylinder surface and end of the near wake is known as the formation length (L). As forcing was applied, it was apparent that there was a significant effect on the near wake and modification of the von Kármán vortices as evident from the deformation of the regions of circulation and reduction in formation length. In Figure 3.15b the top focal point was shifted out of the field of view and the near wake shrank significantly. The circulation region in Figure 3.18a is severely dampened and eludes to a successful suppression of the primary instability present in the no forcing case. The Re = 24,000 case showed similar patterns, but appeared to be less effective.

3.3.2 Turbulence intensity

Figure 3.28 shows a symmetric distribution of velocity fluctuations in the streamwise direction for the no forcing case at a Reynolds number of 12,000. On either side of the cylinder, the contour plot shows regions of large velocity fluctuations about 1.5 diameters downstream. This large velocity gradient appears near the location of the separating shear layers, indicating the formation of strong von Kármán vortices. Figure 3.29 compares the in-phase and out-of-phase excitation modes at 11.5 Hz, which is $\frac{1}{2}f_{s_0}$. It should be noted that the magnitude increased dramatically from the no forcing case, indicating a strengthened shear layer and subsequently, higher energy eddies. The in-phase excitation portrayed lower velocity fluctuations than the out-of-phase case indicating a more effective disruption of the vortex formation. When the forcing frequency was equal to the natural shedding frequency of the cylinder, $f_e = f_{s_0}$, the out-of-phase case produced smaller velocity fluctuations relative to in-phase. At $2f_{s_0}$, a significant decrease in magnitude of the fluctuating velocities was seen, which was in concordance with the power spectral density analysis, showing wake suppression. A lower degree of velocity fluctuations was seen in the out-of-phase driver mode when compared with the in-phase mode. This trend continued until the random noise case, where the in-phase mode saw a lower magnitude of fluctuations.

Generally, for the higher Reynolds number cases, the in-phase forcing mode had lower velocity fluctuations relative to out-of-phase shown in Figures 3.35 through 3.41. Note that the magnitude increased compared to the lower Reynolds number case. This was to be expected due to the larger free stream velocities associated with a higher Reynolds number. Also in the Re=24,000 cases at forcing frequencies of $\frac{1}{2}f_{s_0}$ and f_{s_0}, a large increase in the magnitude of velocity fluctuations due to the apparent strengthening of vortex formation was observed. It was also apparent here due to the lower Turbulence intensities, that as the excitation frequency increased, the formation of the von Kármán vortices were disrupted by the two dimensional disturbances introduced.

3.3.3 Reynolds shear stress

The distribution of Reynolds shear stress in the wake of the circular cylinder is illustrated in Figures 3.42 through 3.55. Figure 3.42 displays the Reynolds stress for the no forcing case. The pockets of oppositely signed Reynolds stress were relatively high in magnitude and symmetric, which corresponds to the large velocity gradients seen in the separating shear layers in Figure 3.42. Reynolds stress has a direct relationship with the streamwise fluctuating velocities and therefore, similar increases in magnitude were seen with periodic forcing frequencies of $\frac{1}{2}f_{s_0}$ and f_{s_0}. For $f_e \geq 2f_{s_0}$ at both Reynolds numbers, there was a decrease in Reynolds stress along the shear layer region in the cylinder wake. According to Williamson [6], this behavior is indicative of an elongation of the near wake, which in turn, leads to the conclusion that a successful attenuation of the primary instability occurred. When forcing was introduced, an asymmetry developed in the near wake due to the disruption of the shear layers on the top and bottom of the cylinder. Naturally, the unforced cylinder had a pure sinusoidal wake that, when averaged, formed a symmetric contour as seen in Figures 3.42 and 3.49. The in-phase case created an asymmetry in the flow and was reflected in the contour plots as having a larger magnitude on either the top or bottom of the cylinder. According to the wake power spectra, the vortex shedding frequency appeared to lock on to the out-of-phase forcing mode creating less of an asymmetry, but still successfully disrupting the shear layers and decreasing the Reynolds stress. On average, the in-phase forcing mode was more effective at decreasing the Reynolds stress in the near wake region for both the Re=12,000 and Re=24,000 cases.

3.3.4 Turbulent kinetic energy

As discussed earlier, the successful suppression of the von Kármán vortex formation is accomplished by breaking up the forming vortices into smaller eddies as they develop near the surface of the cylinder. Smaller eddies inherently contain less energy than larger eddies, therefore the frequencies that successfully suppress the formation of Kármán vortices will

show a decrease in kinetic energy throughout the wake. Figures 3.56 through 3.69 show the distribution of the time-averaged turbulent kinetic energy in. Figure 3.56 shows a large concentration of kinetic energy in the near wake at about $\frac{x}{D} = 1.5$. As the vortex was shed downstream the kinetic energy decreased due to dissipation. The kinetic energy distribution seen in Figures 3.57 and 3.58 was greater than that of the no forcing case due to the higher magnitude of turbulence intensity as discussed earlier. So, as u' decreased with higher forcing frequencies, there was an increase in the uniformity of the flow velocity illustrated as a decrease in turbulent kinetic energy. For Re=12,000, the sub-harmonic and natural forcing frequencies had a greater benefit from the forcing mode being in-phase, where as the remaining forcing frequencies showed the out-of-phase mode as being more effective at decreasing the kinetic energy. However, the in-phase random noise case was seen to decrease the kinetic energy more effectively. For Re=24,000, the in-phase driver mode produced a larger decrease in Turbulent kinetic energy distribution.

3.3.5 Vorticity

Contour plots of time-averaged vorticity are given in Figures 3.70 through 3.76 for Re = 12,000 and Figures 3.77 through 3.83 for Re = 24,000. The plots display oppositely signed vorticity spanning the wake of the cylinder up to 10 diameters downstream. High magnitudes of clockwise vorticity are colored blue and counter-clockwise are colored red. The vorticity was seen to be of the greatest magnitude along the shear layers aft of the cylinder and decreased as the vortices travelled downstream in Figure 3.70. The von Kármán vortex formation is easily discernible from the regions of vorticity revealed in the contour plot. The out-of-phase forcing at frequencies of $\frac{1}{2}f_{s_0}$ and f_{s_0}, for both Reynolds numbers, show a higher concentration of vorticity and an increase in the wake width as illustrated in Figures 3.71, 3.72, 3.78,and 3.79. This indicated an increase in energy and vortex formation strength, which supports the previous observations. As the forcing frequency was increased to $2f_{s_0}$

and above, it was observed that the wake narrowed and a decrease in the vorticity indicated a diffusion of vorticity in the shear layer.

3.3.6 POD modal energy distribution

Proper orthogonal decomposition is very useful in breaking down complex dynamical systems into low-dimensional flow fields, which is useful in characterizing the coherent flow structures of interest [45]. The energy distribution across the POD modes was found to decay exponentially and for modes above five, the energy was very small relative to mode 1. Therefore, the first five proper orthogonal modes were chosen to aide in illustrating the effect each periodic forcing frequency had on the overall flow. Figures 3.84 and 3.85 show the energy distribution at each downstream location for the first five modes.

In the baseline case, Figure 3.84 shows mode-1 as the structure with the highest energy at about 35% and decreasing with downstream location. Modes 2 and 3 are shown to increase slightly from x/D = 2 to x/D = 4. This occurred because the structures associated with these modes in the no forcing case were stronger and more developed as they progressed downstream. It was evident for forcing of $f_e = \frac{1}{2} f_{s_0}$ and $f_e = f_{s_0}$, for both Reynolds numbers, that the overall energy distribution was associated with a greater magnitude than that of the no forcing case for the out-of-phase driver mode. This indicated that the out-of-phase mode added energy to the developing instabilities of the flow and increased the strength of the von Kármán vortices. In general, the Re = 12,000 and Re = 24,000 cases exhibited a behavior in which the first two modes in the out-of-phase case were consistently associated with a higher energy distribution than the in-phase mode. However, modes 3 through 5 had higher energies in the in-phase mode compared to out-of-phase. At forcing frequencies greater than $f_e = f_{s_0}$, the modal energy was less than the no forcing case, indicating a successful decrease in vortex strength. It was also noted that modes 3 through 5 for all forcing frequencies contained, relatively, the same energy magnitude as the no forcing case,

meaning the periodic forcing had less of an effect on lower energy turbulent structures in the wake.

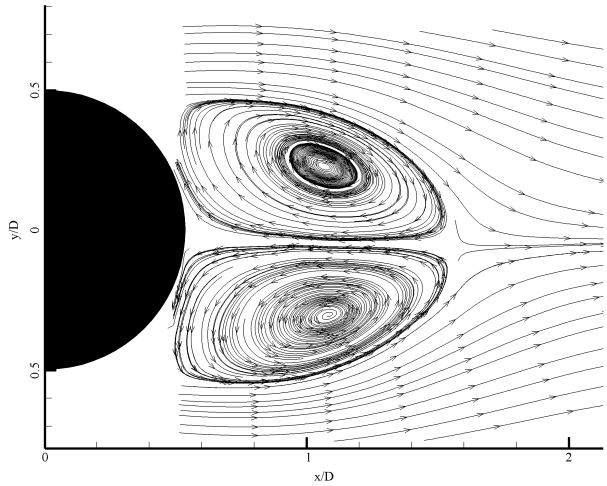

Figure 3.14: Streamline topology (Re = 12,000, No forcing)

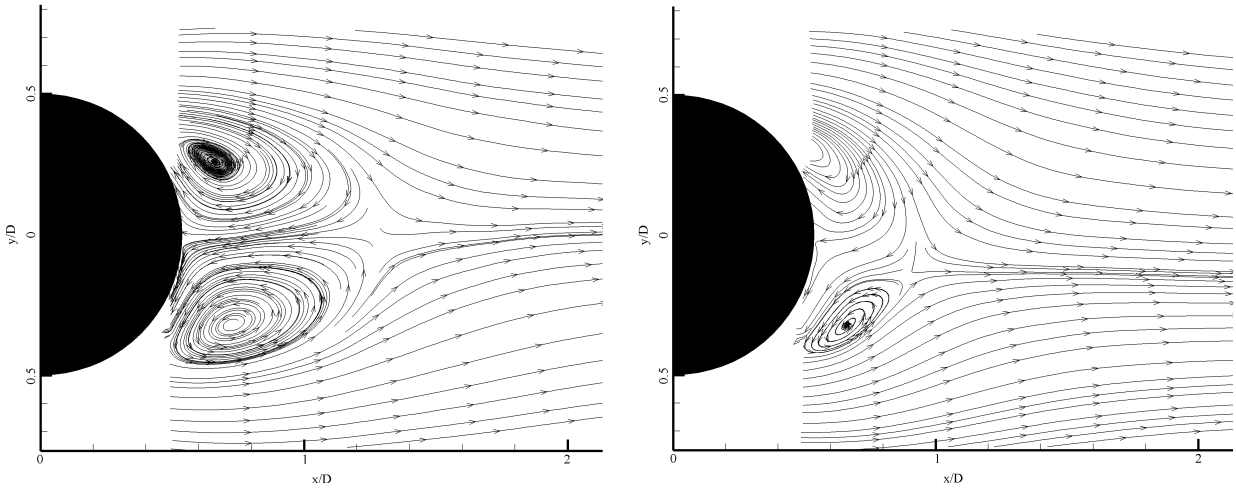

(a) In-phase (b) Out-of-phase

Figure 3.15: Streamline topology (Re = 12,000, f_e = 11.5 Hz)

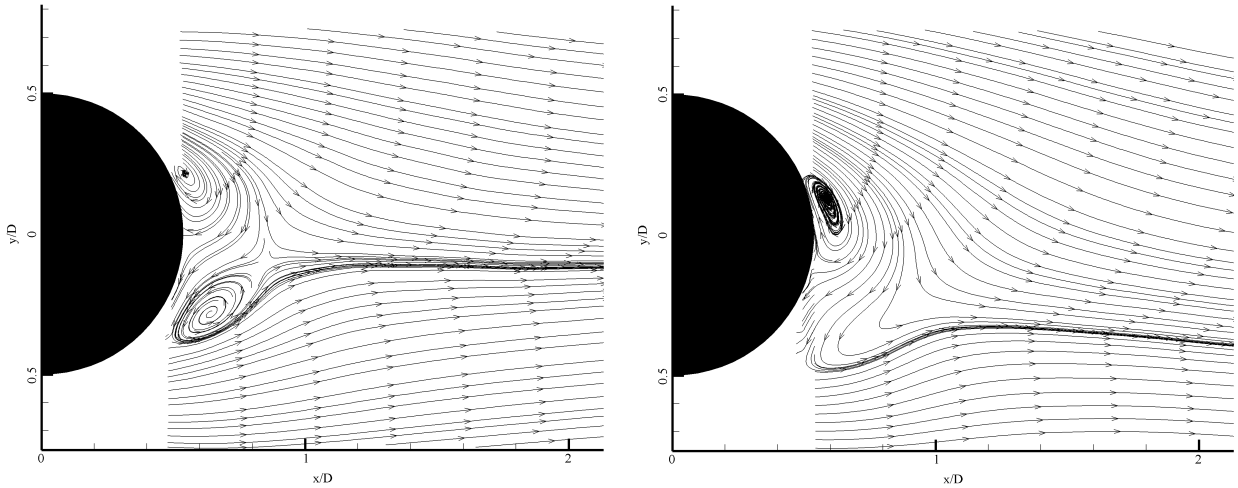

(a) In-phase (b) Out-of-phase

Figure 3.16: Streamline topology (Re = 12,000, f_e = 23 Hz)

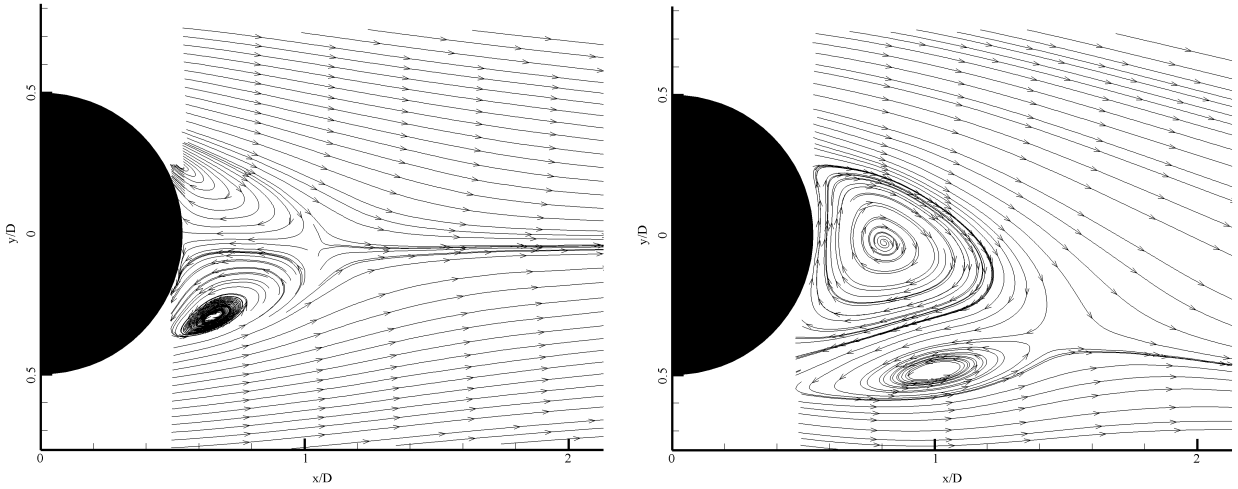

(a) In-phase (b) Out-of-phase

Figure 3.17: Streamline topology (Re = 12,000, f_e = 46 Hz)

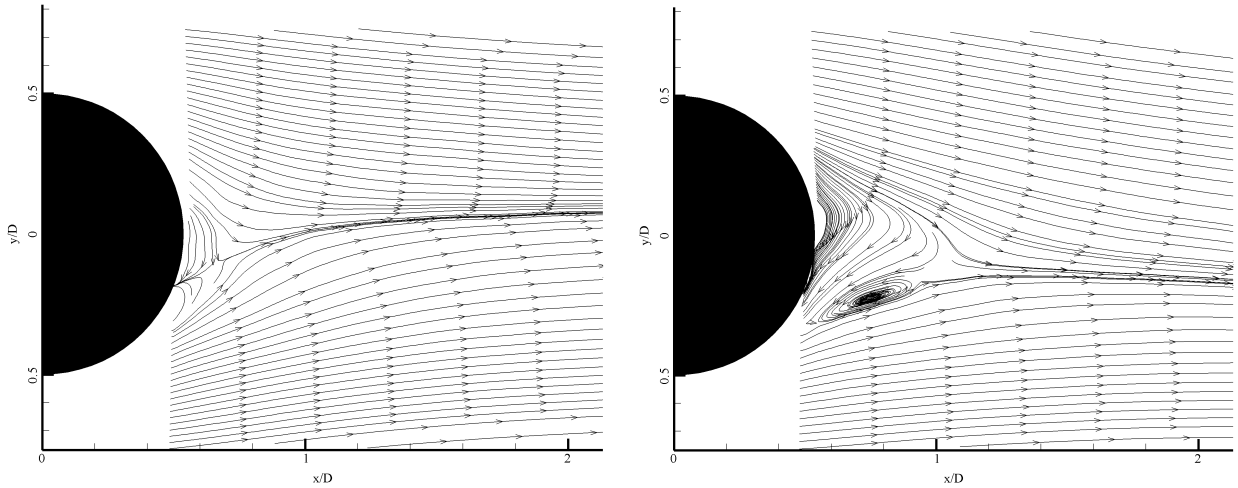

(a) In-phase (b) Out-of-phase

Figure 3.18: Streamline topology (Re = 12,000, f_e = 69 Hz)

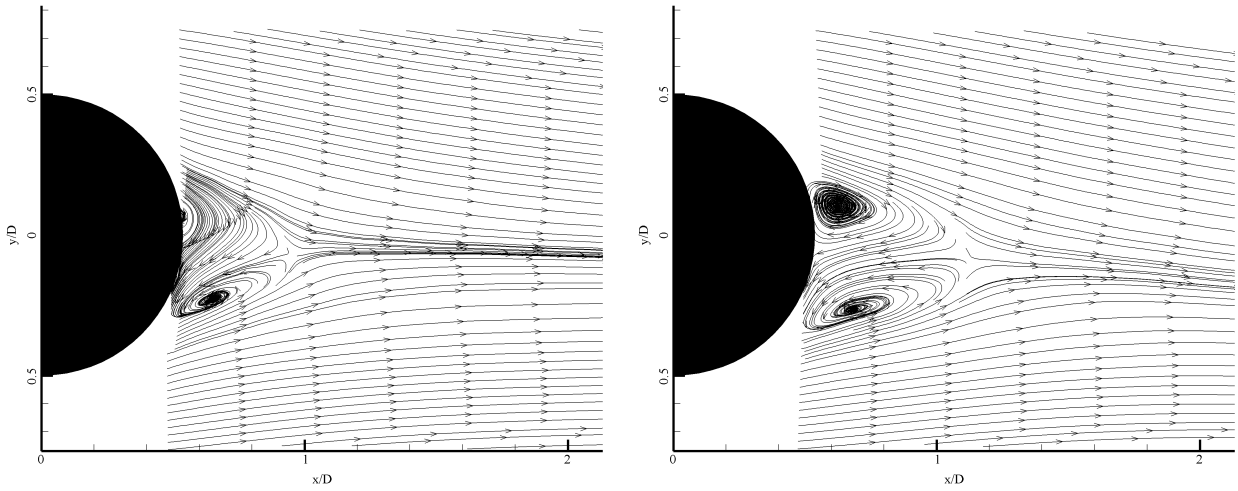

(a) In-phase (b) Out-of-phase

Figure 3.19: Streamline topology (Re = 12,000, f_e = 92 Hz)

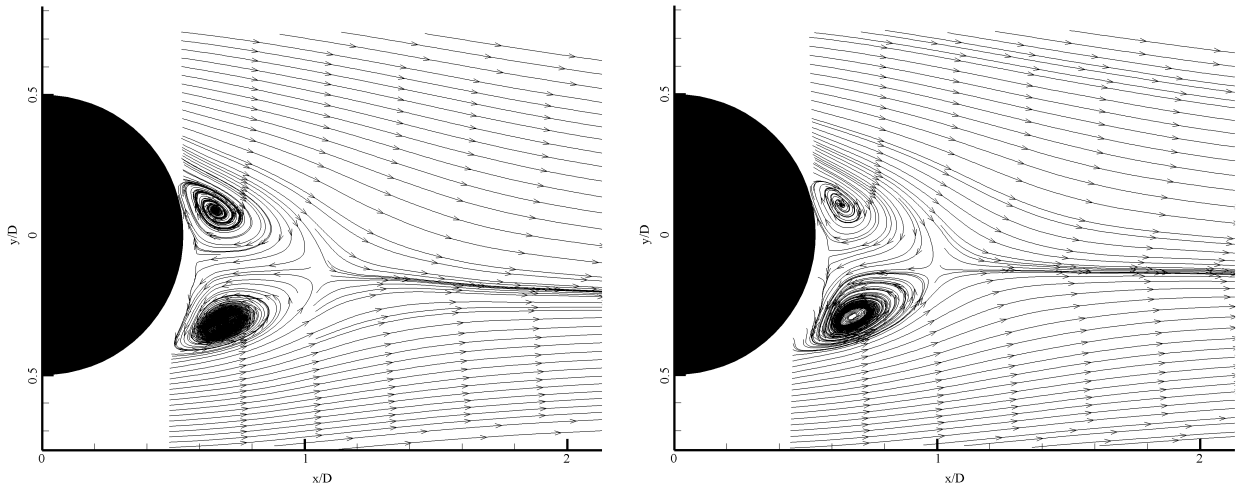

(a) In-phase (b) Out-of-phase

Figure 3.20: Streamline topology (Re = 12,000, f_e = Random noise)

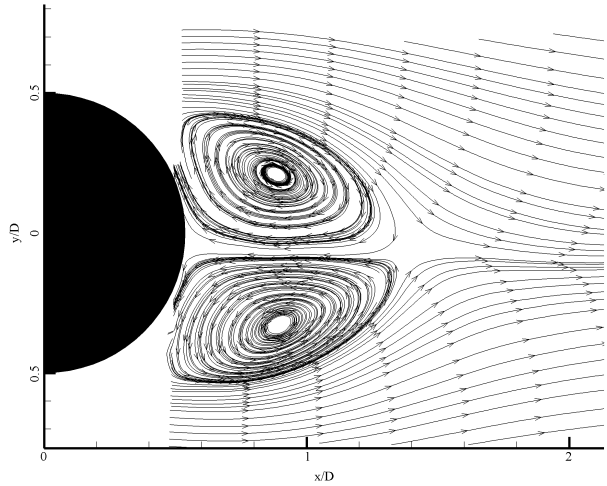

Figure 3.21: Streamline topology (Re = 24,000, No forcing)

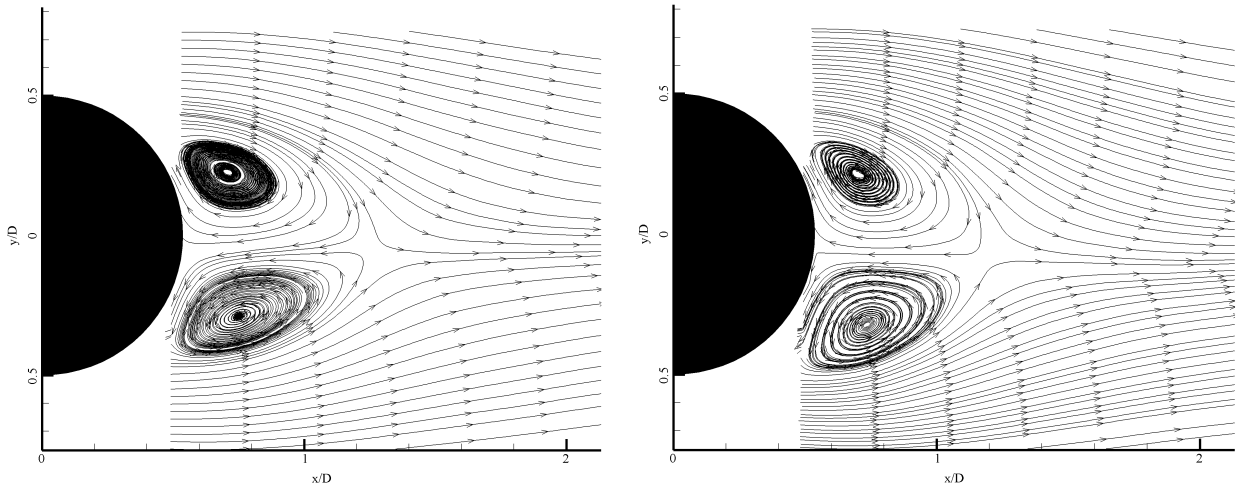

(a) In-phase (b) Out-of-phase

Figure 3.22: Streamline topology (Re = 24,000, f_e = 23 Hz)

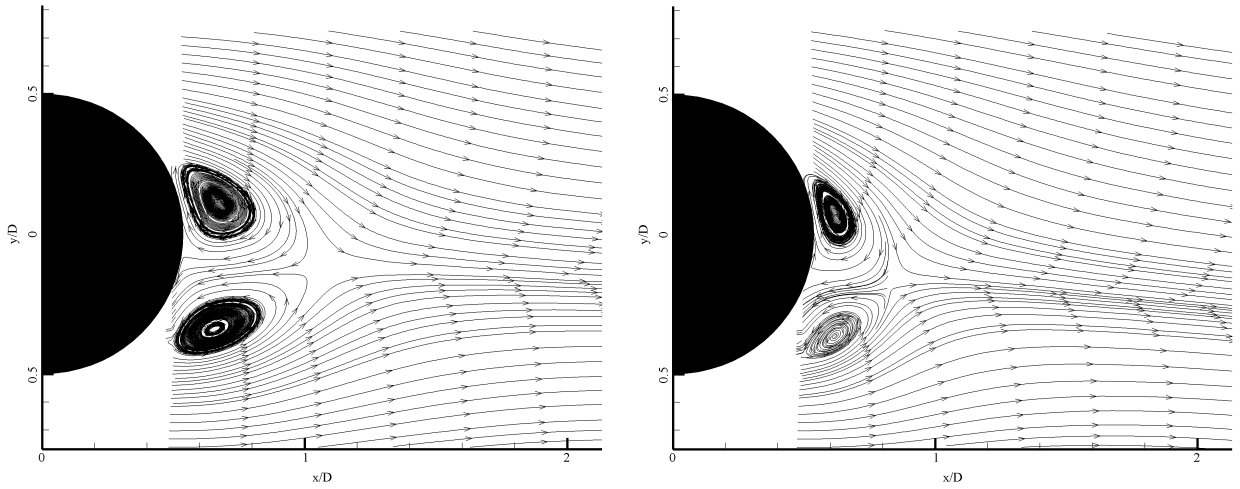

(a) In-phase (b) Out-of-phase

Figure 3.23: Streamline topology (Re = 24,000, f_e = 46 Hz)

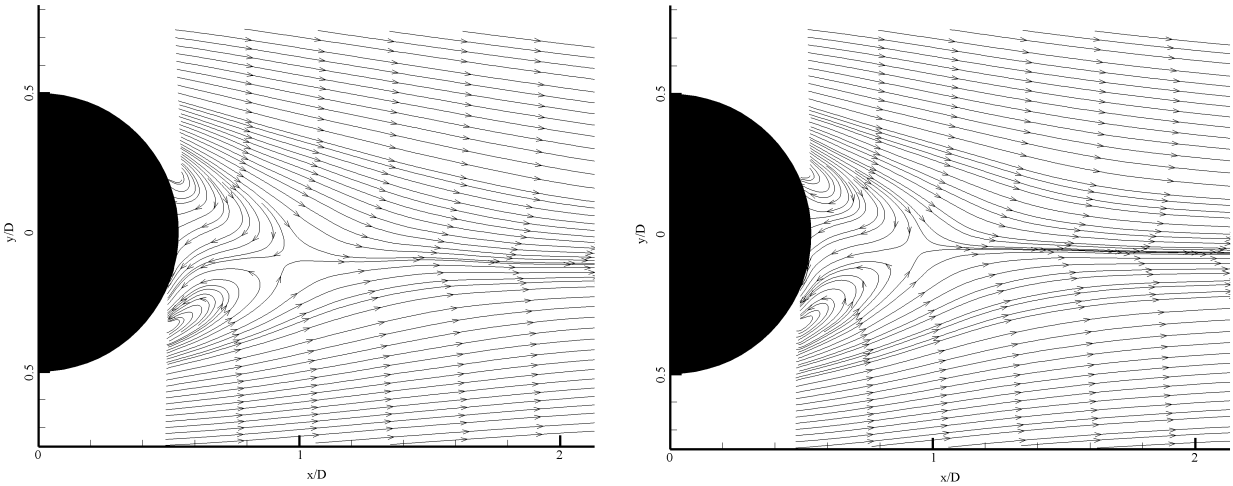

(a) In-phase (b) Out-of-phase

Figure 3.24: Streamline topology (Re = 24,000, f_e = 92 Hz)

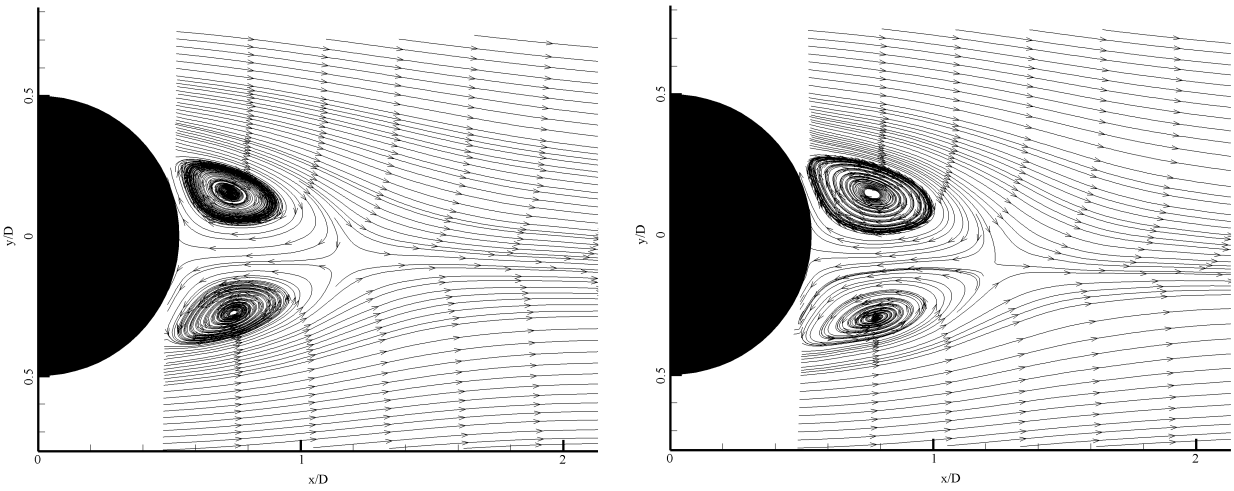

(a) In-phase (b) Out-of-phase

Figure 3.25: Streamline topology (Re = 24,000, f_e = 138 Hz)

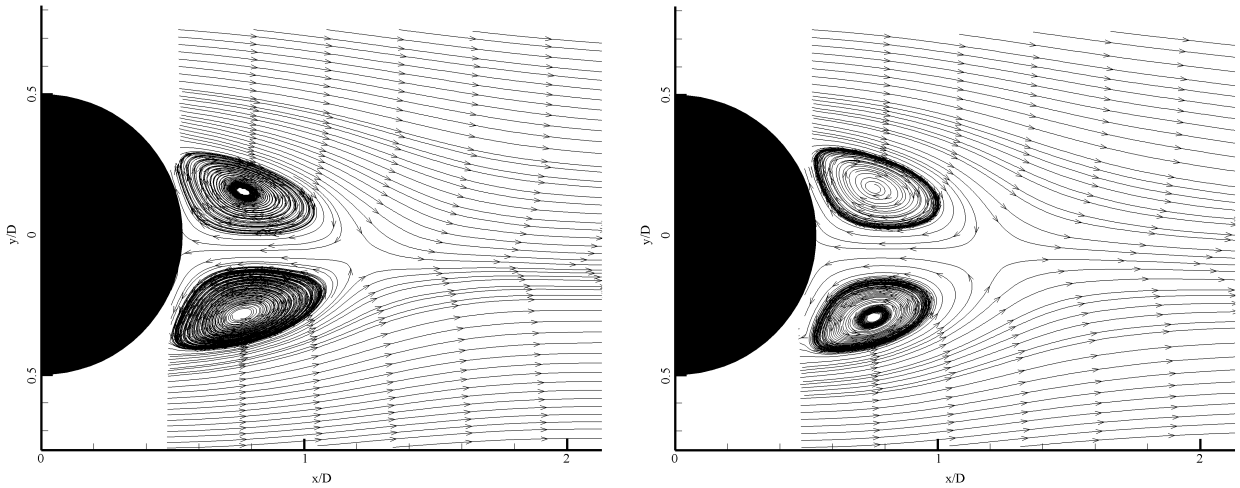

(a) In-phase (b) Out-of-phase

Figure 3.26: Streamline topology (Re = 24,000, f_e = 184 Hz)

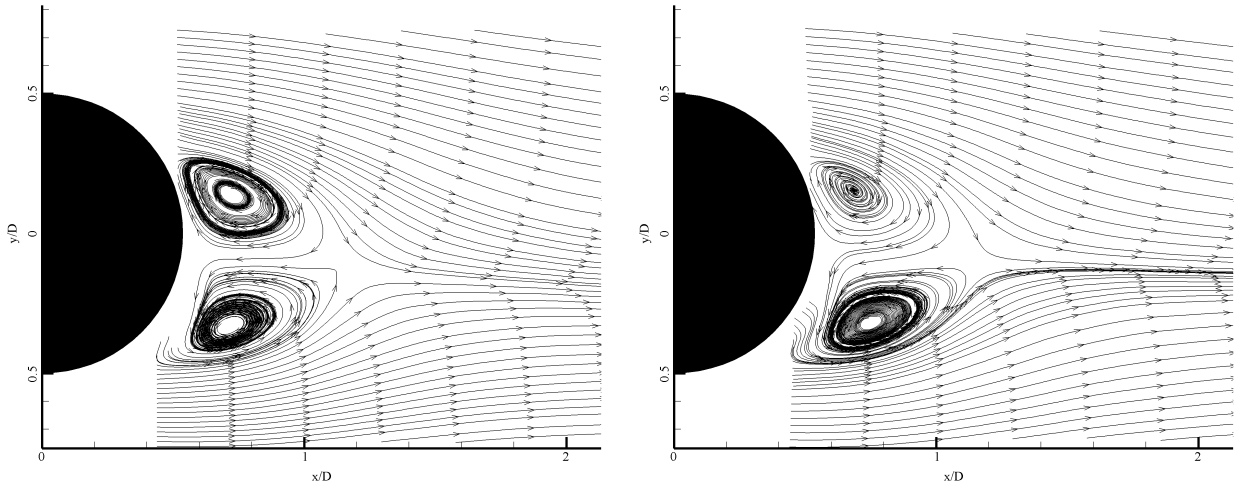

(a) In-phase (b) Out-of-phase

Figure 3.27: Streamline topology (Re = 24,000, f_e = Random noise)

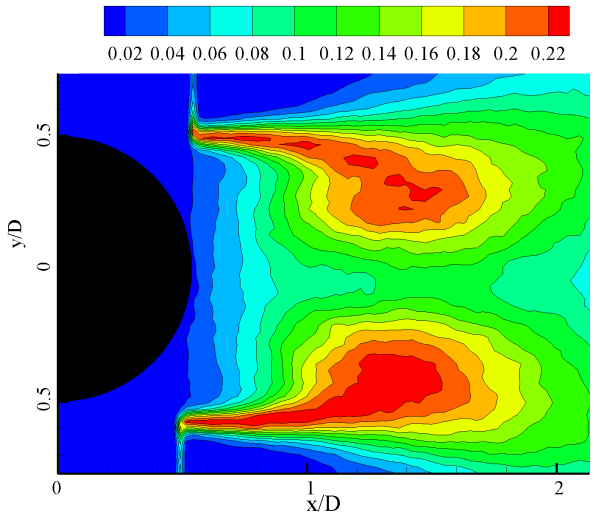

Figure 3.28: Turbulence intensity contour (Re = 12,000, No forcing)

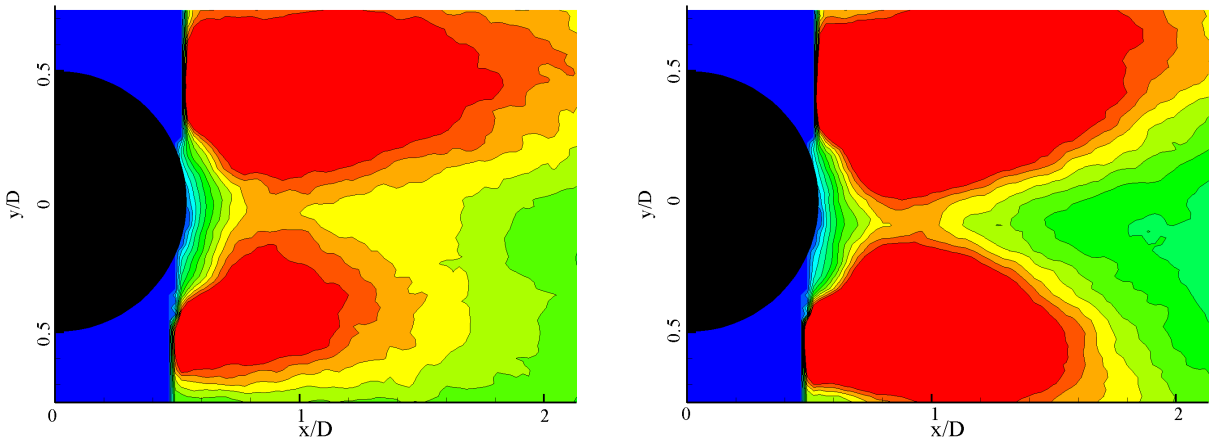

(a) In-phase

(b) Out-of-phase

Figure 3.29: Turbulence intensity contour (Re = 12,000, f_e = 11.5 Hz)

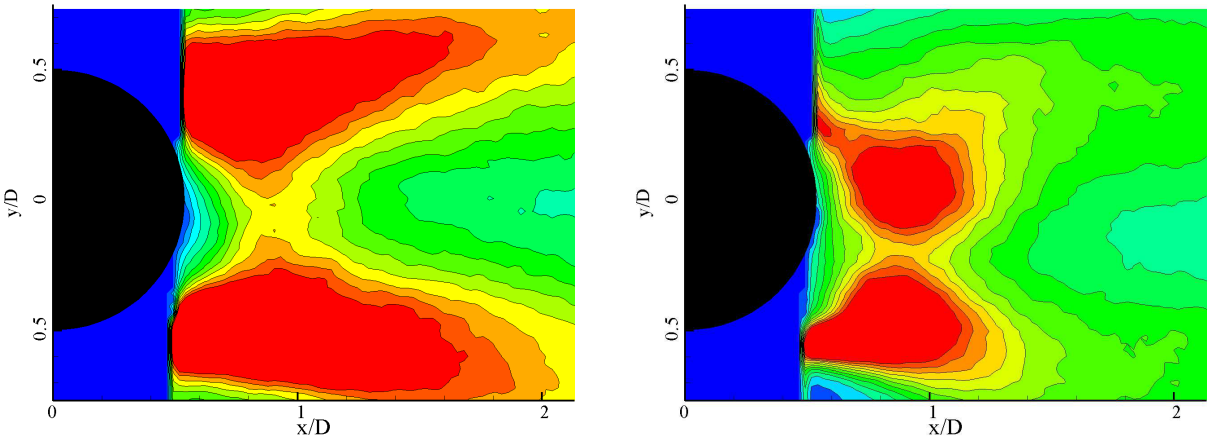

(a) In-phase (b) Out-of-phase

Figure 3.30: Turbulence intensity contour (Re = 12,000, f_e = 23 Hz)

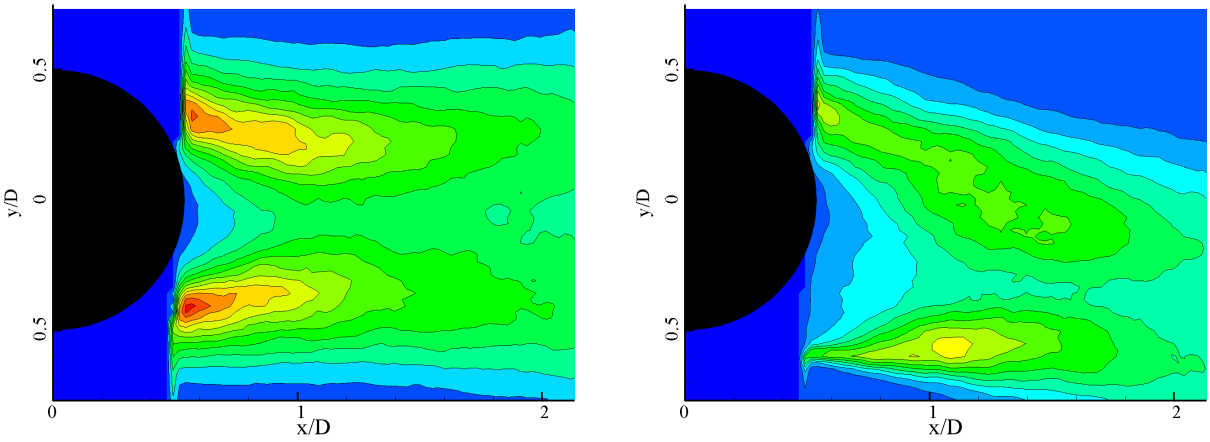

(a) In-phase (b) Out-of-phase

Figure 3.31: Turbulence intensity contour (Re = 12,000, f_e = 46 Hz)

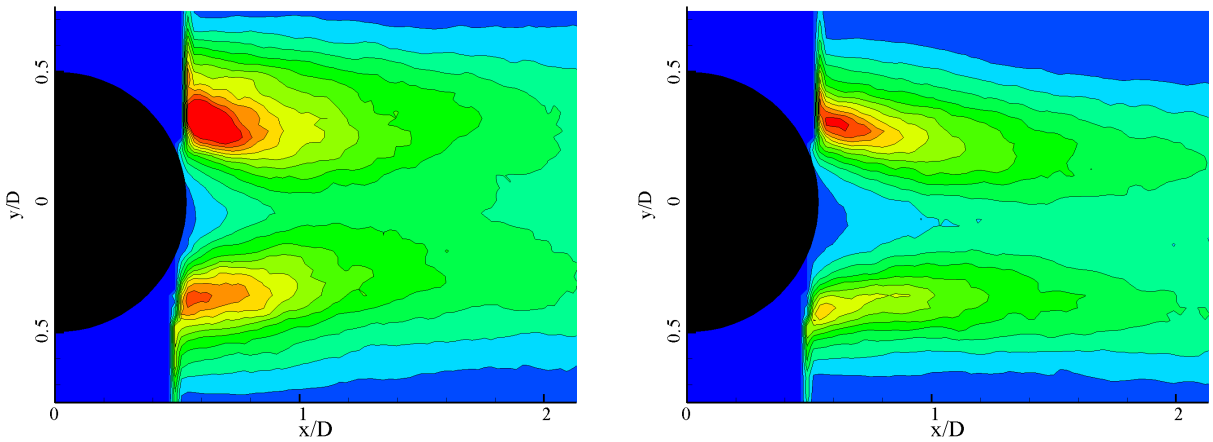

(a) In-phase (b) Out-of-phase

Figure 3.32: Turbulence intensity contour (Re = 12,000, f_e = 69 Hz)

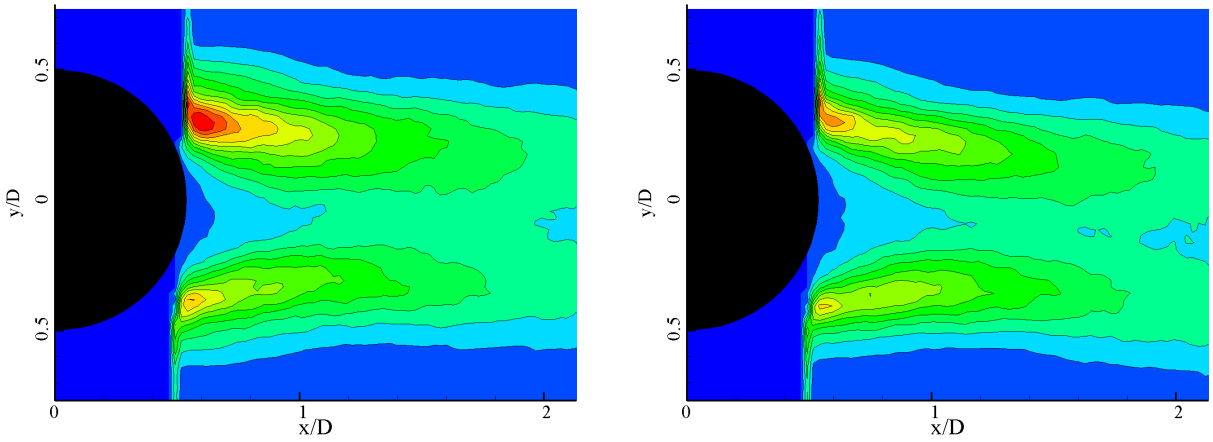

(a) In-phase (b) Out-of-phase

Figure 3.33: Turbulence intensity contour (Re = 12,000, f_e = 92 Hz)

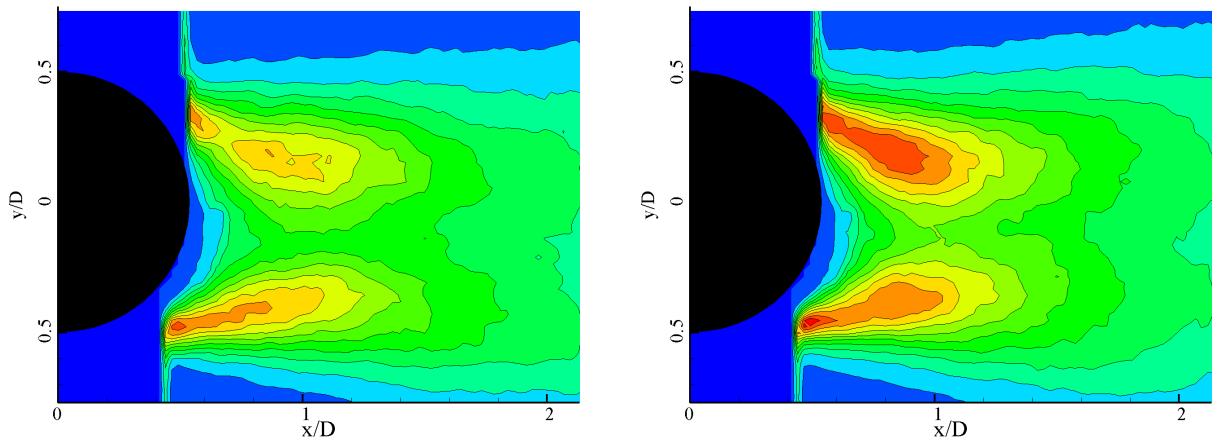

(a) In-phase (b) Out-of-phase

Figure 3.34: Turbulence intensity contour (Re = 12,000, f_e = Random noise)

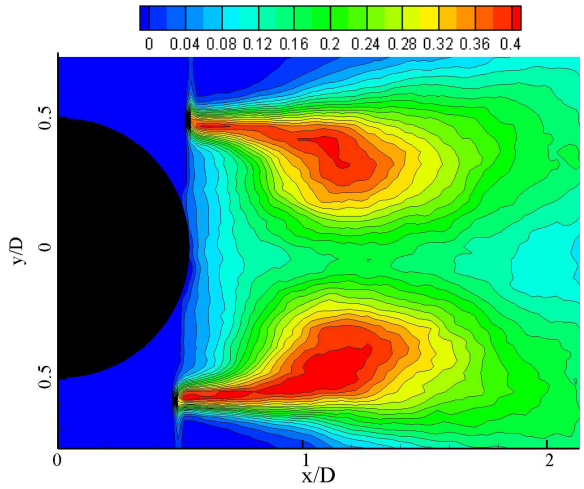

Figure 3.35: Turbulence intensity contour (Re = 24,000, No forcing)

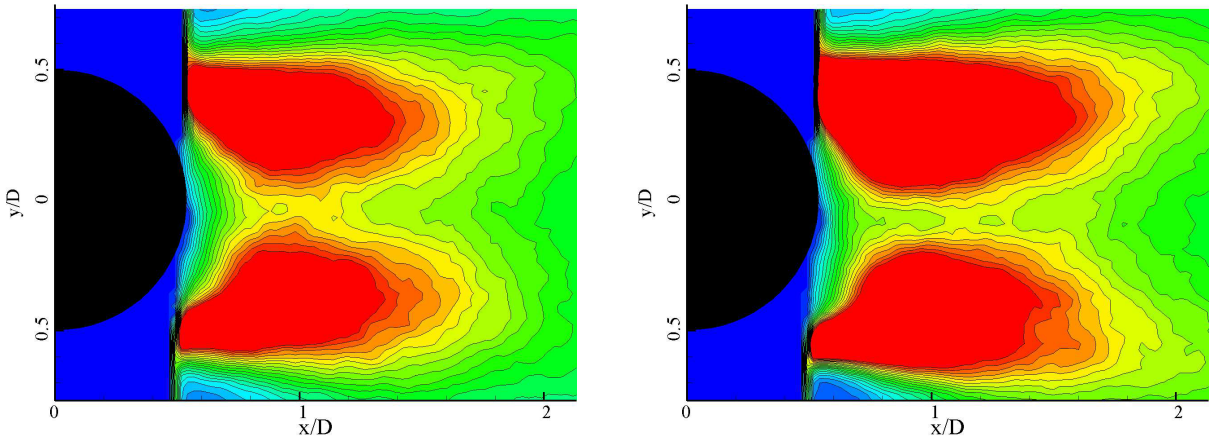

(a) In-phase (b) Out-of-phase

Figure 3.36: Turbulence intensity contour (Re = 24,000, f_e = 23 Hz)

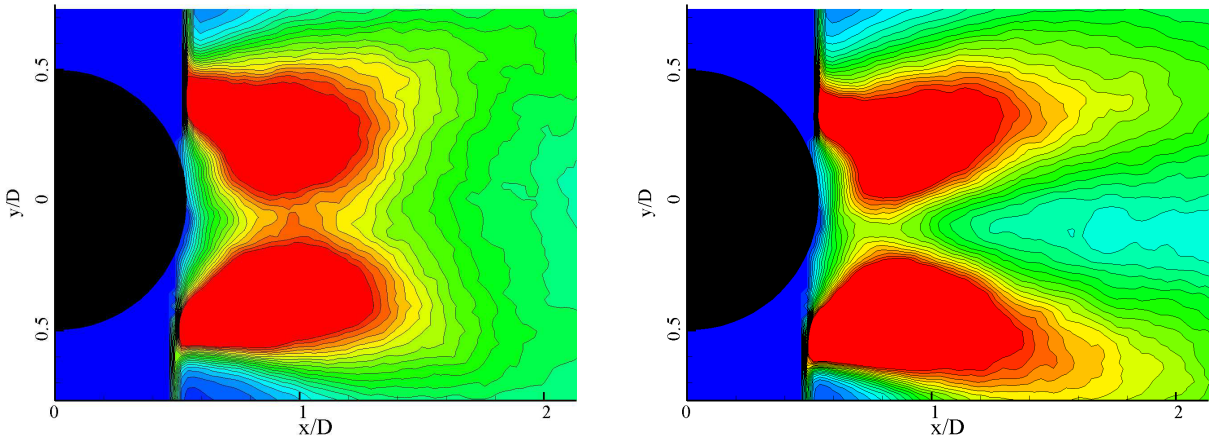

(a) In-phase (b) Out-of-phase

Figure 3.37: Turbulence intensity contour (Re = 24,000, f_e = 46 Hz)

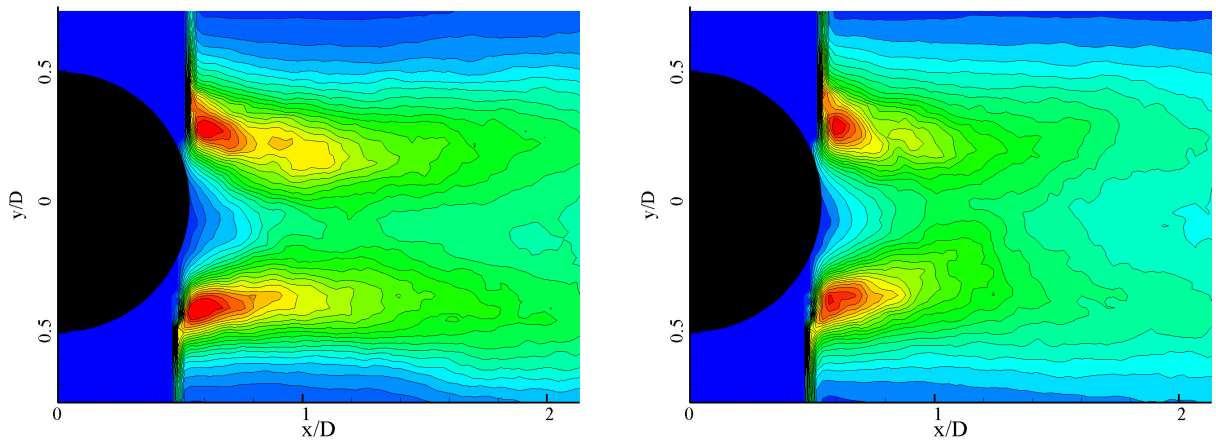

(a) In-phase (b) Out-of-phase

Figure 3.38: Turbulence intensity contour (Re = 24,000, f_e = 92 Hz)

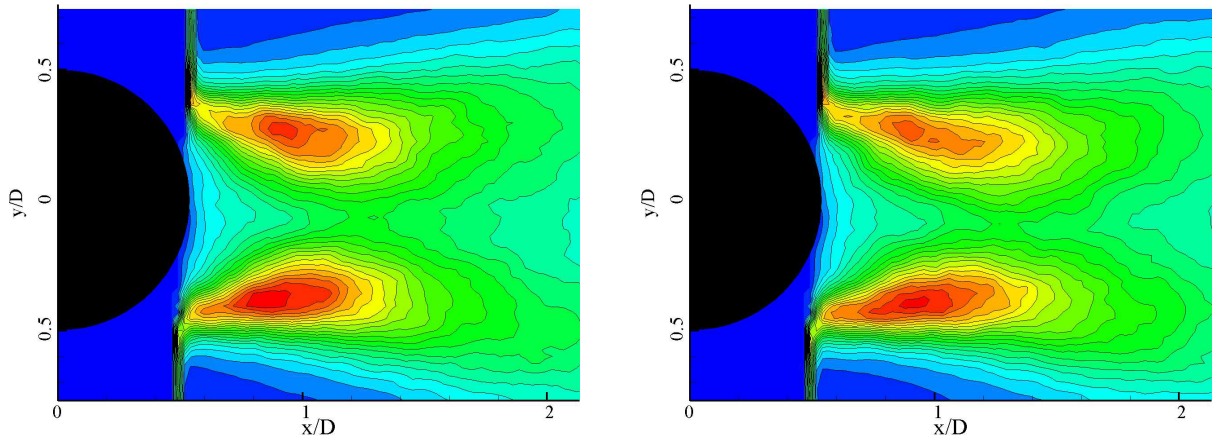

(a) In-phase (b) Out-of-phase

Figure 3.39: Turbulence intensity contour (Re = 24,000, f_e = 138 Hz)

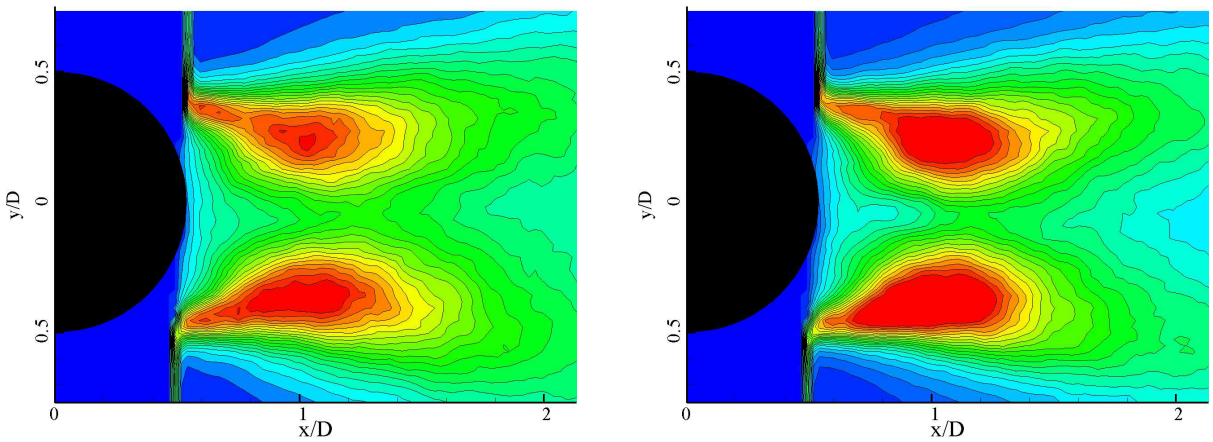

(a) In-phase (b) Out-of-phase

Figure 3.40: Turbulence intensity contour (Re = 24,000, f_e = 184 Hz)

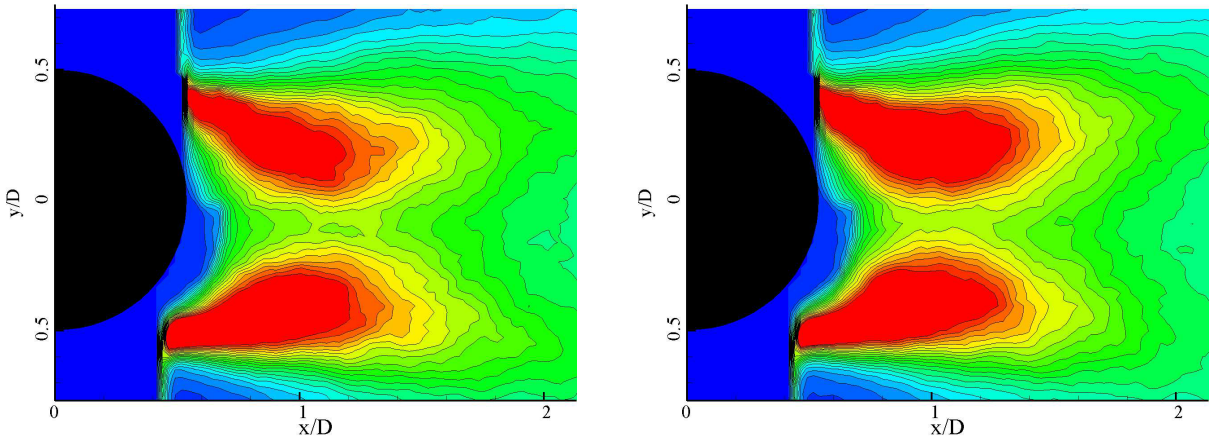

(a) In-phase (b) Out-of-phase

Figure 3.41: Turbulence intensity contour (Re = 24,000, f_e = Random noise)

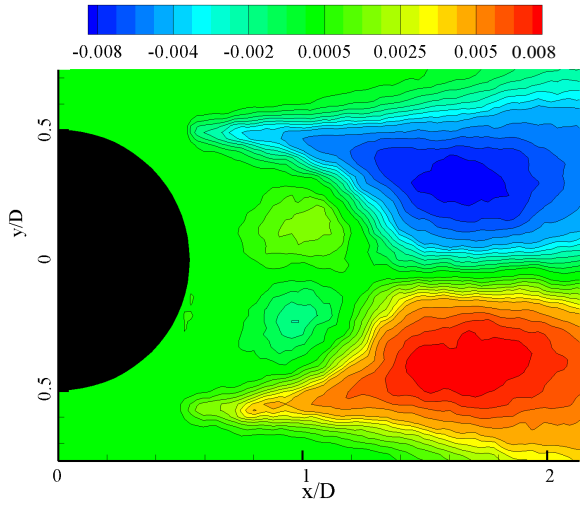

Figure 3.42: Reynolds shear stress contour (Re = 12,000, No forcing)

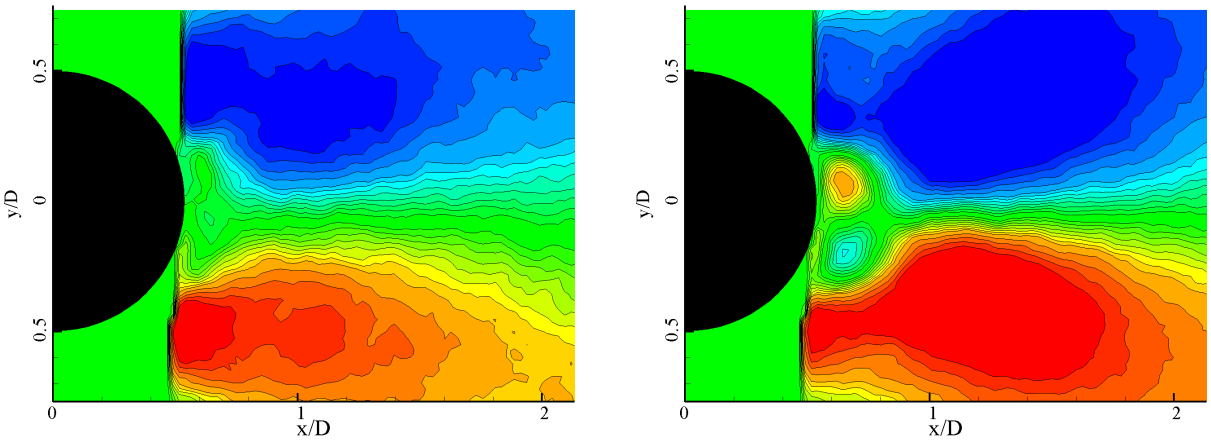

(a) In-phase

(b) Out-of-phase

Figure 3.43: Reynolds shear stress contour (Re = 12,000, f_e = 11.5 Hz)

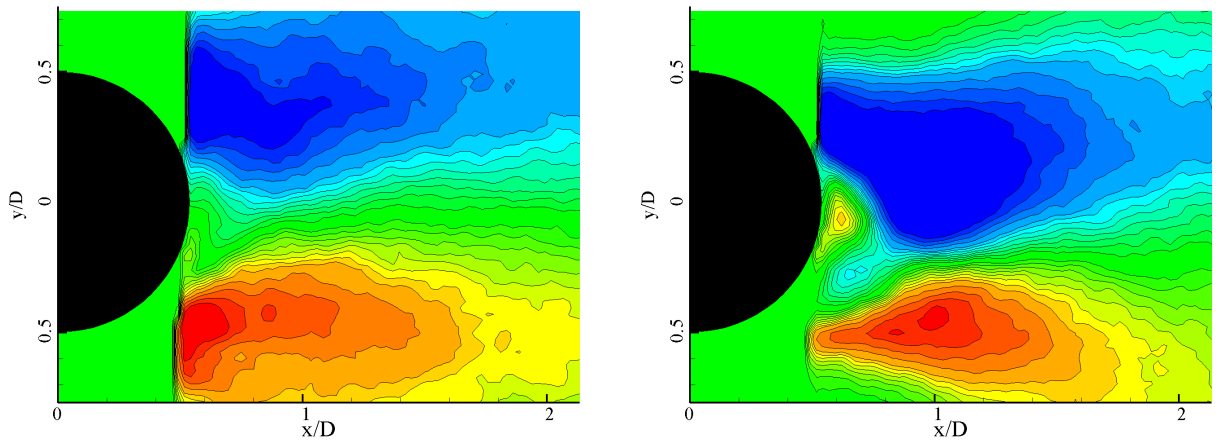

(a) In-phase (b) Out-of-phase

Figure 3.44: Reynolds shear stress contour (Re = 12,000, f_e = 23 Hz)

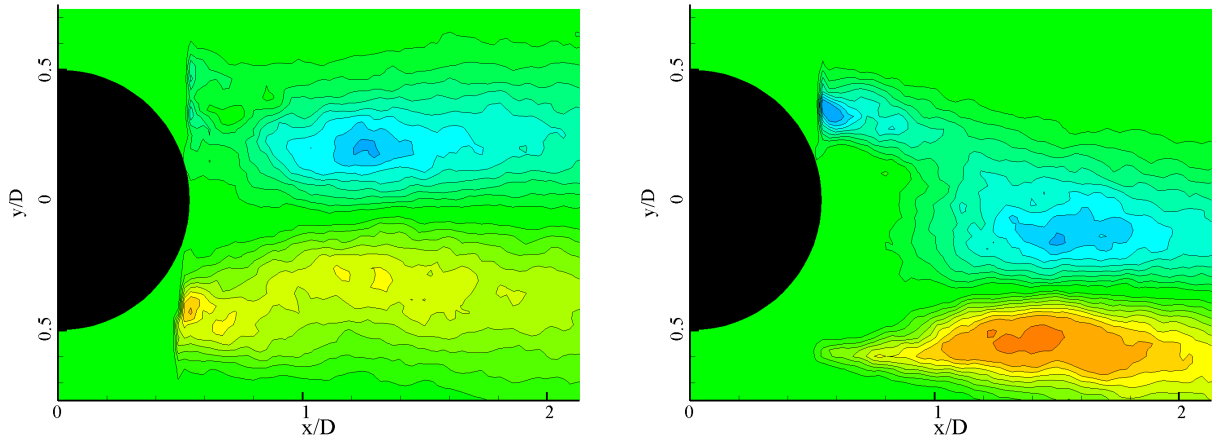

(a) In-phase (b) Out-of-phase

Figure 3.45: Reynolds shear stress contour (Re = 12,000, f_e = 46 Hz)

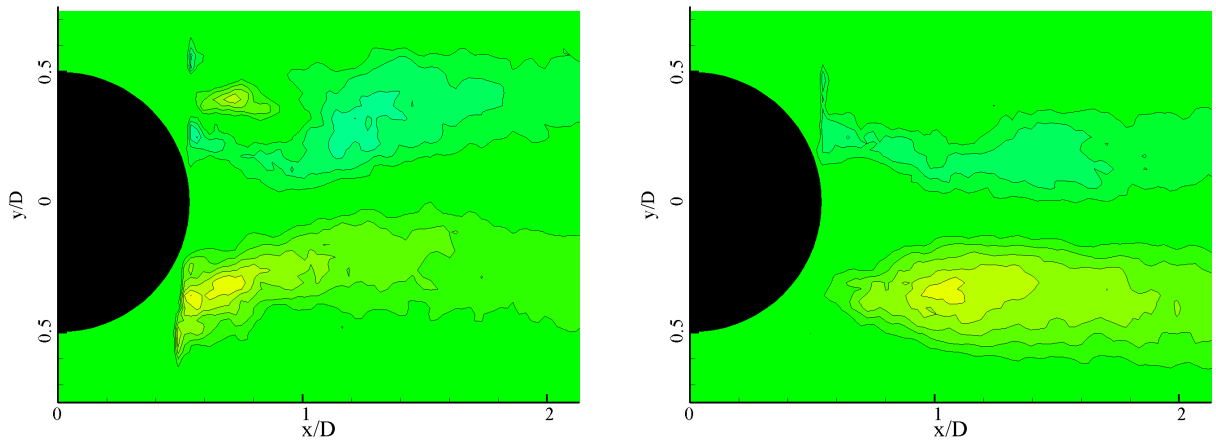

(a) In-phase (b) Out-of-phase

Figure 3.46: Reynolds shear stress contour (Re = 12,000, f_e = 69 Hz)

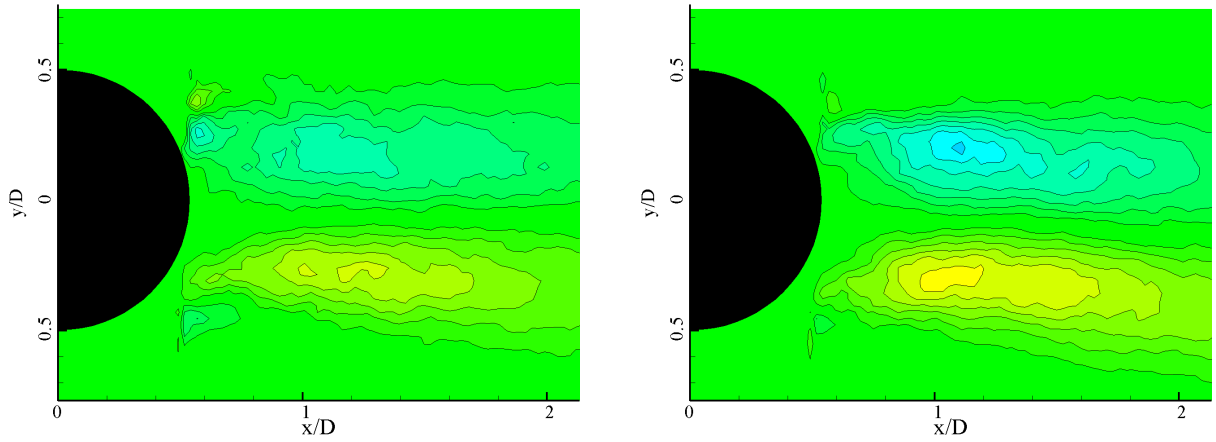

(a) In-phase (b) Out-of-phase

Figure 3.47: Reynolds shear stress contour (Re = 12,000, f_e = 92 Hz)

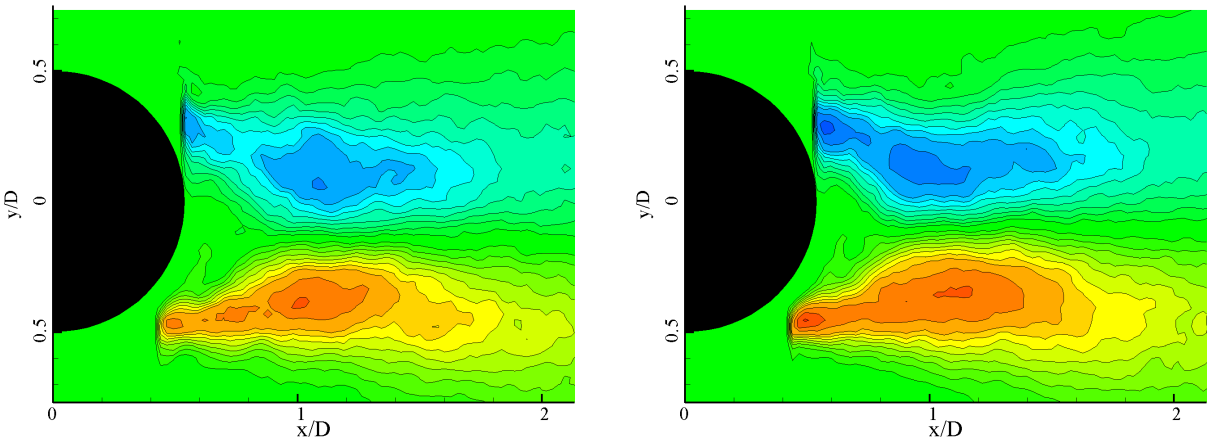

(a) In-phase (b) Out-of-phase

Figure 3.48: Reynolds shear stress contour (Re = 12,000, f_e = Random noise)

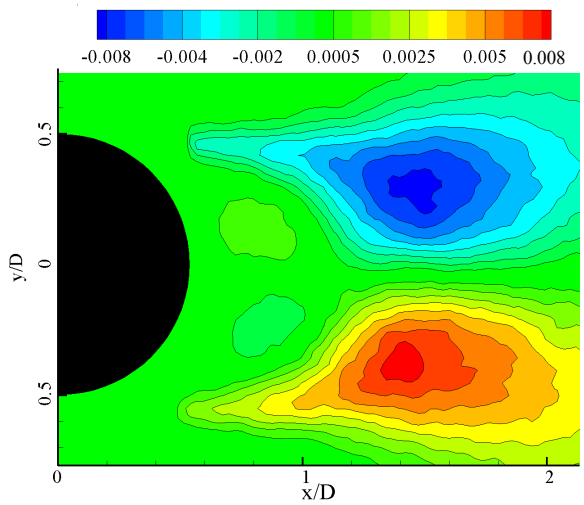

Figure 3.49: Reynolds shear stress contour (Re = 24,000, No forcing)

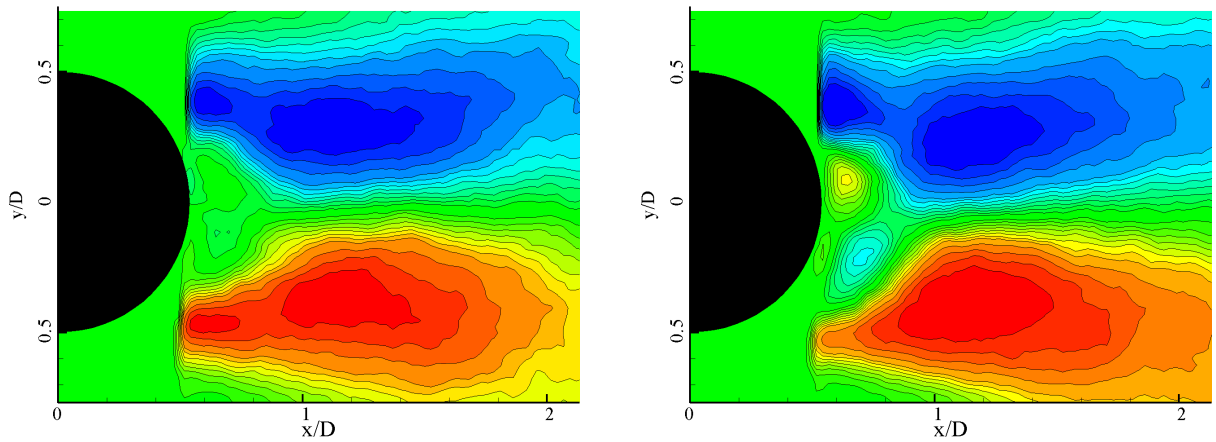

(a) In-phase (b) Out-of-phase

Figure 3.50: Reynolds shear stress contour (Re = 24,000, f_e = 23 Hz)

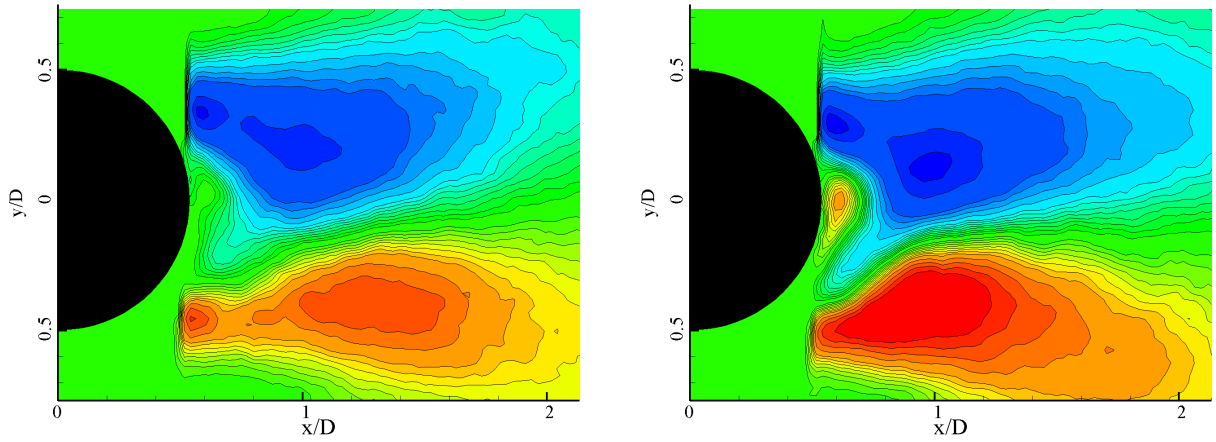

(a) In-phase (b) Out-of-phase

Figure 3.51: Reynolds shear stress contour (Re = 24,000, f_e = 46 Hz)

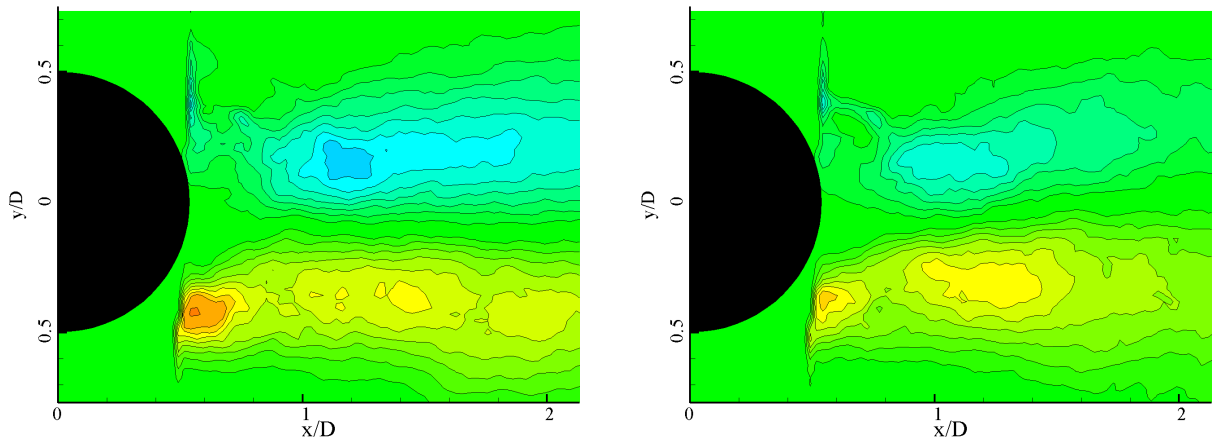

(a) In-phase (b) Out-of-phase

Figure 3.52: Reynolds shear stress contour (Re = 24,000, f_e = 92 Hz)

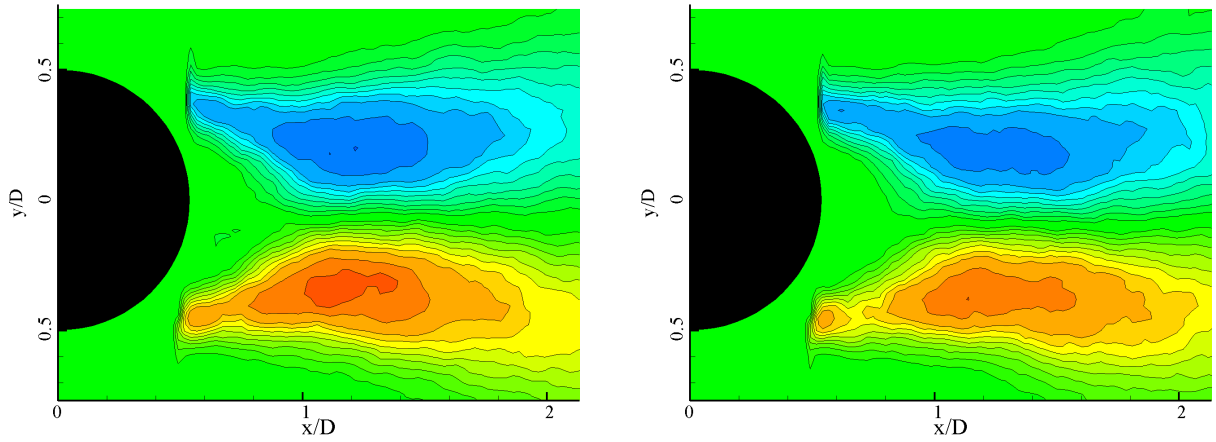

(a) In-phase (b) Out-of-phase

Figure 3.53: Reynolds shear stress contour (Re = 24,000, f_e = 138 Hz)

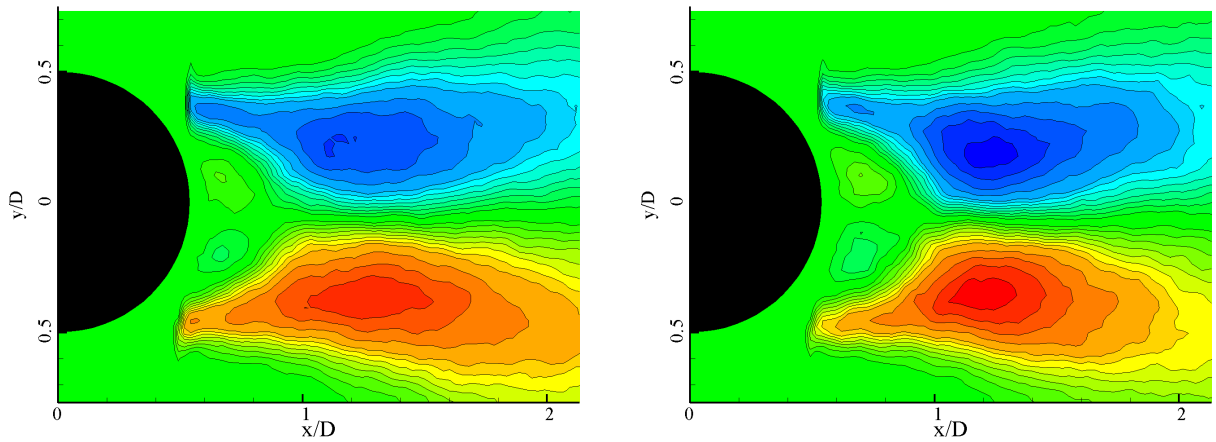

(a) In-phase (b) Out-of-phase

Figure 3.54: Reynolds shear stress contour (Re = 24,000, f_e = 184 Hz)

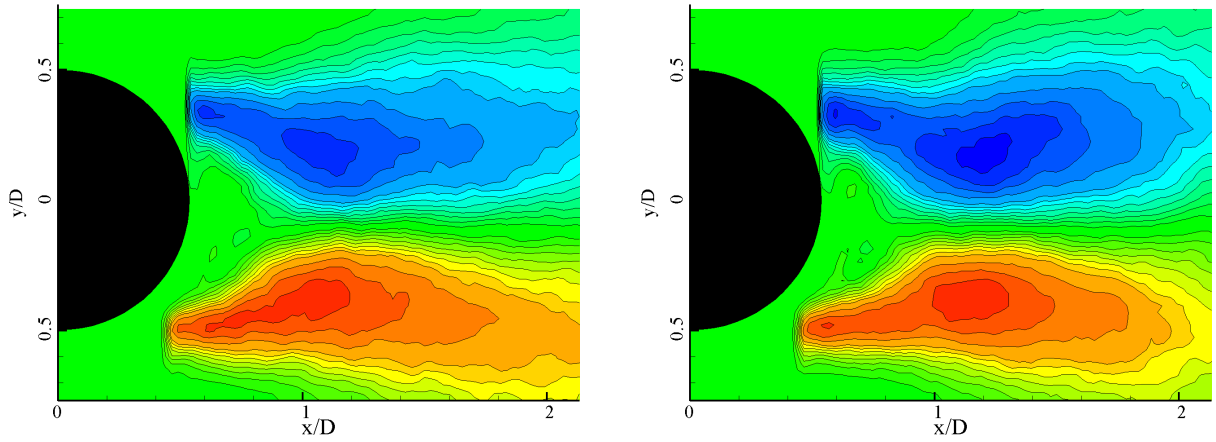

(a) In-phase (b) Out-of-phase

Figure 3.55: Reynolds shear stress contour (Re = 24,000, f_e = Random noise)

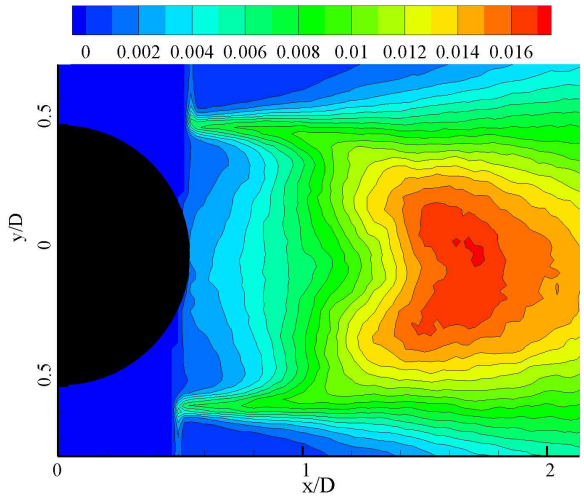

Figure 3.56: Turbulent kinetic energy contour (Re = 12,000, No forcing)

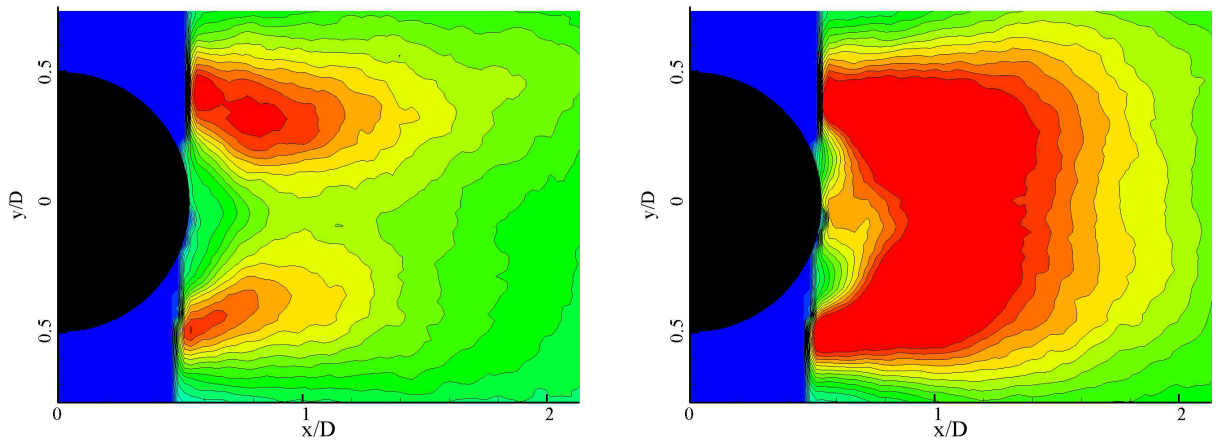

(a) In-phase

(b) Out-of-phase

Figure 3.57: Turbulent kinetic energy contour (Re = 12,000, f_e = 11.5 Hz)

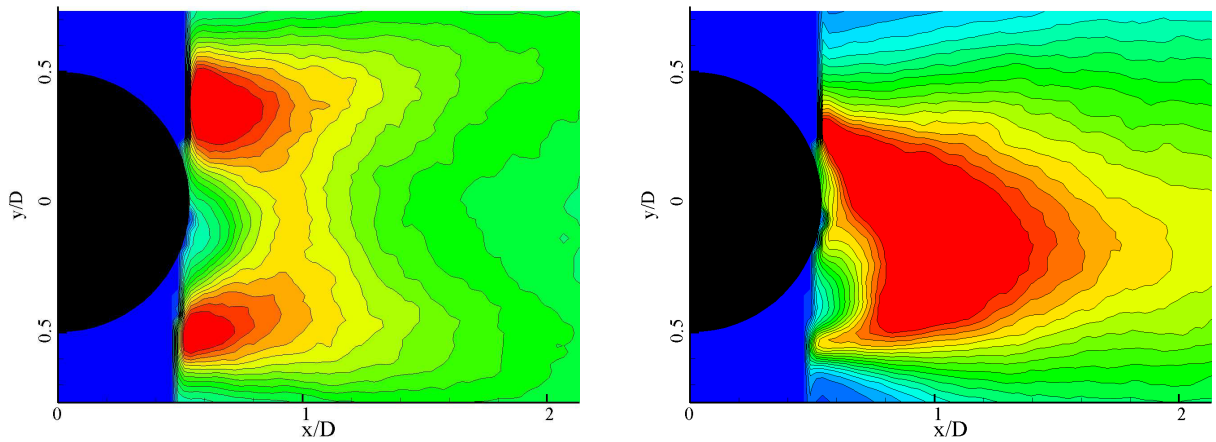

(a) In-phase (b) Out-of-phase

Figure 3.58: Turbulent kinetic energy contour (Re = 12,000, f_e = 23 Hz)

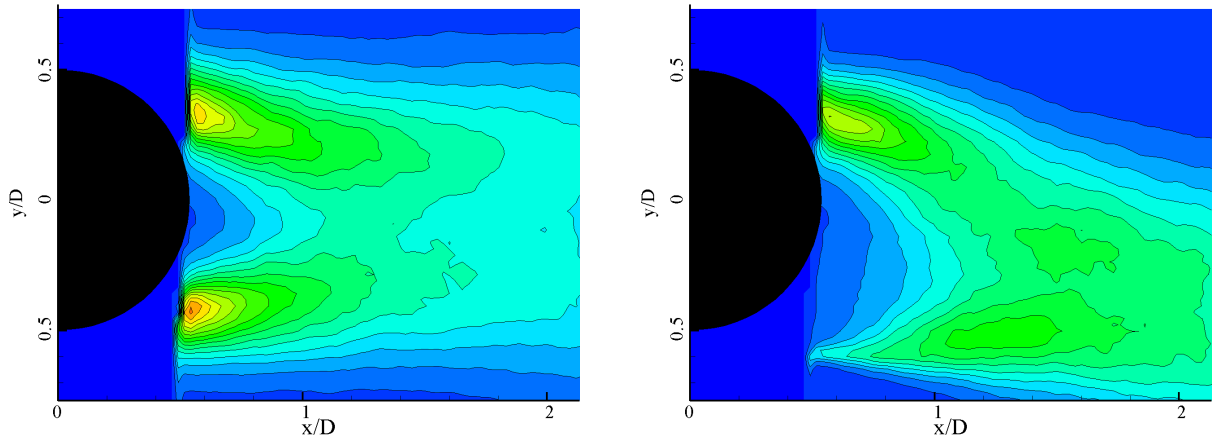

(a) In-phase (b) Out-of-phase

Figure 3.59: Turbulent kinetic energy contour (Re = 12,000, f_e = 46 Hz)

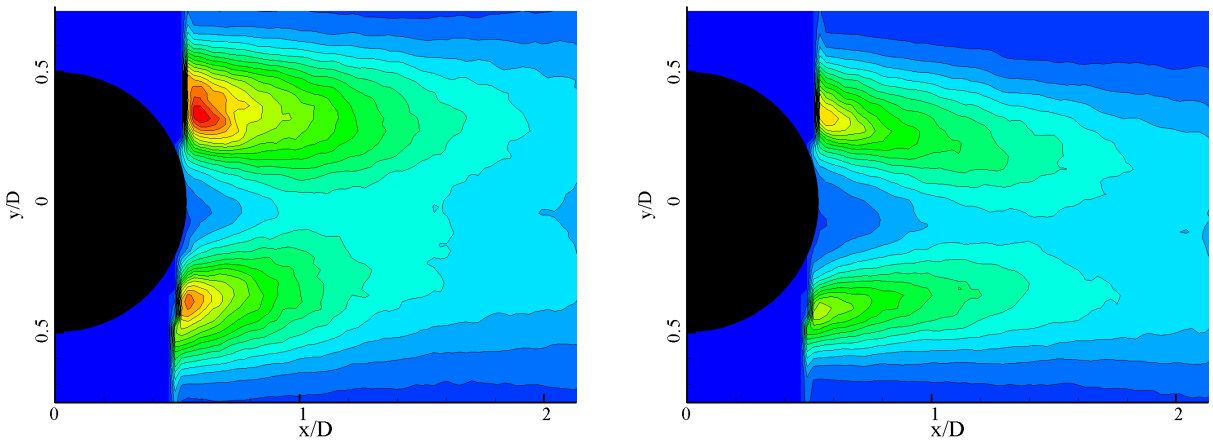

(a) In-phase (b) Out-of-phase

Figure 3.60: Turbulent kinetic energy contour (Re = 12,000, f_e = 69 Hz)

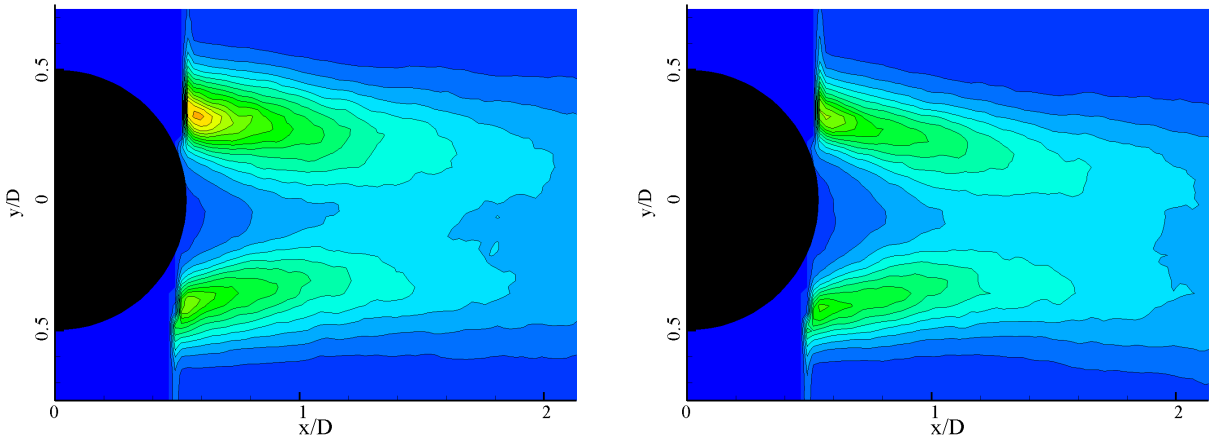

(a) In-phase (b) Out-of-phase

Figure 3.61: Turbulent kinetic energy contour (Re = 12,000, f_e = 92 Hz)

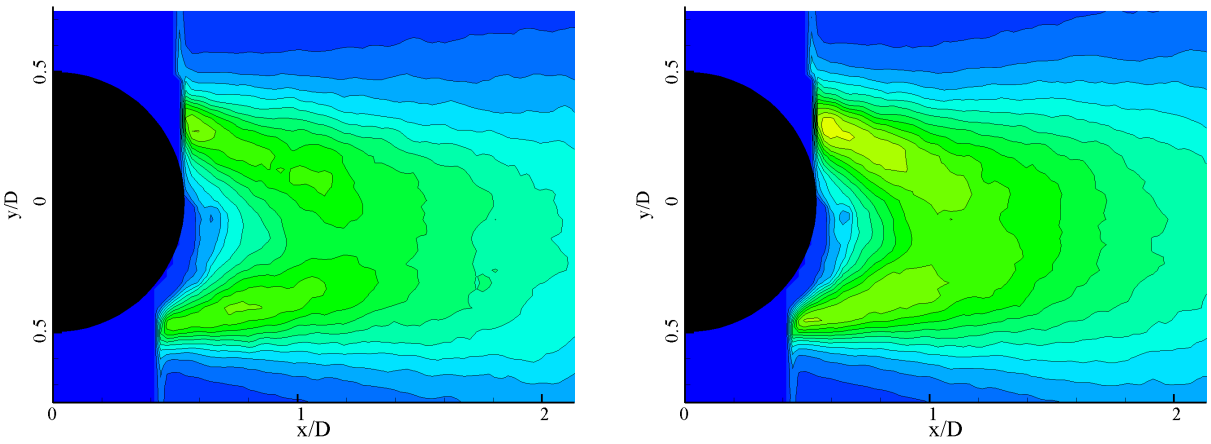

(a) In-phase (b) Out-of-phase

Figure 3.62: Turbulent kinetic energy contour (Re = 12,000, f_e = Random noise)

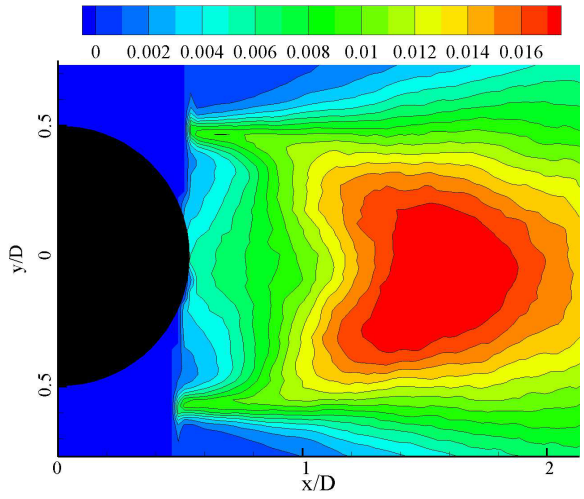

Figure 3.63: Turbulent kinetic energy contour (Re = 24,000, No forcing)

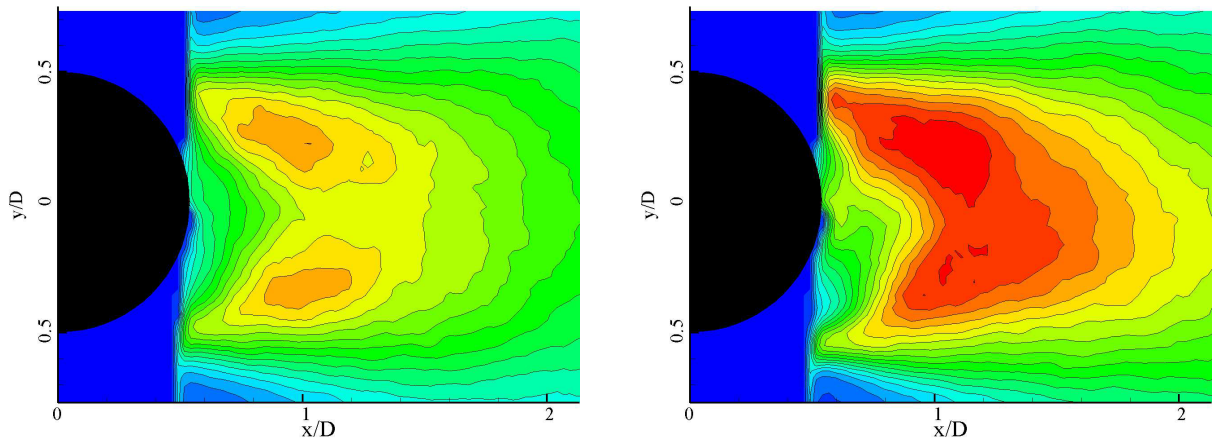

(a) In-phase (b) Out-of-phase

Figure 3.64: Turbulent kinetic energy contour (Re = 24,000, f_e = 23 Hz)

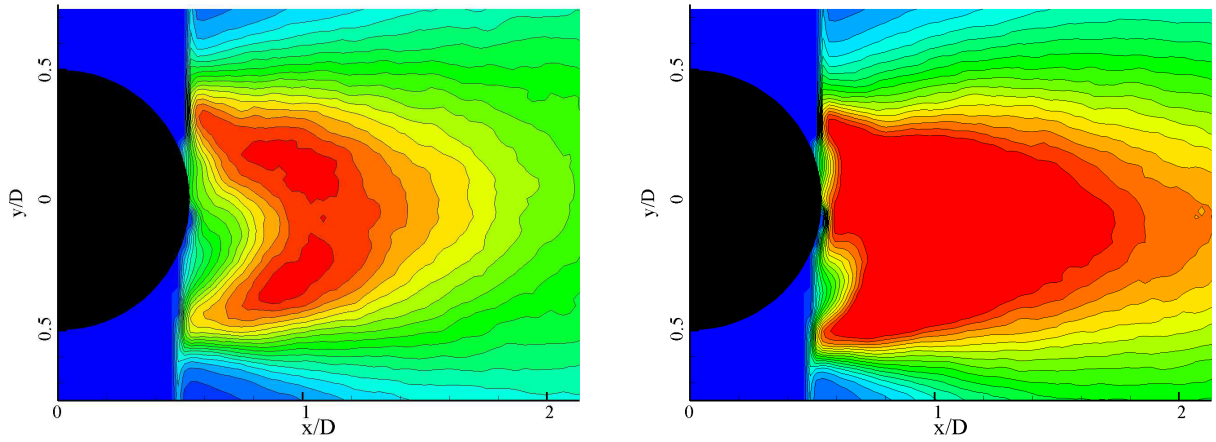

(a) In-phase (b) Out-of-phase

Figure 3.65: Turbulent kinetic energy contour (Re = 24,000, f_e = 46 Hz)

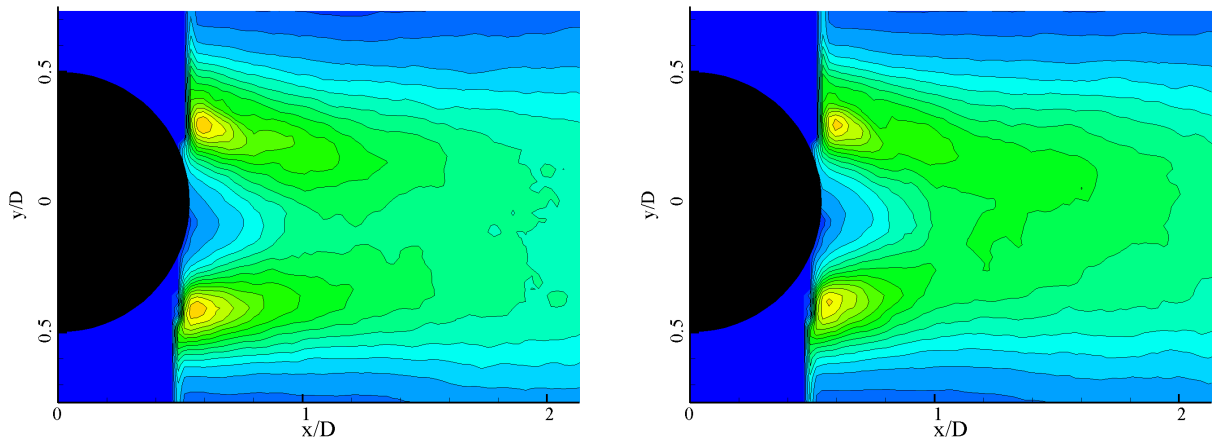

(a) In-phase (b) Out-of-phase

Figure 3.66: Turbulent kinetic energy contour (Re = 24,000, f_e = 92 Hz)

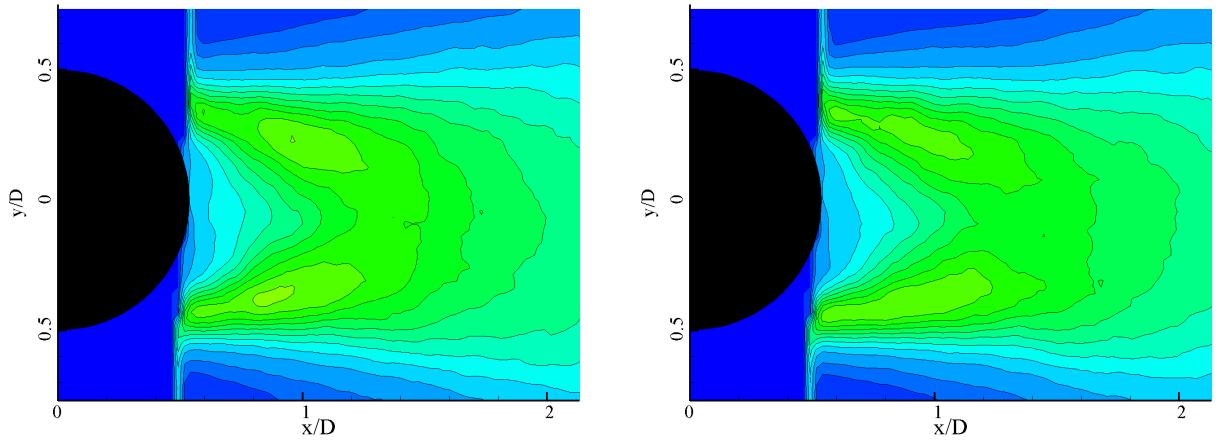

(a) In-phase (b) Out-of-phase

Figure 3.67: Turbulent kinetic energy contour (Re = 24,000, f_e = 138 Hz)

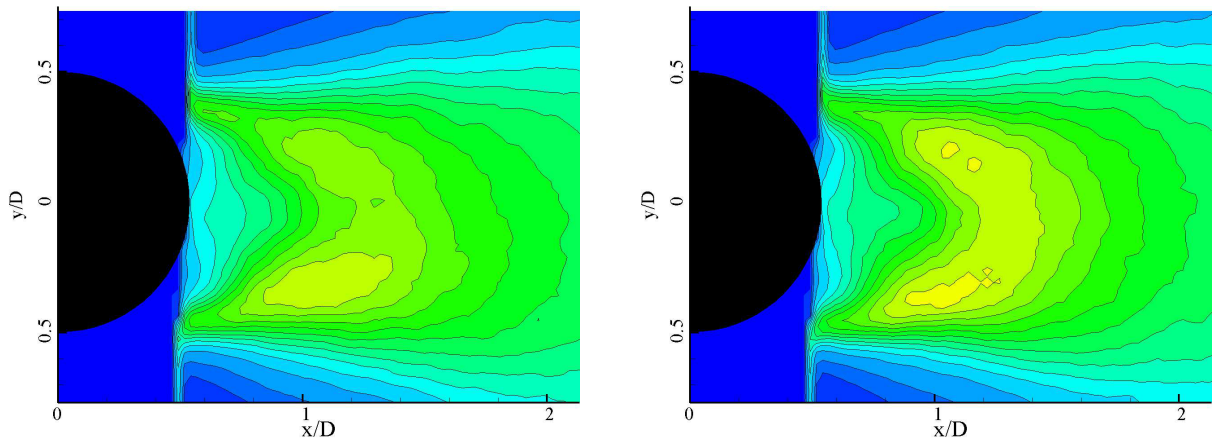

(a) In-phase (b) Out-of-phase

Figure 3.68: Turbulent kinetic energy contour (Re = 24,000, f_e = 184 Hz)

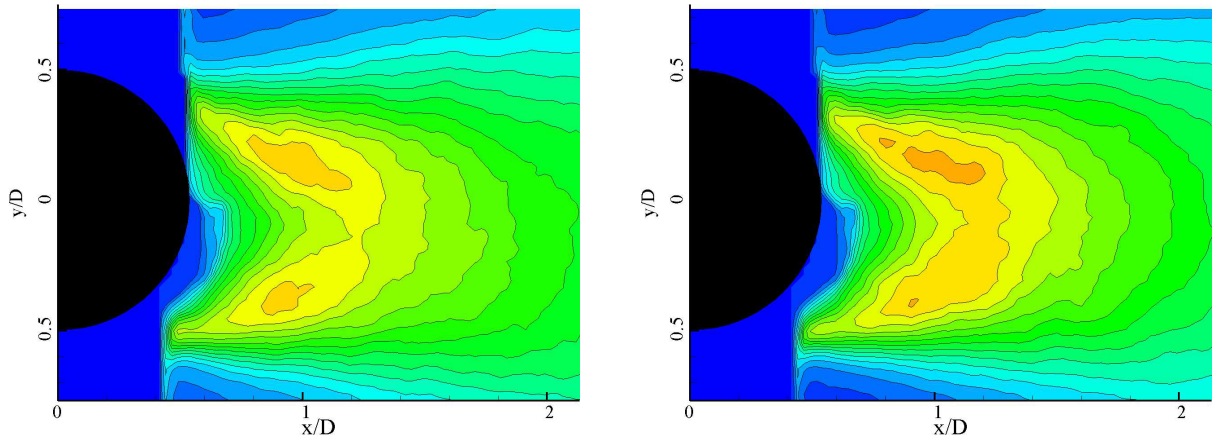

(a) In-phase (b) Out-of-phase

Figure 3.69: Turbulent kinetic energy contour (Re = 24,000, f_e = Random noise)

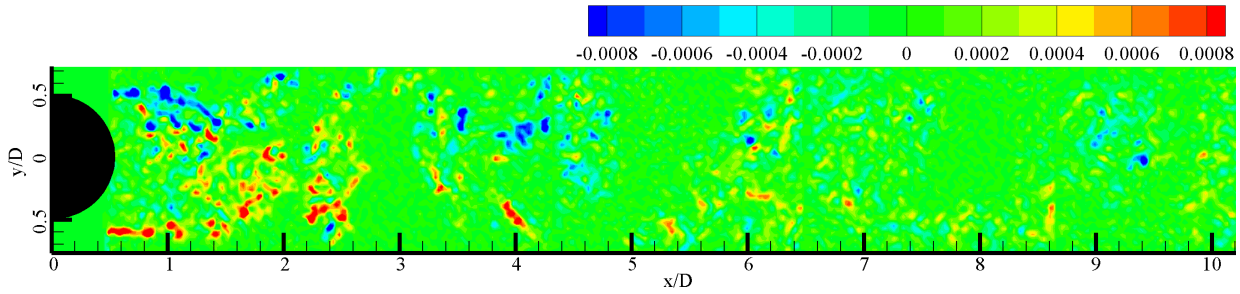

Figure 3.70: Vorticity contour (Re = 12,000, No forcing)

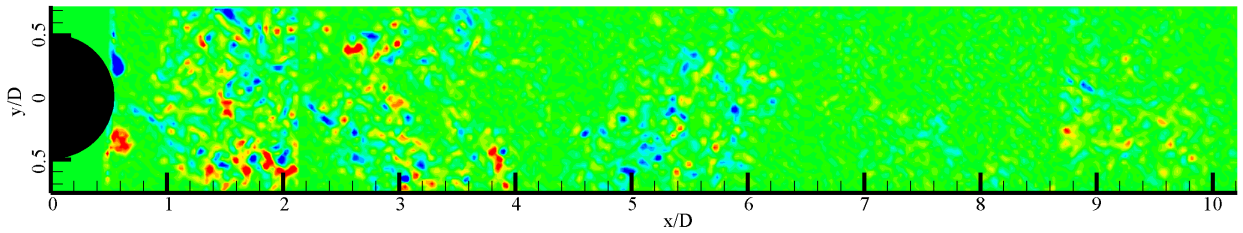

(a) In-phase

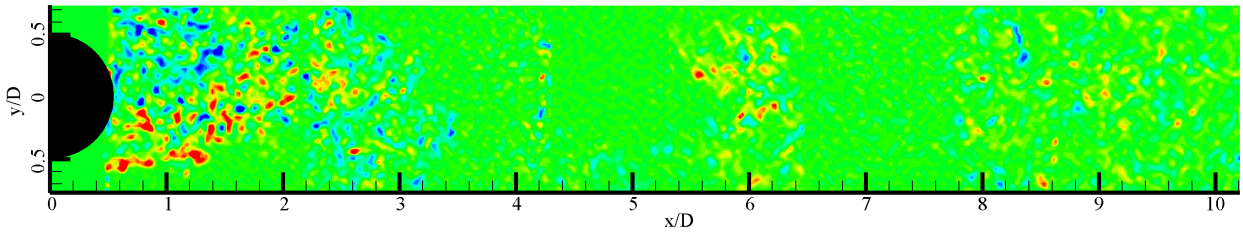

(b) Out-of-phase

Figure 3.71: Vorticity contour (Re = 12,000, f_e = 11.5 Hz)

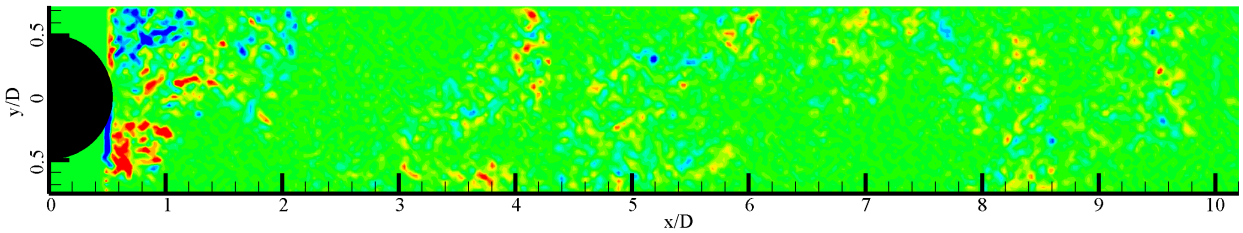

(a) In-phase

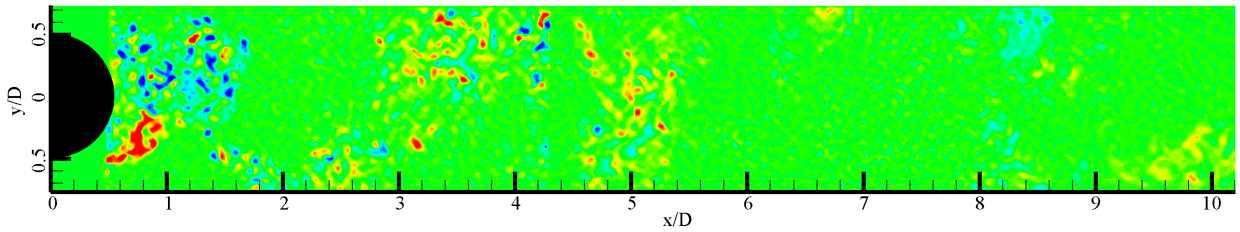

(b) Out-of-phase

Figure 3.72: Vorticity contour (Re = 12,000, f_e = 23 Hz)

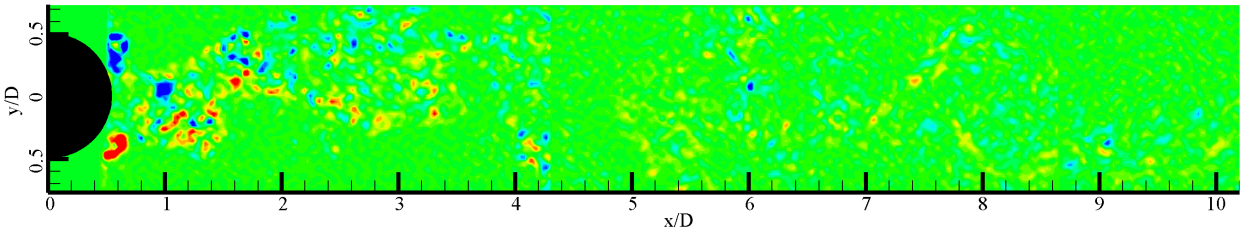

(a) In-phase

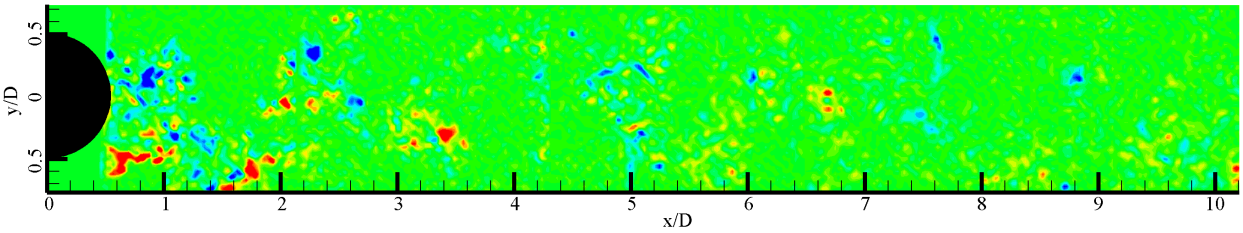

(b) Out-of-phase

Figure 3.73: Vorticity contour (Re = 12,000, f_e = 46 Hz)

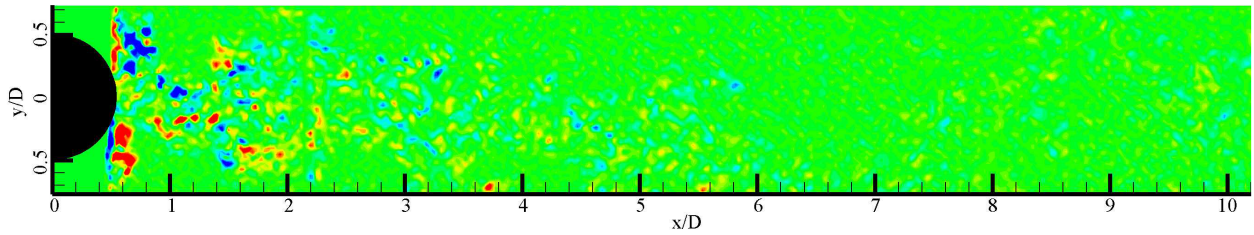

(a) In-phase

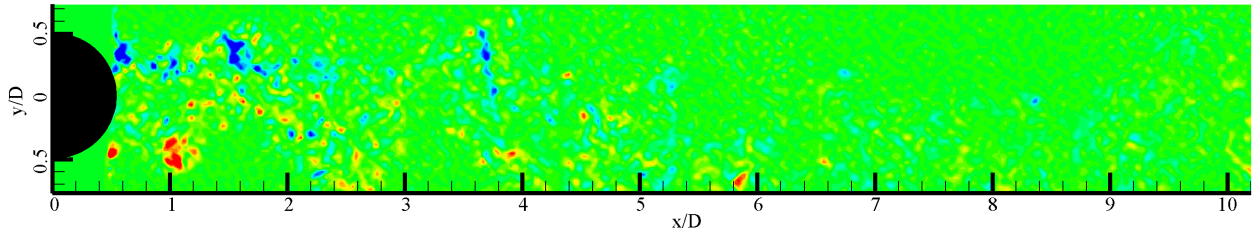

(b) Out-of-phase

Figure 3.74: Vorticity contour (Re = 12,000, f_e = 69 Hz)

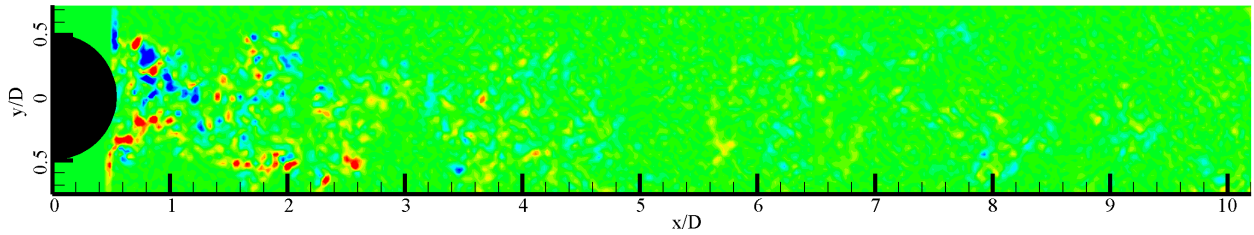

(a) In-phase

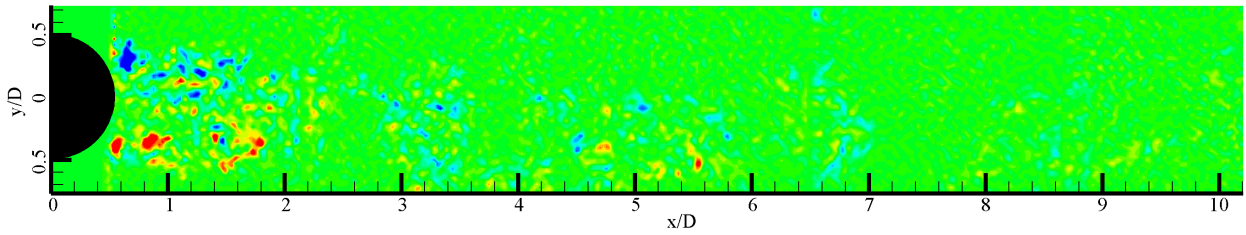

(b) Out-of-phase

Figure 3.75: Vorticity contour (Re = 12,000, f_e = 92 Hz)

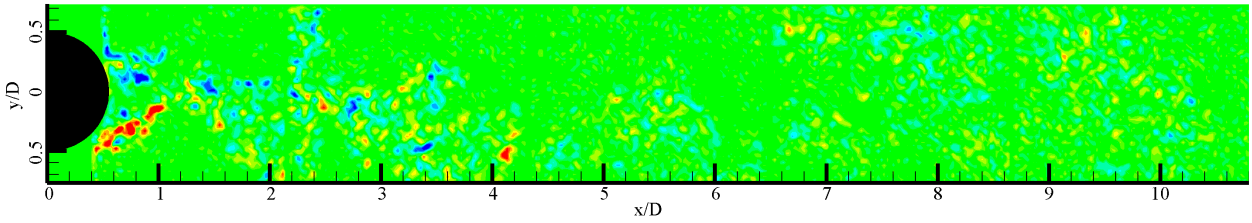

(a) In-phase

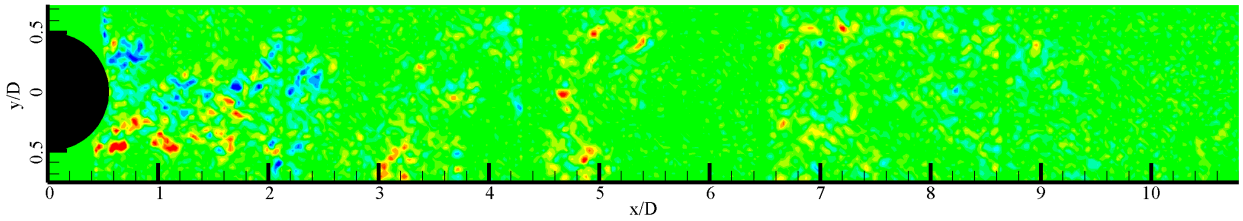

(b) Out-of-phase

Figure 3.76: Vorticity contour (Re = 12,000, f_e = Random noise)

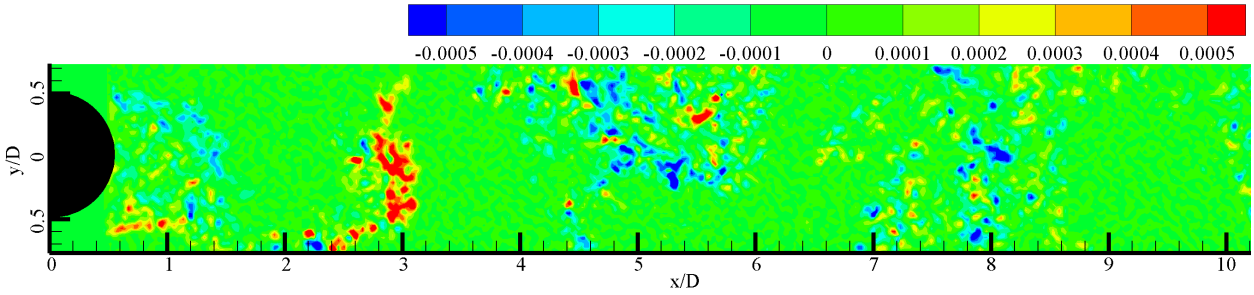

Figure 3.77: Vorticity contour (Re = 24,000, No forcing)

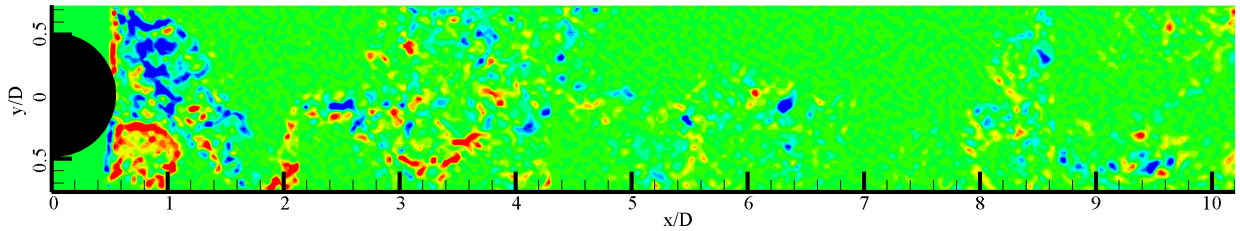

(a) In-phase

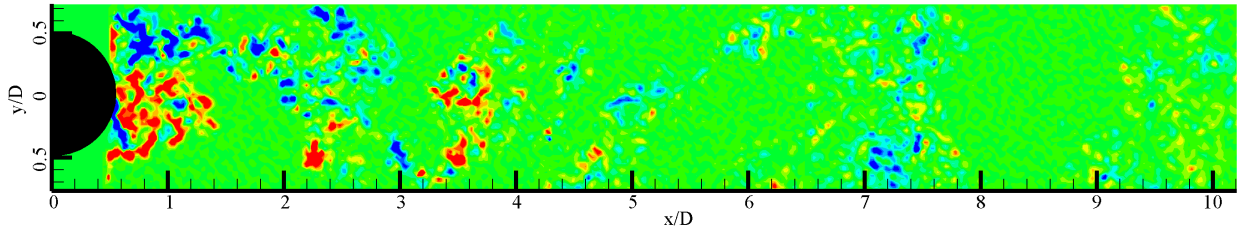

(b) Out-of-phase

Figure 3.78: Vorticity contour (Re = 24,000, f_e = 23 Hz)

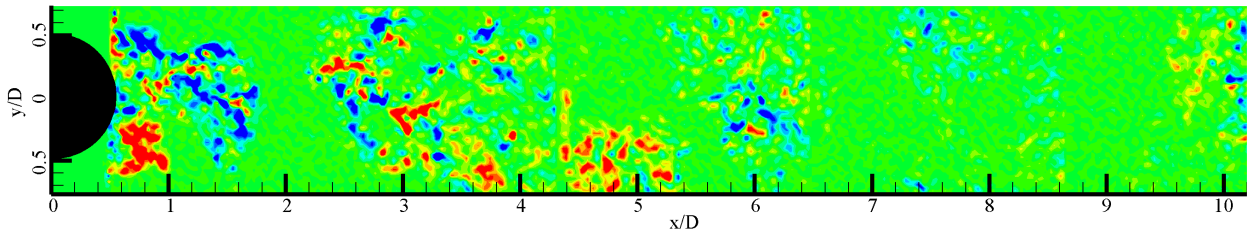

(a) In-phase

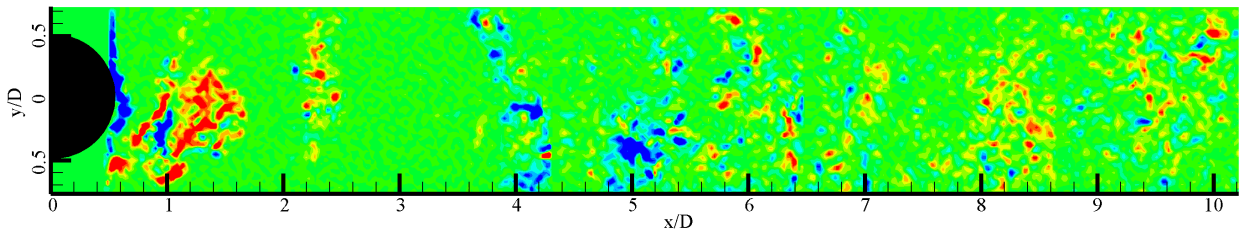

(b) Out-of-phase

Figure 3.79: Vorticity contour (Re = 24,000, f_e = 46 Hz)

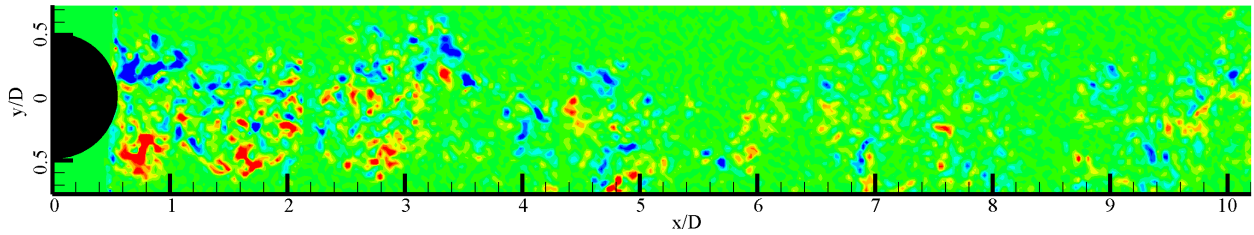

(a) In-phase

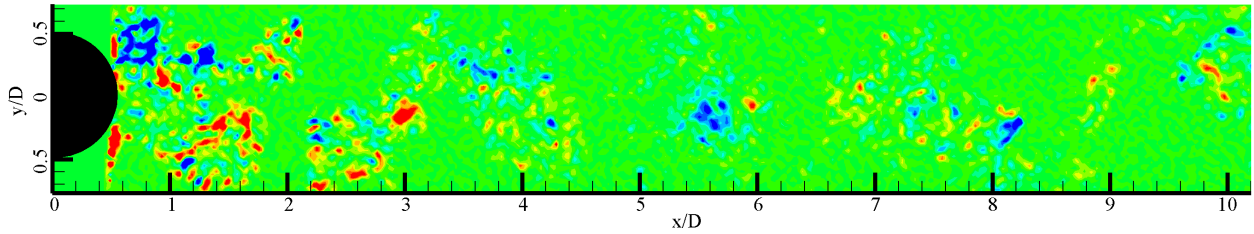

(b) Out-of-phase

Figure 3.80: Vorticity contour (Re = 24,000, f_e = 92 Hz)

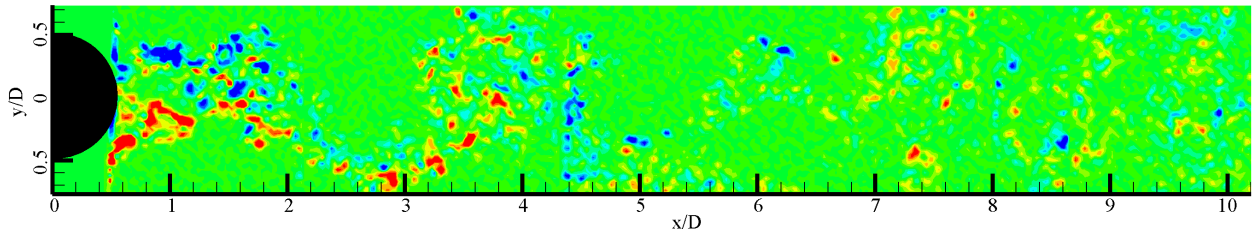

(a) In-phase

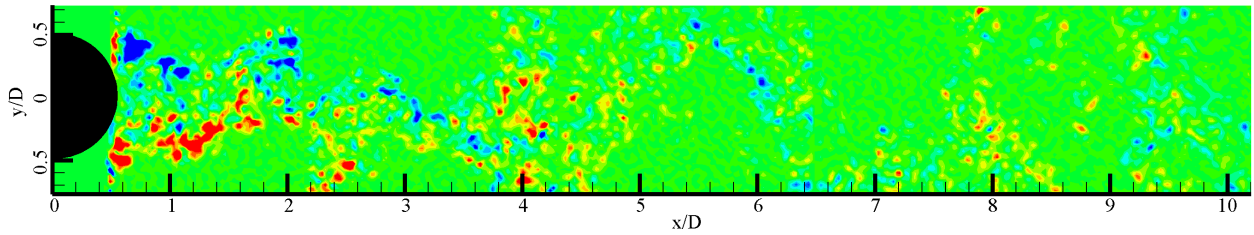

(b) Out-of-phase

Figure 3.81: Vorticity contour (Re = 24,000, f_e = 138 Hz)

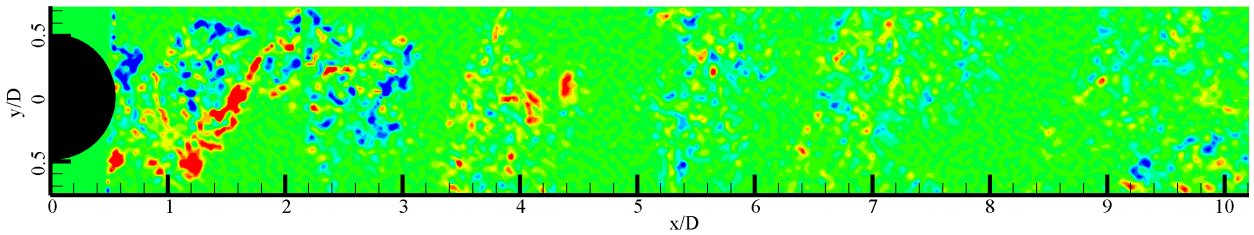

(a) In-phase

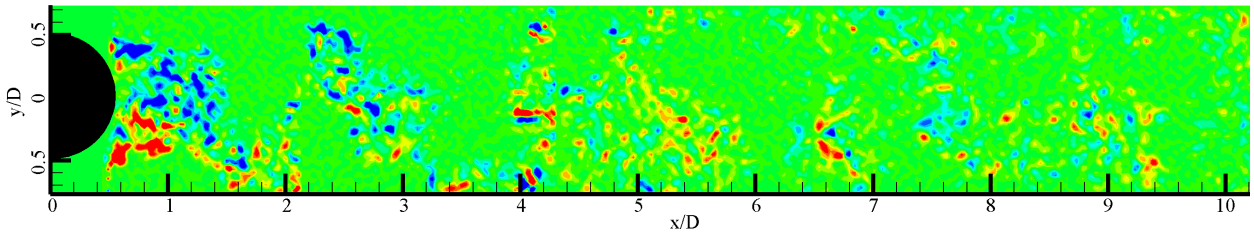

(b) Out-of-phase

Figure 3.82: Vorticity contour (Re = 24,000, f_e = 184 Hz)

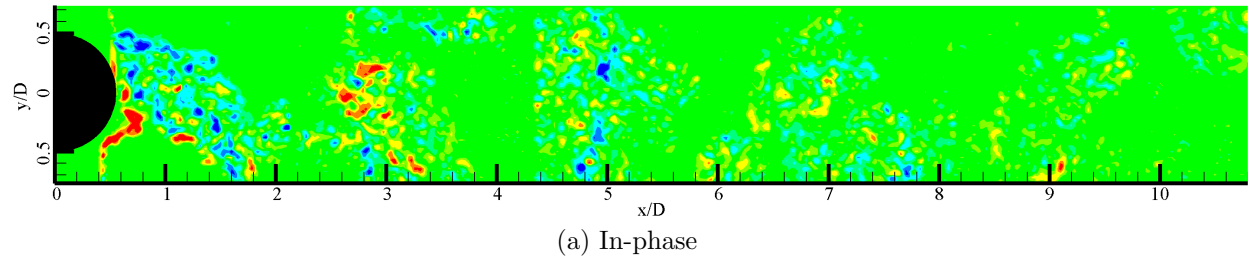

(a) In-phase

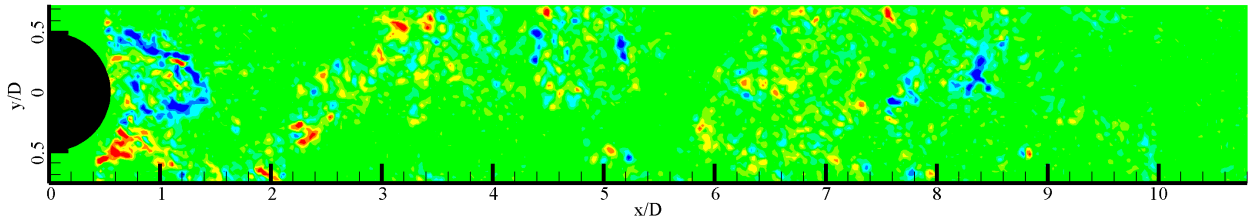

(b) Out-of-phase

Figure 3.83: Vorticity contour (Re = 24,000, f_e = Random noise)

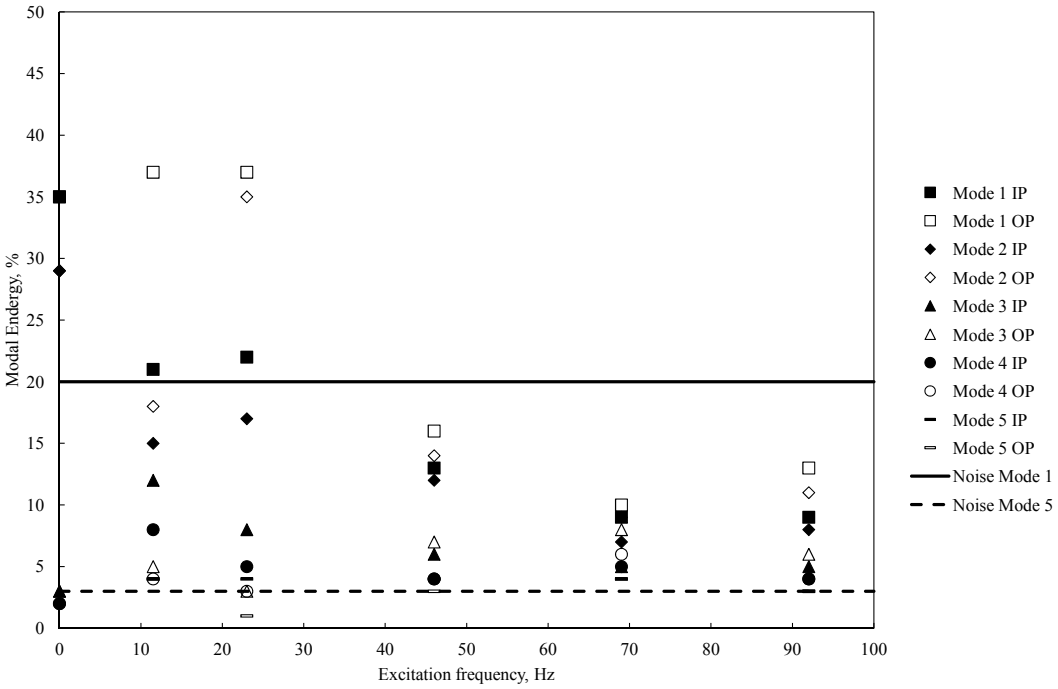

Figure 3.84: Energy distribution, (Re = 12,000, $\frac{x}{D}$=4)

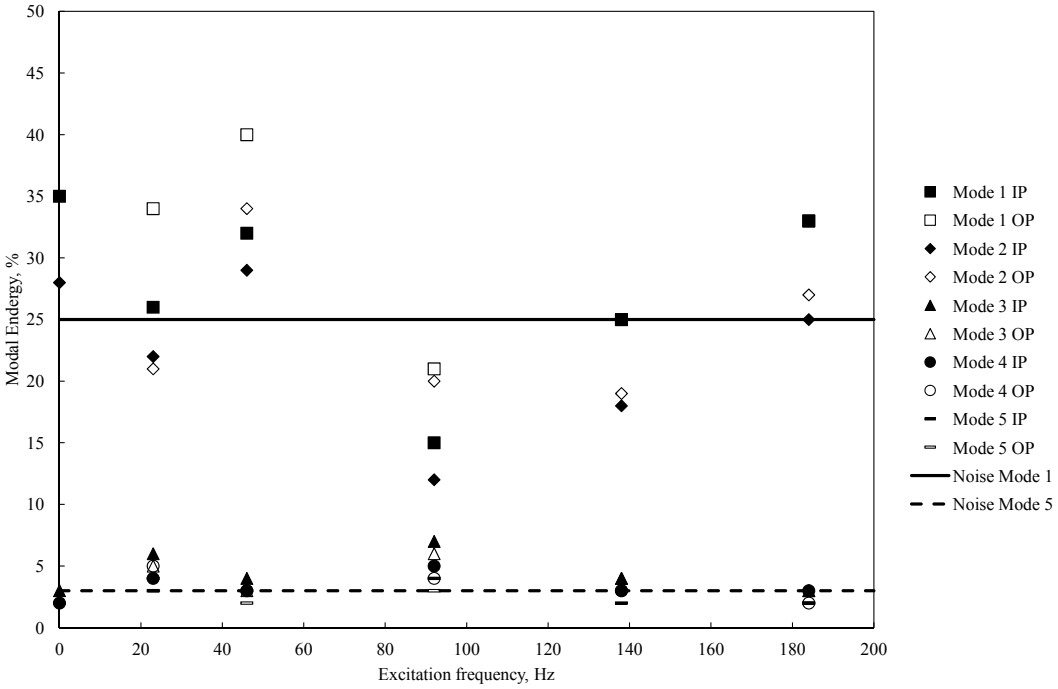

Figure 3.85: Energy distribution, (Re = 24,000, $\frac{x}{D}$=4)

Chapter 4

Conclusions

The wake of a circular cylinder subjected to various periodic forcing frequencies in two modes was investigated. Two pairs of acoustic drivers were used to subject the flow to the two dimensional disturbances through two straight slits on the cylinder surface in diametrically opposite locations. The experiments were conducted at Reynolds numbers of 12,000 and 24,000 in a closed circuit wind tunnel. The power spectral density plots showed a successful suppression of the von Kármán instability for $f_e \geq 2f_{s_0}$ for both Reynolds number cases when an in-phase forcing mode was used. It was found that for the out-of-phase forcing case, the shedding frequency locked on to the forcing frequency. For $f_e = \frac{1}{2}f_{s_0}$ and f_{s_0} there was an increase in vortex strength caused by the addition of energy injected into the shear layers, which accelerated the shear layers and compounded the primary instability. The harmonic and sub-harmonic forcing frequencies built upon the instability by either syncing with the natural shedding frequency in the out-of-phase case or, in the in-phase case, adding kinetic energy to the formation of the vortex formation. The effectiveness of the in-phase mode relative to the out-of-phase mode was also reflected in the drag calculations. On average, $f_e = 4f_{s_0}$ provided the most relief in drag with the in-phase mode reducing drag for a Reynolds number of 12,000 by 28% 4 diameters downstream, whereas the out-of-phase mode resulted in a drag reduction of only 26%. When the Reynolds number was increased to 24,000, the near wake saw a larger drag reduction, while the positive effects of forcing decreased farther downstream. This was, in part, due to a greater amount of kinetic energy in the higher Reynolds number flow, negating the effects of the vortex suppression. A larger decrease in drag was seen with the in-phase forcing mode compared to the out-of-phase mode. Streamline topology, time-averaged turbulence intensity, Reynolds shear stress,

turbulent kinetic energy, and vorticity were calculated to provide a glimpse into the turbulent structures in the wake of the cylinder. A peak in velocity fluctuations occurred along the shear layers on the top and bottom of the cylinder. Higher magnitudes indicated a stronger shear layer able to produce larger eddies, forming a more turbulent wake. A decrease was seen in the fluctuating velocities as the periodic forcing took effect above $f_e = 2f_{s_0}$. The direct correlation between Reynolds shear stress and streamwise velocity fluctuations confirmed successful flow control. The contour plots of the Reynolds shear stress also revealed the shear layer asymmetry introduced by the in-phase mode. The turbulent kinetic energy in the cylinder wake was observed to have a greater response to the in-phase mode. The vorticity contour plots showed that as the forcing was implemented, the wake narrowed and a decrease in vorticity concentration occurred, which supports evidence of the reduction of wake periodicity. The random noise forcing reduced drag and the turbulent quantities in the cylinder wake for both flow velocities. Further investigation of these effects may prove to be beneficial due to the possible application of only a single excitation frequency over a wide range of Reynolds numbers.

Bibliography

[1] Zdravkovich, M. M., *Flow Around Circular Cylinders*, Oxford University Press, 1997.

[2] Gerrard, J. H., "Vortex-Induced Vibrations," *Annual Review of Fluid Mechanics*, Vol. 36, 2004, pp. 413– 455.

[3] Berger, E. and Wille, R., "Periodic flow phenomena," *Annual Review of Fluid Mechanics*, Vol. 4, 1972, pp. 314– 340.

[4] Bearman, P. W., "Vortex shedding from oscillating bluff bodies," *Annual Review of Fluid Mechanics*, Vol. 16, 1984, pp. 195– 222.

[5] Jr., H. O., "Wake behind blunt bodies," *Annual Review of Fluid Mechanics*, Vol. 22, 1990, pp. 539– 564.

[6] Williamson, C. H. K., "Vortex dynamics in the cylinder wake," *Annual Review of Fluid Mechanics*, Vol. 28, 1996, pp. 477– 539.

[7] Rockwell, D., "Vortex-body interactions," *Annual Review of Fluid Mechanics*, Vol. 30, 1998, pp. 199– 229.

[8] Roshko, A., "On the wake and drag of bluff bodies," *Jounal of Aeronautical Sciences*, Vol. 22, 1955, pp. 124– 132.

[9] Williamson, C. H. K. and Govardhan, R., "Vortex-Induced Vibrations," *Annual Review of Fluid Mechanics*, Vol. 36, 2004, pp. 413– 455.

[10] Kumar, B. and Mittal, S., "The mechanics of the formation region of vortices behind bluff bodies," *Journal of Fluid Mechanics*, Vol. 25, 1966, pp. 401– 413.

[11] Cardell, G. S., *Flow Past a Circular Cylinder with a permeable Wake Splitter Plate*, Master's thesis, California Institute of Technology.

[12] Choi, H., Jeon, W.-P., and Kim, J., "Control of flow over a bluff body," *Annual Review of Fluid Mechanics*, Vol. 40, 2008, pp. 113– 139.

[13] Owen, J. C. and Bearman, P. W., "Passive control of VIV with drag reduction," *Journal of Fluids and Structures*, Vol. 15, 2001, pp. 597– 605.

[14] Nakamura, H. and Igarashi, T., "Reductions in drag and fluctuating forces for a circular cylinder by attaching cylindrical rings," *Journal of Fluid Science and Technology*, Vol. 2, No. 1, 2007, pp. 12– 22.

[15] Liu, Y. Z., Shi, L. L., and Yu, J., "TR-PIV measurement of the wake behind a grooved cylinder at low Reynolds number," *Journal of Fluids and Structures*, Vol. 27, 2011, pp. 394– 407.

[16] Shao, C. P., Wang, J. M., and Wei, Q., "Visualization study on suppression of vortex shedding from a cylinder," *Journal of Visualization Society of Japan*, Vol. 10, No. 1, 2007, pp. 57– 64.

[17] Ahmed, A., Khan, M. J., and Bays-Muchmore, B., "Experimental investigation of three dimensional bluff body wake," *AIAA Journal*, Vol. 31, 1993, pp. 559– 563.

[18] Anderson, E. and Szewczyk, A., "Effects of a splitter plate on the near wake of a circular cylinder in 2 and 3-dimensional flow configurations," *Experiments in Fluids*, Vol. 23, 1997, pp. 161– 174.

[19] Bearman, P. W., "Investigation of the flow behind a two-dimensional model with a blunt trailing edge and fitted with splitter plates," *Journal of Fluid Mechanics*, Vol. 21, 1965, pp. 241– 255.

[20] Hwang, J.-Y., Yang, K.-S., and Sun, S.-H., "Reduction of flow-induced forces on a circular cylinder using a detached splitter plate," *Physics of Fluids*, Vol. 15, No. 8, 2003, pp. 2433– 2436.

[21] Kwon, K. and Choi, H., "Control of laminar vortex shedding behind a circular cylinder using splitter plates," *Physics of Fluids*, Vol. 8, No. 2, 1996, pp. 479– 486.

[22] Ozono, S., "Flow control of vortex shedding by a short splitter plate asymmetrically arranged downstream of a cylinder," *Physics of Fluids*, Vol. 11, No. 10, 1999, pp. 2928– 2934.

[23] Scruton, C. and Walshe, D. E., "A means of avoiding wind-excited oscillations of structures with circular or nearly circular cross-section," Tech. rep. 335, 1957.

[24] Woodgate, L. and Mabey, J. F. M., "Further experiments on the use of helical strakes for avoiding wind-excited oscillations of structures of circular or nearly circular section," Tech. rep. 381, 1959.

[25] Hirsch, G., Ruscheweyh, H., and Zutt, H., "Damage on a 140 m high steel stack due to wind-induced transverse vibration (in German)," *Der Stahlbau*, Vol. 2, 1975, pp. 33– 41.

[26] Wong, H. Y. and Kokkalis, A., "A comparitive study of three aerodynamic devices for suppressing vortex-induced oscillation," *Jornal of Wind Engineering and Industrial Aerodynamics*, Vol. 10, 1982, pp. 21– 29.

[27] Every, M. J., Kinjg, R., and Weaver, D. S., "Vortex-induced vibrations of cylinders and cables and their suppression," *Ocean Engineering*, Vol. 9, 1982, pp. 135– 157.

[28] Ekmecki, A. and Rockwell, D., "Effects of a geometrical surface disturbance on flow past a circular cylinder: a large-scale spanwise wire," *Journal of Fluid Mechanics*, Vol. 665, 2010, pp. 120– 157.

[29] Kareem, A. and Cheng, C. M., "Pressure and force fluctuations on isolated roughened circular cylinders of finite height in boundary layer flows," *Journal of Fluids and Structures*, Vol. 13, 1999, pp. 907– 933.

[30] Yoon, J., *Control of flow over a circular cylinder using a wake disrupter*, Master's thesis, Seoul Natl. Univ., Korea.

[31] Blevins, R., *Flow-Induced Vibration*, New York: Van Nostrand Reinhold. 2nd ed., 1990.

[32] Tokumaru, P. T. and Dimotakis, P. E., "Rotary oscillatory control of a cylinder wake," *Journal of Fluid Mechanics*, Vol. 224, 1991, pp. 77– 90.

[33] Bearman, P. W., "The effect of base bleed on the flow behind a two-dimensional model with a blunt trailing edge," *Aeronautical Quarterly*, Vol. 18, 1967, pp. 207– 2240.

[34] Wood, C. J., "The effect of base bleed on a periodic wake," *Journal of the Royal Aeronautical Society*, Vol. 68, 1964, pp. 477– 482.

[35] Koopman, G. H., "The vortex wakes of vibrating cylinders at low Reynolds numbers," *Journal of Fluid Mechanics*, Vol. 28, 1967, pp. 501– 512.

[36] Ongoren, A. and Rockwell, D., "Flow structures from an oscillating cylinder Part 1. Mechanisms of phase shift and recovery in teh near wake," *Journal of Fluid Mechanics*, Vol. 191, 1988, pp. 197– 223.

[37] Fransson, J. H. M., Konieczny, P., and Alfredsson, P. H., "Flow around a porous cylinder subject to continuous suction or blowing," *Journal of Fluids and Structures*, Vol. 19, 2004, pp. 1031– 1048.

[38] Blevins, R. D., "The effect of sound on vortex shedding from cylinders," *Journal of Fluid Mechanics*, Vol. 161, 1985, pp. 217– 237.

[39] Detemple-Laake, E. and Eckelmann, H., "Phenomonology of Kármán vortex streets in oscillatory flow," *Experiments in Fluids*, Vol. 7, 1997, pp. 217– 227.

[40] Huang, X. Y., "Suppression of vortex shedding from a circular cylinder by internal acoustic excitation," *Journal of Fluids and Structures*, Vol. 9, 1995, pp. 563– 570.

[41] Fujisawa, N. and Takeda, G., "Flow control around a cicular cylinder by internal acoustic excitation," *Journal of Fluids and Structures*, Vol. 19, 2004, pp. 1031– 1048.

[42] Bhattacharya, S., *Effect of three dimensional forcing on the wake of a circular cylinder*, Master's thesis, Auburn University.

[43] Detemple-Laake, E. and Eckelmann, H., "Phenomenology of Karman vortex streets in oscillatory flow," *Experiments in Fluids*, Vol. 7, 1989, pp. 217– 227.

[44] Hsiao, F. B. and Shyu, J. Y., "Influence of Internal Acoustic Excitation upon Flow Passing a Circular Cylinder," *Journal of Fluids and Structures*, Vol. 5, 1991, pp. 427–442.

[45] Bernero, S. and Fiedler, H., "Application of particle image velocimetry and proper orthogonal decomposition to the study of a jet in a counterflow," *Experiments in Fluids*, 2000, pp. S274– S281.

[46] Jorgensen, F. E., *How to Measure Turbulence with Hot-wire Anemometers: A Practical Guide*, Dantec Dynamics, 2005.

[47] M. Raffel, C. W. and Kompenhans, J., *Particle Image Velocimetry: A Practical Guide*, Springer-Verlag, 1998.

Appendices

Appendix A

Calibration

The content of this appendix describes the calibration procedure for the hot wire, power amplifier, and pressure transducer, which was carried out before each experiment.

A.1 Constant temperature anemometer calibration

The single wire was calibrated using a jet calibrator. The system consisted of an air compressor, pressure regulator, manometer, and a stagnation chamber with a series of three screens and a nozzle. The hot wire was connected to an oscilloscope and the average voltage was measured and recorded for each nozzle exit velocity specified as seen in Table A.1. The calibration ranged from zero to ninety six feet per second. The data was plotted and a fourth order polynomial was fitted to the data and can be noted in Figure A.1. The equation was then used to obtain the voltages and velocities needed to produce the correct blowing coefficients and free stream speeds.

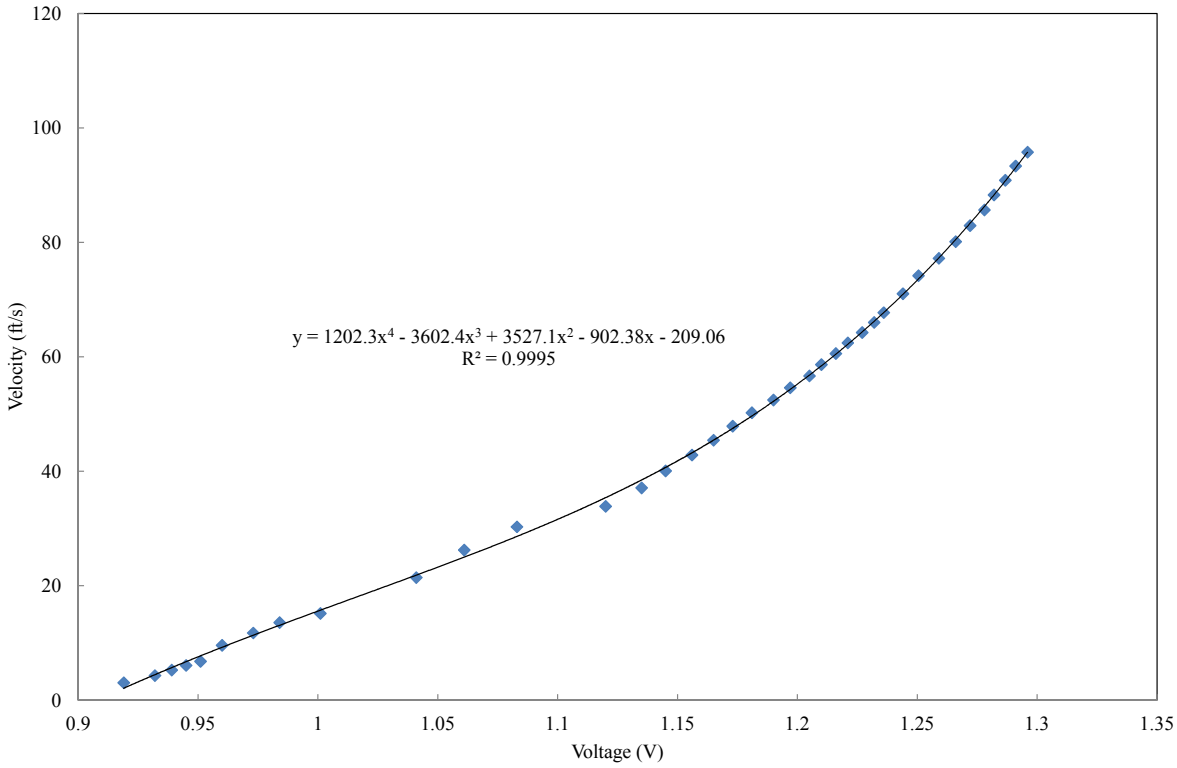

Figure A.1: Hot wire calibration curve

Table A.1: Hot wire calibration data

Pressure (inches H_2O)	Velocity (ft/s)	Voltage (volts)
0	0.00	0.757
0.002	3.03	0.919
0.004	4.28	0.932
0.006	5.25	0.939
0.008	6.06	0.945
0.01	6.77	0.951
0.02	9.58	0.96
0.03	11.73	0.973
0.04	13.55	0.984
0.05	15.14	1.001
0.1	21.42	1.041
0.15	26.23	1.061
0.2	30.29	1.083
0.25	33.86	1.12
0.3	37.09	1.135
0.35	40.07	1.145
0.4	42.83	1.156
0.45	45.43	1.165
0.5	47.89	1.173
0.55	50.23	1.181
0.6	52.46	1.19
0.65	54.60	1.197
0.7	56.66	1.205
0.75	58.65	1.21
0.8	60.58	1.216
0.85	62.44	1.221
0.9	64.25	1.227
0.95	66.01	1.232
1	67.73	1.236
1.1	71.03	1.244
1.2	74.19	1.2505
1.3	77.22	1.259
1.4	80.13	1.266
1.5	82.95	1.272
1.6	85.67	1.278
1.7	88.30	1.282
1.8	90.86	1.2867
1.9	93.35	1.291
2	95.78	1.296

A.2 Power amplifier calibration

The power amplifier was calibrated to obtain the correct voltages needed to produce the specified forcing coefficients from the drivers. The hot wire was positioned just above the slit in the cylinder to read the air velocities produced at each speaker frequency. The amplifier was connected to a wave from generator and an oscilloscope was used to measure the output voltage. At each driver frequency the peak-to-peak voltage required to generate the correct amount of forcing was recorded and the blowing coefficients were verified as seen in Table A.2 for a Reynolds number of 12,000 and Table A.3 for a Reynolds number of 24,000.

Table A.2: Amplifier calibration data at Re = 12,000

Driver freq. (Hz)	Amp. voltage (volts)	C_μ
11.5	37	0.17
23	26	0.168
46	22	0.17
69	18	0.171
92	14	0.173

Table A.3: Amplifier calibration data at Re = 24,000

Driver freq. (Hz)	Amp. voltage (volts)	C_μ
23	45	0.214
46	32	0.218
92	35	0.225
138	48	0.223
184	50	0.222

Appendix B

Calculations

B.1 Drag

The drag values were calculated using the wake deficit method as shown in Equation B.3. This method calculates the amount of momentum lost in the wake due to the presence of the cylinder.

$$P_t = P_s + q \tag{B.1}$$

$$q = \frac{1}{2}\rho U_\infty^2 \tag{B.2}$$

$$C_d = \frac{2}{D}\int_{y_1}^{y_2}\left[\sqrt{\frac{q}{q_\infty}} - \frac{q}{q_\infty}\right]dy \tag{B.3}$$

Appendix C

Uncertainty analysis

An uncertainty analysis was conducted to ensure the precision of the data gathered in this investigation. The reference case selected was the Reynolds number of 12,000, which corresponds to a free stream velocity of about 15 ft/s. Several sources of uncertainty were considered: pressure transducer error, pressure transducer calibration error, hot wire calibration error, and A/D board resolution error.

The pressure transducer error was determined from the data sheet provided by the manufacturer and was found to be 0.5%, which equates to a relative uncertainty of 0.01.

Pressure transducer calibration error was rooted in curve fitting errors. A linear curve fit was used for the calibration and the standard deviation was calculated to be 0.7%. Using equation C.1 [46], the relative uncertainty was calculated to be 0.014.

$$\text{relative standard uncertainty} = 2 * \frac{1}{100}\text{standard deviation (errors, \%)} \tag{C.1}$$

A fourth order polynomial curve was fitted to the hot wire data gathered, shown in Figure A.1. The standard deviation was calculated to be 0.05% which corresponds to a relative uncertainty of 0.001.

The A/D data acquisition board relative uncertainty was calculated using equation C.2.

$$\text{relative standard uncertainty} = \frac{1}{\sqrt{3}}\frac{1}{U_\infty}\frac{E_{AD}}{2^n}\frac{\partial U_\infty}{\partial E} \tag{C.2}$$

where U_∞ is the free stream velocity, E_{AD} is the A/D input range, n is the resolution in bits, and $\frac{\partial U_\infty}{\partial E}$ is the slope of the inverse calibration curve. $E_{AD} = 10V$, $n = 16$, $U_\infty = 15ft/s$, and $\frac{\partial U_\infty}{\partial E} = 153.67$ Plugging in with the above values gives a relative uncertainty of 0.0009025.

Therefore, equation C.3 calculates the total uncertainties present in the mean velocity, which is equal to 3.45%.

$$\text{total standard uncertainty} = 2\sqrt{0.01^2 + 0.014^2 + 0.001^2 + 0.0009025^2} = 0.03451 \qquad \text{(C.3)}$$

The PIV measurements were taken using a 32 pixel interrogation window with a pixel size of ≈ 2. According to Raffel et al [47] the RMS uncertainty is roughly 0.01 pixels. In this investigation, the PIV images had an overlap of 3.5%, which resulted in a 2 pixel uncertainty in the results.